DOI:10.15774/PPKE.ITK.2023.003

Characterization of polymer microstructures for in vitro and in vivo applications

Szabó Ágnes

Theses of the Ph.D. Dissertation

Supervisor: Dr. Fekete Zoltán

Pázmány Péter Catholic University
Faculty of Information Technology and Bionics
Roska Tamás Doctoral School of Sciences and Technology

Budapest, 2022

DOI:10.15774/PPKE.ITK.2023.003

Preface

Interfacing with the neural tissue gives an outstanding opportunity to learn about the brain. Different microelectrodes were developed to record neural activity and study different behaviors. The development of these interfaces allows for enhancing the interaction between the neural tissue and the artificial system. Based on the literature, polymer-based devices are suitable for long-term measurement with an efficient signal-noise ratio and cause a mild immune response compared to traditional, stiff material-based electrodes.

Overview of the thesis The first Chapter, the *General introduction*, presents an overview of the scientific background of the later chapters. First, the neural tissue, its cells, and the electrical recording are described. Then the imaging techniques that are used in this thesis and the potential image processing methods. To understand the operation of the neural interfaces, the manufacturing methods (*MEMS technologies*) are described. Finally, the biocompatibility aspects are specified.

Chapter two contains the research work corresponding with the first thesis group. The first thesis group contains three thesis points about the interaction between a microstructured polymer-based surface and astroglial cells, which have a major role in the immune response to a brain implant.

The third Chapter presents the second thesis group with two thesis points. This work focus on the technical parameters of a multimodal recording setting. A polymer electrode grid is used with two-photon microscopy, and the current thesis work concentrate on the limit of the concurrent usage of the two modalities.

DOI:10.15774/PPKE.ITK.2023.003

Contents

DOI:10.15774/PPKE.ITK.2023.003

DOI:10.15774/PPKE.ITK.2023.003

List of abbreviations

aCSF	artificial cerebrospinal fluid
AI	artificial intelligence
AP	action potential
AZO	aluminum doped zinc oxide
BBB	blood-brain barrier
CNS	central nervous system
CVD	chemical vapor deposition
DAPI	4',6-diamidino-2-phenylindole
DNA	deoxyribonucleic acid
DRIE	deep reactive ion etching
DSP	double side polished
ECM	extracellular matrix
ECoG	electrocorticography
EDTA	ethylenediamine tetraacetic acid
EEG	electroencephalogram
FCS	fetal calf serum
FVB/Ant	FVB originated transgene mouse strain
FWHM	full width half maximum
GCaMP	GFP-Calmodulin-M13-Protein
GFAP	glial fibrillary acidic protein
GUI	graphical user interface
HDMEM	high glucose Dulbecco's Modified Eagle Medium
hNT	human teratocarcinoma cell line
iEEG	intracranial electroencephalogram
ITO	indium-tin-oxide
LFP	local field potential

DOI:10.15774/PPKE.ITK.2023.003

MEMS	microelectromechanical system
PBS	phosphate-buffered saline
PDMS	Polydimethylsiloxane
PEDOT	Poly(3,4-ethylenedioxythiophene)
PEDOT:PSS	Poly(3,4-Poly(3,4-ethylenedioxythiophene):poly(styrenesulfonate)
PET	Polyethylene terephthalate
PFA	Paraformaldehyde
PMT	photomultiplier tubes
PSF	point spread function
PVD	physical vapor deposition
RF	radio frequency
RIE	reactive ion etching
ROI	region of interest
RT	room temperature
SD	standard deviation
SEM	scanning electron microscope
SNR	signal-noise ratio
SUA	single unit activity
UV	ultraviolet

DOI:10.15774/PPKE.ITK.2023.003

Chapter 1

General introduction

1.1. Brain signals and neural recording

1.1.1 Nerve tissue

Brain tissue is made up of two main cell types, neurons, and glial cells. The greater mass of the brain is made up of glial cells, which can be grouped according to their function.

The astroglia plays a significant role in ensuring the connection of neurons. Astroglia perceives remaining neurotransmitters in the synaptic cleft and performs chemical control of the environment. Astrocytes are responsible for the mechanical support of mature neural circuits and can alter the synaptic activity of neurons. At the same time, they control the growth of neurons at rest and allow nutrient transport through the blood-brain barrier (BBB) [1]. In addition, astroglia plays a major role in the immune response to damage in the nervous system. A detailed description of the immune response to an implanted device is given in Chapter 1.5. A feature of astroglia used in imaging is that it expresses a cell skeletal protein called GFAP (glial fibrillary acidic protein). Thus, the astroglia cell skeleton can be seen on fluorescent microscope images by labeling the GFAP protein [2].

Besides astrocytes, microglia are the other major glial cell type. These cells are the local macrophages in the neural tissue, so their role is to protect the nerve tissue. They either act as cytotoxic cells and kill pathogenic organisms or degrade cellular debris and damaged matrix after an injury as phagocytes [3].

The third glial cell type is oligodendrocyte, which has no important part in the response to a brain injury. Oligodendrocytes form the myelin sheath in the central nervous system [4].

Neurons are the nerve-conducting cells of the nervous system that can process stimuli.

DOI:10.15774/PPKE.ITK.2023.003

The connections between them are formed by their characteristic neurites. The neurites of the neuron may be an axon capable of forming action potential and directing the stimulus away from the cell body. Usually, a cell has one axon, the most extended neurite. The nerve cells receive the stimulus with one or more dendrites, which transmit the received signal to the cell body [5]. Dendrites often branch and have dendritic spines that increase the area of the 'dendritic tree'. The structure of a neuron is illustrated in Fig. 1.1.a. The large area of the dendritic tree enhances the neuron-neuron connections through the communication between axon and dendrite, called the synapse, shown in Fig. 1.1. panel b. The information spreads from the axon to the axon terminal, where the signal stimulates the release of chemical transmitters to the synaptic gap. With this release, the electrical signal is translated into a chemical signal. This chemical information passes through the synaptic gap and reaches one dendrite of the other neurons, where the signal turns back into electrical [6].

1.1.2 Signal generation and propagation

The electrical signals are produced by the electrical potential change across the cell membrane. This current represents the flow of ions through the ion channels. The sodium-potassium pump maintains the ion concentration gradient. The cell membrane of the neurons separates charge: the extracellular surface of the membrane has positive charge excess, while the cytoplasmic surface has a negative charge excess. At rest, this potential difference is usually between -60 mV and -70 mV, called the resting membrane potential. A neuron can receive either an excitatory or an inhibitory signal at its dendrites. In case of an excitatory signal, ligand-gated channels open, causing a flow of positively charged ions (mainly sodium ions) into the cell. The positive ions neutralize some of the negative charges, leading to temporary depolarization of the membrane. In case of an inhibitory signal, other ligand-gated channels open, which allow negatively charged ions (mainly chloride) into the cell. This flow generates a temporary hyperpolarization of the membrane. Both ions flow diffusely inside the cell, causing a current, which travels toward the axon hillock. The action potential is generated when the summation of the input signals (both excitatory and inhibitory) gets to the axon hillock and reaches a threshold, typically around -55 mV. An action potential is an all-or-none event, which means that the input current level does not influence the size and shape of the action potential. The amplitude remains constant during the signal propagation through the axon, and the action potential is always followed by a refractory period. The travel of the action potential stops at

DOI:10.15774/PPKE.ITK.2023.003

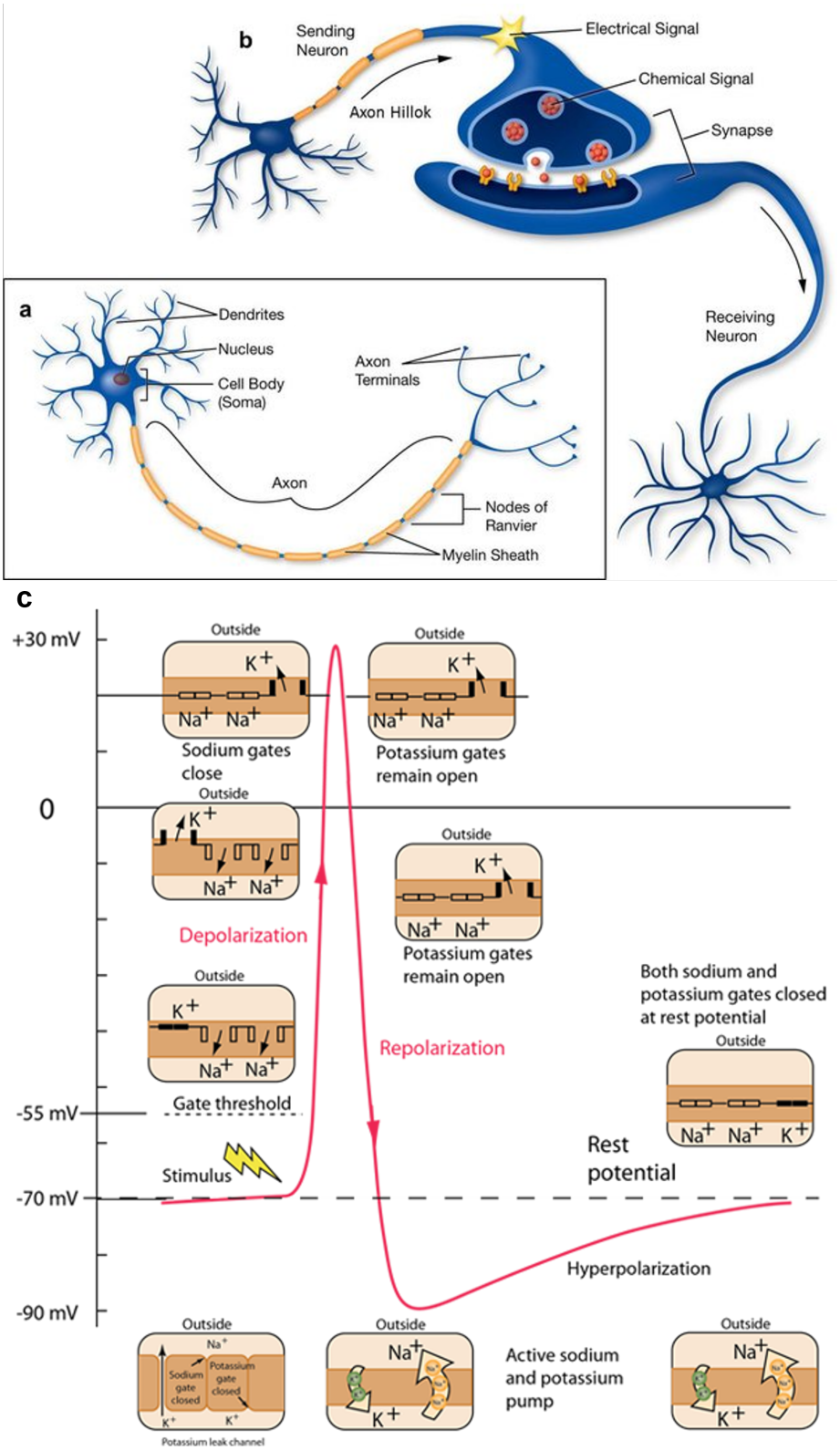

Figure 1.1: a) Structure of neuron. b) structure of synaptic connection. [8] c) Course of action potential [7]

DOI:10.15774/PPKE.ITK.2023.003

the axon terminal, where this signal causes neurotransmitter release to the synaptic cleft between the two neurons. These neurotransmitters can act on the post-synaptic cell, conducting the information towards a new cell and the previously described processes are repeated. The course of an action potential is connected with sodium channels and potassium channels. When the summation of the input signals reaches the threshold, the voltage-gated sodium channels are activated and sodium ions enter the cell. The flow of the positively charged ions causes depolarization. Since the voltage-gated potassium channels have slower kinetics, the potassium channels open approximately 5 ms after reaching the threshold. As the action potential approaches its peak (+30 mV), sodium channels become inactive, while potassium ions continue to leave the cell through the open potassium channels. This ion flow continues even after repolarization until reaching the resting potential. The slow inactivation of the potassium channels allows further potassium ions to leave the cell, causing a negative overshoot, called hyperpolarization. After the hyperpolarization, the active sodium-potassium pumps slowly restore the resting membrane potential. This restoring period causes the refractory period when no new action potential can be generated on the same neuron [6, 7]. The course of action potential and the states of the ion channels are illustrated in Fig.1.1.c.

1.1.3 Signal recordings

Neuronal activity can be measured with a sensor placed in the vicinity of the cell, by measuring the electric field generated by the neurons. The brain tissue can be described as an ohmic conductor medium, with inhomogeneity. The measured potential is inversely proportional to the tissue conductivity and the measured potential is highly distance dependent from the source [9]. Action potential can not spread to a large distance in the extracellular space of the brain tissue, since it has a small potential field distribution, and a short duration (a few milliseconds). Extracellular signals are composed of local field potentials (LFPs) and action potentials (APs). APs or single unit activity (SUA) can be recorded with extracellular recordings if the small recording sites are placed 50-100 µm far from the neurons. The synchronized summed inhibitory and excitatory postsynaptic potentials generate the LFP, with a frequency between a few Hz (delta band: ∼1-4 Hz) to hundreds of Hz (high gamma band: ∼80-150 Hz [10]). Next to the superposition of APs, LFP also contains information on calcium spikes, afterhyperpolarization and slow glial potentials [11, 12]. A comparison of LFP traces from different locations is presented in Fig. 1.2. Recording LFP gives information about population activity such

DOI:10.15774/PPKE.ITK.2023.003

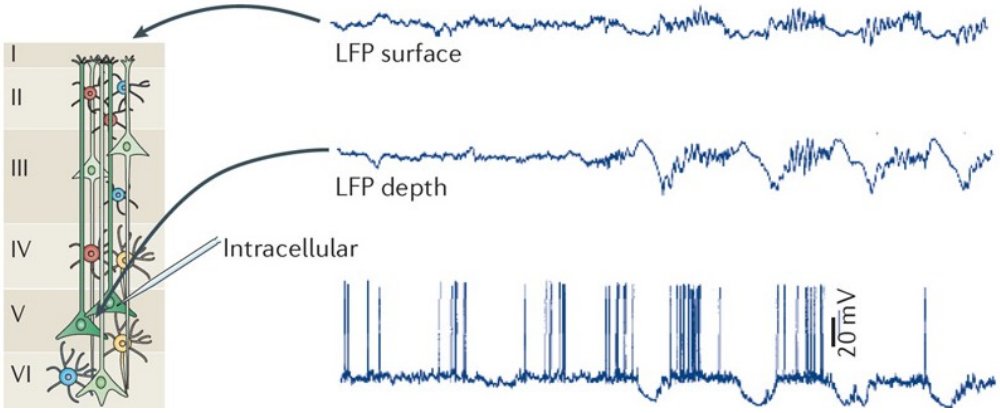

Figure 1.2: Simultaneously recorded LFP traces from the superficial ('surface') and deep ('depth') layers of the cortex and an intracellular trace from a layer 5 pyramidal neuron [12].

as neural oscillation. One technique to record LFPs is electrocorticography (ECoG), or intracranial electroencephalogram (iEEG) when the electrodes are placed directly onto the exposed brain surface. This invasive technique mainly records electrical activity from the superficial cortical layers (Layer 1, Layer 2) and is rarely capable to record APs as well [13].

1.2. Imaging techniques

1.2.1 Fluorescence microscopy

Fluorescence microscopy is a highly sensitive, specific, and reliable tool to observe the localization of cells in a tissue. During fluorescence, an atom or molecule is temporarily excited by external radiation. From this state, when it returns to its initial, stable energy level, it emits a photon. This emitted photon is detected by the microscope to form a microscopic image [14]. This process requires special molecules, called fluorophores. Fluorophores or fluorochromes are natural or artificial molecules that are capable of fluorescence. The fluorochrome labeling of the molecules makes the desired parts of the sample visible to the microscope. These fluorochromes are characterized by their excitation and emission wavelengths. According to the Stokes shift, to obtain emission, the wavelength of the transmitted light must be smaller than the emission wavelength characteristic of the material used [15]. This difference allows one to completely filter out the exciting light and detect only the emitted signal. With this specificity, only the labeled object will be visible on the microscope image. The labeling may be direct

DOI:10.15774/PPKE.ITK.2023.003

or indirect. In the case of direct labeling, the fluorophores used directly label the cell constituents. Such is the case with DAPI (4',6-diamidino-2-phenylindole) dye, which binds to DNA. For indirect labeling, antibody-conjugated fluorophore materials such as synthetic ALEXA dyes are used. Various dyes can stain molecules separately, enabling the tracking of different molecules in the same sample. The operation of the popular fluorescence microscopes relies on epifluorescence, where the excitation light and the emission light beam go through the same light path. Next to the excitation and emission filter, the dichroic mirror is another essential part of the microscope. This mirror separates the excitation light from the emitted light. The schematic structure of a fluorescence microscope is shown in Fig.1.3.

During my research work, described in Chapter 2, I analyzed fluorescent microscope images, stained by DAPI. DAPI is a blue fluorescent stain that binds to the adenine-thymine-rich DNA regions [16]. This stain can be used both in fixed and live cells since it can pass through the intact cell membrane [17]. Its excitation peak is at a wavelength of 359 nm and its emission peak is at 457 nm.

1.2.2 Two-photon microscopy

Most of the biological tissues strongly scatter light which prevents high-resolution deep imaging with traditional fluorescence microscopy. Two-photon microscopy overcomes this problem and enables deep imaging with the concept of two-photon absorption. The two photons combine their energy when they arrive simultaneously (around 0.5 fs) at the molecule to excite it (Fig. 1.4.). Multiple photons increase the light-matter interaction that causes the nonlinear nature of this imaging technique [19]. Using near-infrared light (700-1000 nm) not only achieves deep penetration depth but also is less phototoxic compared to single-photon methods [20]. The submicron spatial resolution and the brightness of emitted fluorescence light make this technology suitable for studying subcellular processes in living tissue [21].

Calcium imaging with two-photon microscopy is a widely used technique for imaging neural activity in vivo [22]. Ca^{2+} ions have a crucial part in the transmission of depolarization signal, therefore it is partially responsible for neural signaling [23]. The used calcium indicators are either chemicals or genetically encoded as the most commonly used GCaMP (GFP-Calmodulin-M13-Protein) [24]. The temporal resolution of Ca^{2+} imaging is limited by the intracellular calcium-binding kinetics (>100 ms) [25].

DOI:10.15774/PPKE.ITK.2023.003

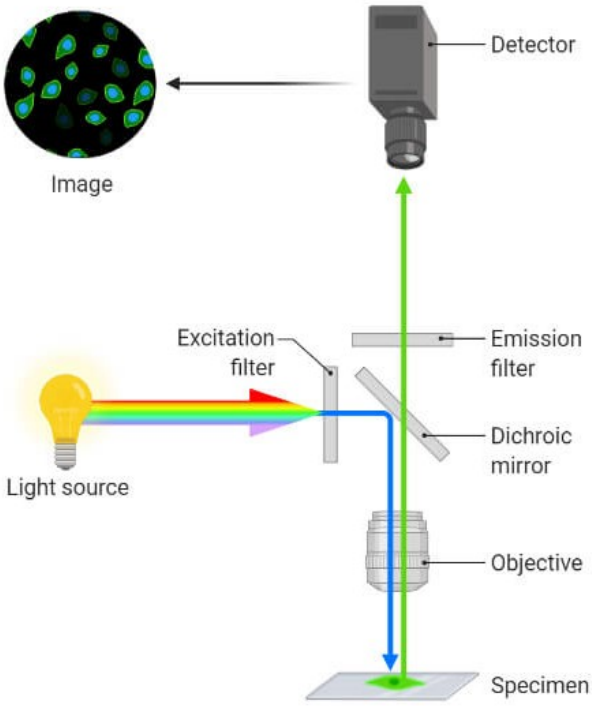

Figure 1.3: Schematic structure of fluorescence microscope. The excitation light and the emitted light pass over the same objective and the dichroic mirror directs the filtered excitation light from the light source to the specimen. From the specimen, the emitted light passes the mirror and the emission filter before reaching the detector. The filters allow fluorochrome-specific excitation and detection. [18]

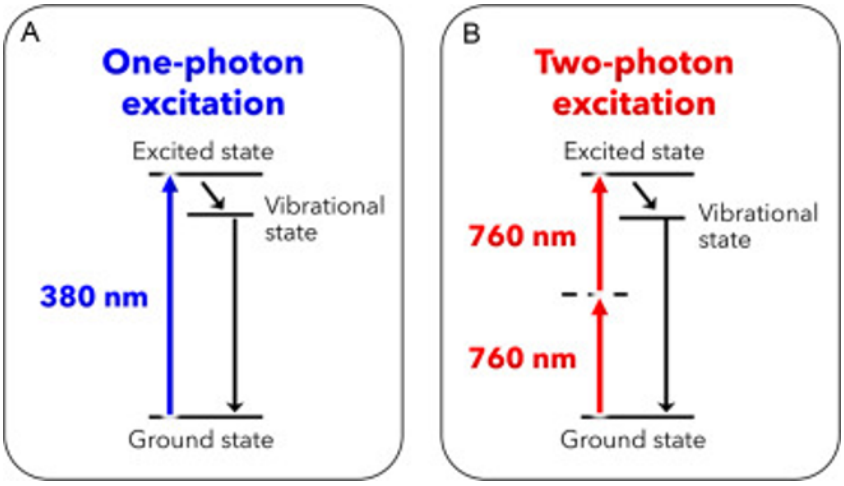

Figure 1.4: Jablonski diagram of one (A) and two-photon excitation (B). In the case of two-photon excitation, the wavelength of one photon is higher which enables the deep penetration of the tissue [26]

DOI:10.15774/PPKE.ITK.2023.003

1.2.3 Photoelectric artefact

The increasing number of research combining optical imaging and electrophysiological devices highlighted the role of photoelectric artefacts generated by optical excitation. These artefacts appear when the photoelectric effect occurs. Photoelectric effect is when voltage or current is generated in the material during light exposure. It was observed first time by Alexandre Edmond Becquerel in 1839 and Albert Einstein got a Nobel prize for the detailed description of the effect. The crucial criterion for the voltage/ current generation is that the light should achieve a threshold frequency level to dislodge the electrons in the material. The threshold frequency depends on the material properties: the energy difference between the valence band and the conduction band. The necessary energy can be modified by doping, the alteration of the energy gap between the electron bands decreases the threshold for photoactivation. The injected and absorbed energy is released in time. The mechanism of energy emission is different depending on the material. These various photoactivation types are summarized in Fig. 1.5.

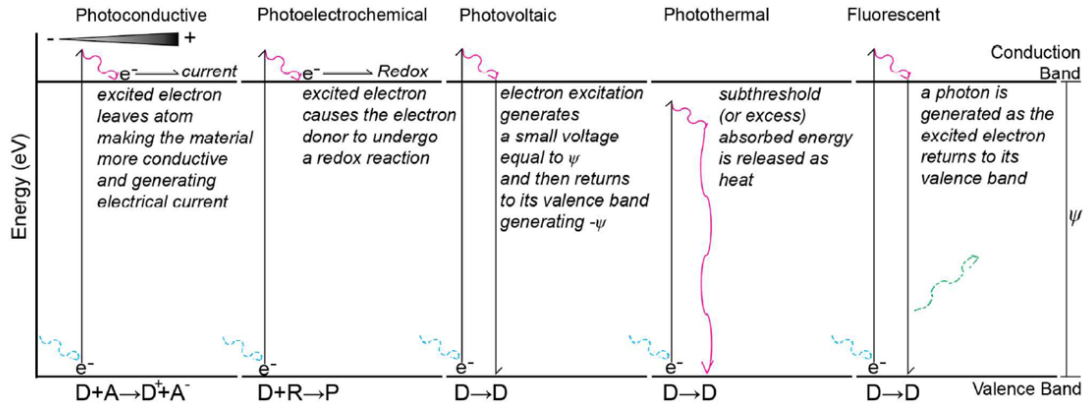

Figure 1.5: Representation of different modes of photoactivation. A high-energy light (blue light) excites an electron in the atom or molecule (represented with D). The further notations are the following: A - electron acceptor, R - reactant, P - product of a redox reaction [27].

I would like to highlight the photovoltaic mode, when excited the electrons are not separated from their holes in a purely solid-state device. In this case, there is no electric field bias and photocurrent out of the device is restricted, so the excited electron generates a small voltage. Adding together these small voltages depending on the surface area, the photovoltaic effect can generate large electrical artefacts during electrophysiology recording [27]. Besides material properties, the light source can also alter the necessary

DOI:10.15774/PPKE.ITK.2023.003

energy level to achieve a photoelectric effect. The usage of two or multiple photons instead of one also reduces the cutoff threshold [28]. A more precise description of photoelectric effects needs a deeper quantum physical introduction which is not within the scope of this dissertation.

1.3. Image processing techniques

Microscopic imaging techniques allow the investigation of various biological phenomena to researchers. Biologists often analyze these visualizations manually, for example by watching a video frame by frame. With the more advanced techniques, more raw data is generated which increases the necessary work and time to inspect the samples manually. This evolution of imaging techniques requires accurate automatic analyzing methods. Traditional image processing algorithms are the base theory behind the development of a biological image processing program. Three main steps are usually used in the case of images: gray-level transformation and binarization, image filtering, and image segmentation [29]. The main purposes of these steps are to enhance visibility, detect the searched objects, and measure the useful parameters of these objects. Gray-level transformation is a great method to reduce the data size of a three-dimensional color image. Also, the contrast can be enhanced by rescaling the pixel values. Binarization is an important method to separate the foreground and background from each other by converting the gray-level pixel value into a white or black pixel. This conversion is usually done by thresholding. In most cases, global thresholding does not give an appropriate result. During adaptive or local thresholding, the threshold value used for binarization is calculated locally, and a different value is obtained for each pixel. Using this approach, the ratio of the pixels relative to each other is taken into account as much as possible during the dimension reduction [30].

Cells and tissue have intrinsic fluorescence called autofluorescence, which causes an inferior signal-to-noise ratio [31]. Also, other external noises require image filtering before segmentation. The different linear and nonlinear filters aim to improve image quality. Smoothing is a popular solution to equalize the noise and improve the signal-noise ratio [32].

Image analysis methods used for the segmentation of biological samples include thresholding, segmentation considering morphology (shape), region growth, Watershed method, and clustering [33]. These are usually preceded by pre-processing which helps the final segmentation accuracy. Pre-processing can include conversion to a grayscale image, bi-

DOI:10.15774/PPKE.ITK.2023.003

narization, and noise filtering. Morphological opening is one of the methods of erasing minor error points resulting from imaging [34]. Keeping the morphology of the object in the binary image, the area of the object is reduced by removing the pixels on its edges. This process is called erosion. After erosion the next part of the morphological opening is dilation. The areas are increased by the same amount as the pixel value taken, so the objects get their original size back while the noises, smaller than the used pixel number, are deleted.

K-means clustering is also a procedure used in several places. The essence of the iterative algorithm is to group data points into given K classes in such a way as to minimize the distance between the data point and the center of the group. The center points are calculated from the average of the points belonging to the group. The initial centers are selected with a random generator, then the data points belonging to a cluster are determined by calculating the distances, and then the new center is determined by another average calculation. This iteration continues until the center of the group stabilizes[35]. Besides traditional image processing methods, artificial intelligence (AI)-based solutions are also getting popular in the case of biological samples. This trend can also be seen in various open-source software (e.g. ImageJ, CellProfiler). A recent mini-review was published where the most common AI solutions are introduced [36]. In the research work in Chapter 2, the image segmentation focuses on nucleus detection, therefore instead of introducing AI-based methods, some work about nucleus detection will be explained in the following paragraph.

Single-cell detection is an important part of image-based cellular analysis. The basis of this detection is the identification of cell nuclei. The nucleus not only helps to identify the different cells but its morphology is an essential indicator of phenotypic variation. In a model environment (either it is cell culture or in vitro sample) cells tend to overlap which is disadvantageous in terms of segmentation. In the research group of Péter Horváth in Szeged, the model of gas of circles was introduced [37] and developed further [38]. The 'multi-layered gas of circles' model can handle even images with multiple overlapping objects and segment near-circular objects as nuclei. Fig. 1.6. presents the segmentation steps of this approach. The same group also presented a deep-learning-based approach to segment nuclei [39], which helps to overcome the difficulty of collecting samples from the same conditions.

DOI:10.15774/PPKE.ITK.2023.003

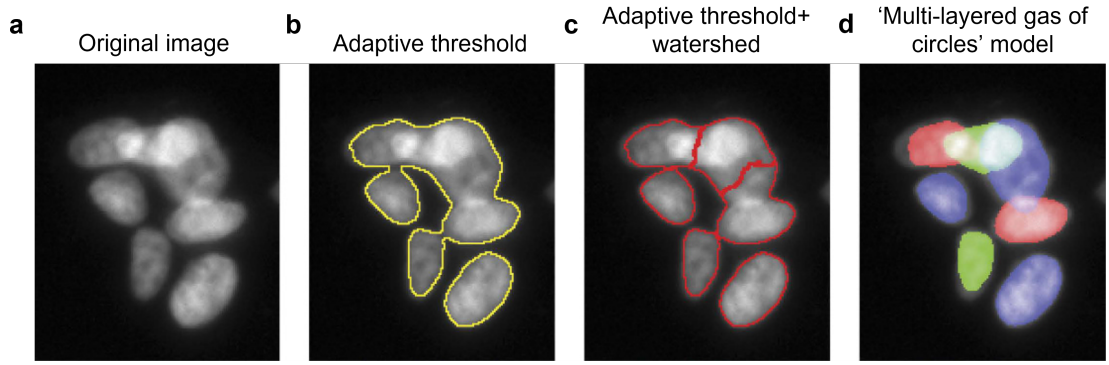

Figure 1.6: Different stage of segmentation from the research of Molnár et al. (a) Original image; (b) Result obtained by adaptive threshold using CellProfiler7; (c) Results of CellProfiler standard segmentation method containing adaptive threshold and watershed; (d) Results with the proposed "multi-layer gas of near-circles" method [38].

1.4. MEMS technologies

The development of neural implants evolves with the development of micro-electro-mechanical systems (MEMS). The microfabrication techniques allow the production of microelectrodes with various structures and materials and also with integrated electronics. The biological and biomedical application of MEMS technology is called BioMEMS. To understand the manufacturing steps of the devices in Chapters 2.2.2. and 3.2.1 I introduce the main microfabrication techniques based on the review of Ziaie [40].

1.4.1 Microfabrication techniques

The fabrication of microdevices utilizes planar technology, which consists of layer-by-layer micromachining of various conductive, dielectric, and semiconductor thin films with nanoscale precision. The combination of thin film deposition, photolithography, and etching processes leads to the formation of the final device. In this chapter, I give a brief overview of these processes.

Thin-film deposition Four main thin-film deposition techniques are used: (1) oxidation, (2) chemical vapor deposition (CVD), (3) physical vapor deposition (PVD), and (4) electrodeposition. Different materials need different deposition techniques since the properties of the deposited film are process-dependent. A high-quality thin film of oxide can be manufactured with oxidation. Typically semiconductor substrates are heated up to the range of 800 to 1200 °C in an atmosphere containing O_2 or H_2O vapor. Forming a

DOI:10.15774/PPKE.ITK.2023.003

thin film with CVD uses the reaction of chemicals in a gas phase. PVD is based on two principles: evaporation and sputtering. During evaporation, the material to be deposited is heated in a vacuum chamber containing the substrate, which causes the spreading of the layer material, and so on the top of the substrate, there will be a thin layer of the deposited material. The other method is sputtering, where the material of the desired layer is targeted by high-energy inert ions, usually argon. Due to the bombardment, individual atoms or clusters are removed from the surface and ejected toward the substrate. Electrodeposition (or electroplating) is a process typically used to obtain thick (tens of micrometers) metal structures. In the process of electrodeposition, the substrate is in a solution containing a reducible form of the ion of the desired metal while it is maintained at a negative potential (cathode) relative to a counter electrode (anode). The charge difference causes the reduction of the ions at the sample surface and the deposition of non-soluble metal atoms.

Photolithography Photolithography is a technique to transfer a pattern to the surface of the device. The substrate needs to be cleaned and dehydrated, after that, a layer of photosensitive resist is spin-coated to the surface. A pattern is transferred through a photomask, which is a glass plate with the desired pattern. The spin-coated photoresist is exposed to UV light through the created photomask. Due to this exposition, the photoresist either became soluble (positive resist) or polymerized (negative resist). The selective washing of the resist is the development, which is followed by a hard-bake step. Photolitoghrapy is often followed by an etching step.

Etching and Lift-off After lithography, the manufacturing often needs a selective material removal from the substrate. In the case of etching, the photoresist is spin-coated onto the thin-film layer, not to the substrate. In Fig.1.7 b) panel the sample material is aluminum doped zinc oxide (AZO). The development of the resist is performed as previously introduced and it is followed by the etching. Selectivity and directionality are two important indicators of any etching process. Selectivity is the degree of differentiation of the etchant between the masking material and the material to be etched. Directionality is related to the etch profile under the mask. Isotropic etch creates a semi-circular profile under the mask when the etchant attacks the material in all directions at the same rate. In the case of anisotropic etching, the dissolution is directional specific, so straight sidewalls can be manufactured. Another classification is dry and wet etching. Wet etchants are mostly isotropic and show better material selectivity than most dry etchants.

DOI:10.15774/PPKE.ITK.2023.003

The achievable minimum feature size is >3 µm, due to the lateral undercut. Dry etching shows a smaller undercut and higher anisotropicity, which allows smaller pattern lines and high aspect ratio vertical structures. One of the dry etching techniques, which is used in Chapter 3 is Reactive Ion Etching (RIE), more specifically the Depp Reactive Ion Etching (DRIE). During RIE, the sample is in a chemically active plasma. Ions from this plasma collide with the surface, which activates the surface and enables the reactive species to react with the material. DRIE is a modified version of RIE to further increase etch anisotropy.

In lift-off processing, the thin film is applied to an existing photoresist layer (Fig.1.7 a) The thin film is deposited only after the development of the resist. The actual lift-off removes the resist structure and the deposited material thereon together. The desired material remains on the substrate where there was no resist. The lift-off technique is a good alternative when wet-etching is problematic (e.g. in the case of gold, silicon nitride), however, its reproducibility depends on the prevention of the sidewalls. Besides, high heating steps during coating deposition are critical to lift-off, since the photoresist is already on the substrate and it can be thermally affected [41].

DOI:10.15774/PPKE.ITK.2023.003

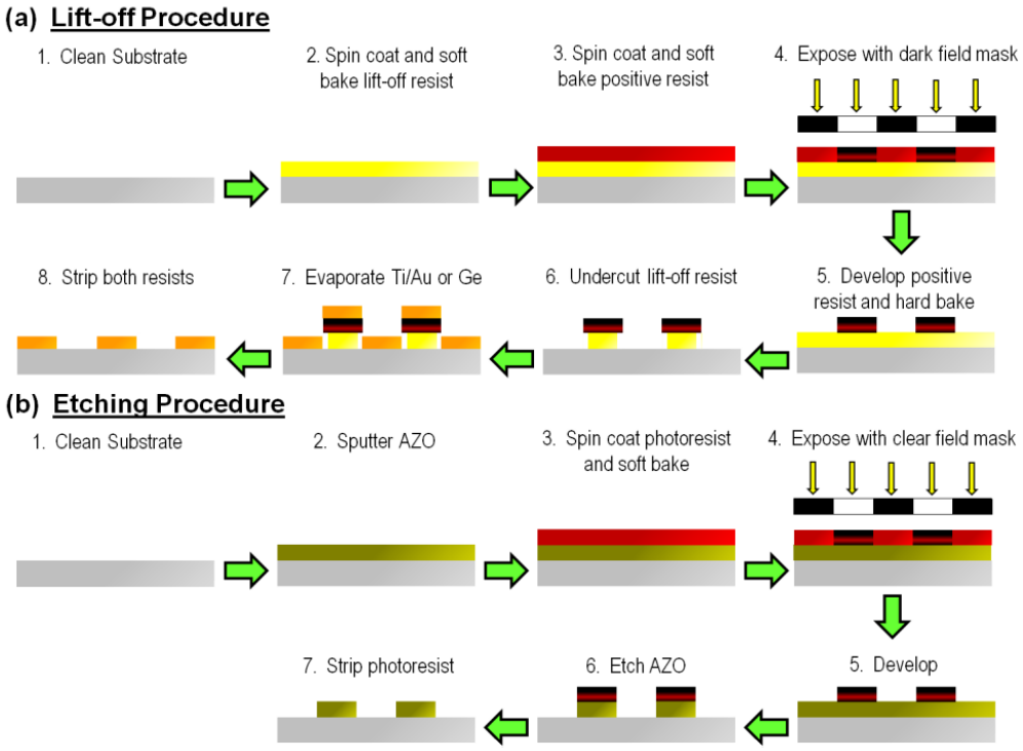

Figure 1.7: Description of UV lithography with (a) lift-off procedure and (b) etching procedure [42]. During lift-off, first a lift-off resist (yellow) is spin coated onto the clean substrate, then a positive photoresist layer (red). After the exposure with dark field mask, the photoresist became soluble where the light went through the black parts of the mask. After development the unexposed parts remain from the resist. During the undercut of the lift-off resist, only those parts remain, where there is photoresist on the top of the layer. Only at this point comes the conductive layer deposition with evaporation. The orange layer can be a Ti/Au or Ge. The final step is the removal of both resist layer, and only the patterned conductive layer remains. During etching the conductive layer is the first one on the substrate (gold), and only on top of that is the photoresist spin coated. In this case the negative photoresist is exposed with clear field mask (light goes through the white parts of the mask), and the exposed parts remain. During etching only part of the conductive layer remain, where there was photoresist on top of it. After the final photoresist removal, we get the patterned conductive layer.

DOI:10.15774/PPKE.ITK.2023.003

1.4.2 Polymer implants

During the development of neural implants, minimal invasiveness is an increasingly important aspect. New devices are proposed from a versatile, soft, flexible material that not only reduces the immune response of the brain tissue but also allows the combination of multiple imaging techniques. These new devices are mostly manufactured from different types of polymers. Polymers are suitable materials to fabricate either penetrating electrodes or surface electrodes [43]. Using polymer devices fabricated with MEMS technologies is popular due to their biocompatibility, easy fabrication with soft lithography, and the low cost and rapid prototyping methods available in plastic material [44]. Additionally, the size of microdevices reduces the tissue damage caused during the implantation.

Chronically implanted devices evoke inflammatory tissue response, which can cause device failure. To moderate this response, one effective method, based on histological studies, is to reduce the mechanical mismatch between the interface materials and tissue properties [45]. Many different material combinations were published and also reviewed the most commonly used polymers for implantables [46, 47, 48]. The most popular materials are polyimide [49], SU-8 [50], Parylene C [51], Parylene HT [51], and polydimethylsiloxane (PDMS) [52].

1.5. Biocompatibility

A foreign body interaction, such as electrode insertion, provokes a complex response called reactive gliosis. The complex process involving cell division and cell migration causes the formation of a glial scar that separates the damaged tissue from the intact. This scar tissue creates a spatial and electrical insulating effect between the neuron and the electrode [4]. Newly proliferated cells can be also found in the glial scar, which cells are not present in intact tissue. Not only does the insulating effect of the process impair the usability of the implanted electrode, but the death of neurons also negatively affects the measurement of neural activity [53].

The three main glial cell types in the central nervous system are oligodendrocytes, astrocytes, and microglia. After implantation, the activation of microglia and astrocytes has key importance in the immune response to the injury [54]. The disrupture of the blood-brain barrier (BBB) activates inflammatory pathways of the glial cells [55]. This activation causes a transformation of cell phenotype. The reactive astrocytes have an

DOI:10.15774/PPKE.ITK.2023.003

irregular nucleus, show hypertrophy, upregulation of GFAP, proliferation, and enhanced migration [4]. Similarly, microglia start to proliferate due to the activation and change their morphology to a more compact, amoeboid form. Their function in the immune response is similar to macrophage-like cells, which include producing cytotoxic and neurotoxic factors [56], that lead to neuronal cell death in a chronic application [57]. Fig.1.8 demonstrates the formation of the glial scar in time. Besides cell death, the glial scar tissue act like a low-pass filter, which hinders proper signal recording [4].

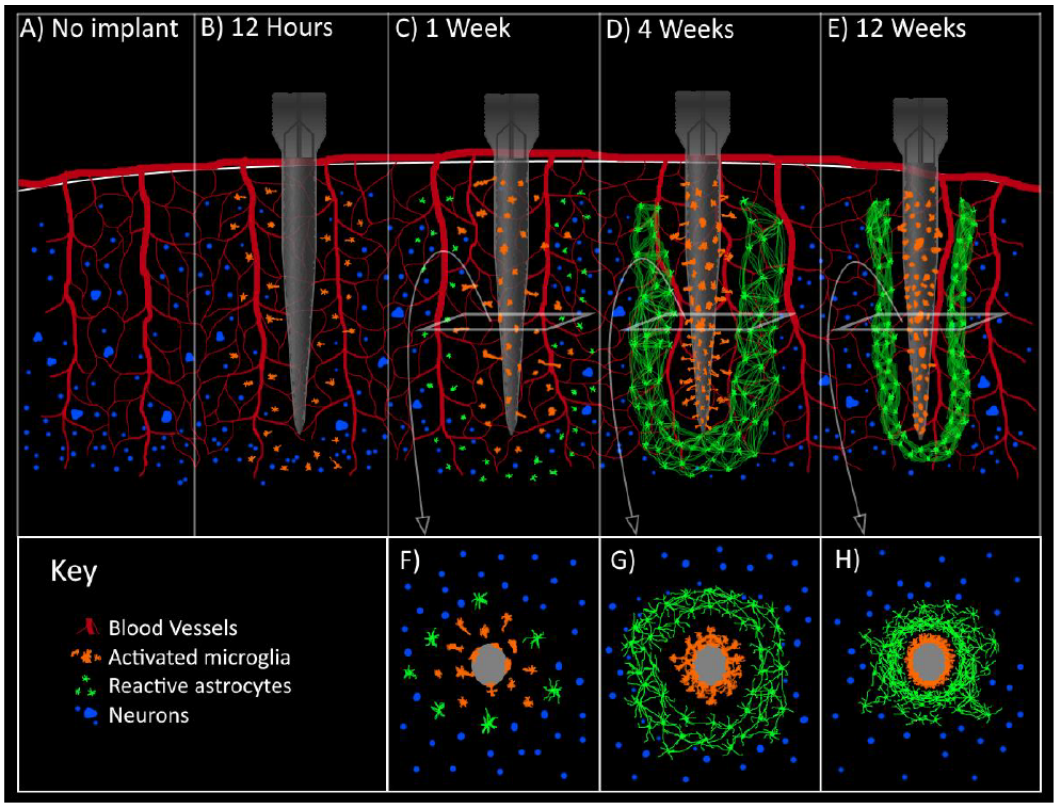

Figure 1.8: Illustration of encapsulation. The glial response (A) before the implantation, after (B) 12 hours, (C) 1 week, (D) 4 weeks, and (E) 12 weeks after the implantation. The cross-section view of the panels (C-E) is illustrated on panels (F-H) [54]

Many researchers investigate the immune response during and after the implantation to identify the best solution to reduce this immune response and achieve long-term stability. One approach to minimize the formation of encapsulating sheath is to minimize tissue damage by reducing the size of the device. Although some studies claim that the long-term functionality of the device seems to be independent of the device size, shape, surface texture [58], or insertion method [59], multiple studies introduce implantation

DOI:10.15774/PPKE.ITK.2023.003

methods to avoid or minimize tissue damage. Avoiding surface neurovasculature during implantation can cause better long-term device efficacy [60]. The geometry of the tip of the device and the insertion speed also show differences in vascular damage [61], and the insertion speed also influences the signal-noise ratio (SNR) of the recording [62]. In the case of chronic implantation, the stress originating from the micromotions between the moving brain and the implant is hypothesized to be the main reason for the neuroinflammatory response [63]. Therefore, the development of neural implants should take the mechanical aspects into account during implant design. The primary approaches based on [64] are:

- Using compliant microelectrode substrate to reduce motion-induced injury
- Preventing inflammatory cell adhesion by surface coatings
- Altering surface topography to manipulate cell phenotypes
- Reducing surgical trauma by proper architecture design
- Using bioactive materials to help electrode-tissue integration
- Using conductive polymers and nanomaterials to enhance the electrical performance

The compliant intracortical implants indeed reduce the neuroinflammatory response after two weeks of implantation [45]. The suitable polymer materials either for substrate or coatings were also reviewed by Lecomte et al. [65]. The topographical modification of the substrate is based on the crucial role of the microenvironment in cell adhesion, guidance, and scaffolding [66]. The extracellular matrix proteins exhibit nanometer-scale structure to the cells that have a major role in cell-matrix signaling [67]. This implies that engineering the substrate topography at the nanoscale can improve cell-surface interaction and helps to control cell function [68, 69].

1.6. References

[1] M. V. Sofroniew and H. V. Vinters, "Astrocytes: Biology and pathology," *Acta Neuropathologica*, vol. 119, pp. 7–35, 1 2010.

[2] A. Verkhratsky and A. Butt, *Glial physiology and pathophysiology*. Wiley-Blackwell, 2013.

[3] W. J. Streit, *Microglial cells*, pp. 85–96. Oxford University Press, USA, 1995.

DOI:10.15774/PPKE.ITK.2023.003

[4] V. S. Polikov, P. A. Tresco, and W. M. Reichert, "Response of brain tissue to chronically implanted neural electrodes," *Journal of Neuroscience Methods*, vol. 148, pp. 1–18, 10 2005.

[5] E. C. Amerman, *Human anatomy & physiology*. Pearson, global edition ed., 2016.

[6] E. R. Kandel, J. H. Schwartz, T. M. Jessell, S. Siegelbaum, A. J. Hudspeth, and S. Mack, *Principles of neural science*. McGraw-Hill Professional, 5th ed., 2000.

[7] Carl Rod Nave, "Action potentials." `http://hyperphysics.phy-astr.gsu.edu/hbase/Biology/actpot.html#c1`, 2002. Accessed: 2022-07-19.

[8] V. Castagnola, *Implantable microelectrodes on soft substrate with nanostructured active surface for stimulation and recording of brain activities*. Theses, Universite Toulouse III Paul Sabatier, Dec. 2014.

[9] Y. Kajikawa and C. E. Schroeder, "Generation of field potentials and modulation of their dynamics through volume integration of cortical activity," *Journal of Neurophysiology*, vol. 113, pp. 339–351, 1 2015.

[10] R. T. Canolty, E. Edwards, S. S. Dalal, M. Soltani, S. S. Nagarajan, H. E. Kirsch, M. S. Berger, N. M. Barbaro, and R. T. Knight, "High gamma power is phase-locked to theta oscillations in human neocortex," *science*, vol. 313, no. 5793, pp. 1626–1628, 2006.

[11] H. Petsche, H. Pockberger, and P. Rappelsberger, "On the search for the sources of the electroencephalogram," *Neuroscience*, vol. 11, pp. 1–27, 1 1984.

[12] G. Buzsáki, C. A. Anastassiou, and C. Koch, "The origin of extracellular fields and currents — eeg, ecog, lfp and spikes," *Nature Reviews Neuroscience 2012 13:6*, vol. 13, pp. 407–420, 5 2012.

[13] D. Khodagholy, J. N. Gelinas, T. Thesen, W. Doyle, O. Devinsky, G. G. Malliaras, and G. Buzsáki, "Neurogrid: recording action potentials from the surface of the brain," *Nature Neuroscience 2015 18:2*, vol. 18, pp. 310–315, 12 2014.

[14] B. Valeur and M. Berberan-Santos, *Molecular fluorescence: principles and applications*. Wiley-VCH, 2012.

[15] J. W. Lichtman and J.-A. Conchello, "Fluorescence microscopy," *Nature methods*, vol. 2, no. 12, pp. 910–919, 2005.

[16] J. Kapuscinski, "Dapi: a dna-specific fluorescent probe," *Biotechnic & Histochemistry*, vol. 70, no. 5, pp. 220–233, 1995. PMID: 8580206.

[17] B. I. Tarnowski, F. G. Spinale, and J. H. Nicholson, "Dapi as a useful stain for nuclear quantitation," *Biotechnic and Histochemistry*, vol. 66, pp. 296–302, 1991.

[18] X. Wang and Y. Lai, "Three basic types of fluorescence microscopy and recent improvement," *E3S Web of Conferences*, vol. 290, p. 01031, 2021.

[19] F. Helmchen and W. Denk, "Deep tissue two-photon microscopy," *Nature Methods 2005 2:12*, vol. 2, pp. 932–940, 11 2005.

[20] J. Nakai, M. Ohkura, and K. Imoto, "A high signal-to-noise ca2+ probe composed of a single green fluorescent protein," *Nature Biotechnology 2001 19:2*, vol. 19, pp. 137–141, 2001.

[21] Z. F. Mainen, M. Maletic-Savatic, S. H. Shi, Y. Hayashi, R. Malinow, and K. Svoboda, "Two-photon imaging in living brain slices," *Methods*, vol. 18, pp. 231–239, 6 1999.

[22] K. Ohki, S. Chung, Y. H. Ch'ng, P. Kara, and R. C. Reid, "Functional imaging with cellular resolution reveals precise micro-architecture in visual cortex," *Nature 2005 433:7026*, vol. 433, pp. 597–603, 1 2005.

[23] M. Brini, T. Calì, D. Ottolini, and E. Carafoli, "Neuronal calcium signaling: function and dysfunction," *Cellular and molecular life sciences*, vol. 71, no. 15, pp. 2787–2814, 2014.

[24] T. W. Chen, T. J. Wardill, Y. Sun, S. R. Pulver, S. L. Renninger, A. Baohan, E. R. Schreiter, R. A. Kerr, M. B. Orger, V. Jayaraman, L. L. Looger, K. Svoboda, and D. S. Kim, "Ultrasensitive fluorescent proteins for imaging neuronal activity," *Nature 2013 499:7458*, vol. 499, pp. 295–300, 7 2013.

[25] N. Helassa, B. Podor, A. Fine, and K. Török, "Design and mechanistic insight into ultrafast calcium indicators for monitoring intracellular calcium dynamics," *Scientific Reports 2016 6:1*, vol. 6, pp. 1–14, 12 2016.

[26] J. G. Croissant and J. O. Durand, "Mesoporous silica-based nanoparticles for light-actuated biomedical applications via near-infrared two-photon absorption," *Enzymes*, vol. 43, pp. 67–99, 1 2018.

DOI:10.15774/PPKE.ITK.2023.003

[27] T. D. Kozai and A. L. Vazquez, "Photoelectric artefact from optogenetics and imaging on microelectrodes and bioelectronics: new challenges and opportunities," *Journal of Materials Chemistry B*, vol. 3, pp. 4965–4978, 6 2015.

[28] M. Göppert-Mayer, "Über elementarakte mit zwei quantensprüngen," *Annalen der Physik*, vol. 401, pp. 273–294, 1 1931.

[29] S. Uchida, "Image processing and recognition for biological images," *Development, Growth & Differentiation*, vol. 55, pp. 523–549, 5 2013.

[30] P. K. Sahoo, S. Soltani, and A. K. Wong, "A survey of thresholding techniques," *Computer Vision, Graphics, and Image Processing*, vol. 41, pp. 233–260, 2 1988.

[31] M. Monici, "Cell and tissue autofluorescence research and diagnostic applications," *Biotechnology Annual Review*, vol. 11, pp. 227–256, 1 2005.

[32] C. P. Behrenbruch, S. Petroudi, S. Bond, J. D. Declerck, F. J. Leong, and J. M. Brady, "Image filtering techniques for medical image post-processing: An overview," *British Journal of Radiology*, vol. 77, 2004.

[33] H. Irshad, A. Veillard, L. Roux, and D. Racoceanu, "Methods for nuclei detection, segmentation, and classification in digital histopathology: A review-current status and future potential," *IEEE Reviews in Biomedical Engineering*, vol. 7, pp. 97–114, 2014.

[34] L. Vincent, "Morphological area openings and closings for grey-scale images," in *Shape in Picture*, pp. 197–208, Springer, Berlin, Heidelberg, 1994.

[35] A. Likas, N. Vlassis, and J. J. Verbeek, "The global k-means clustering algorithm," *Pattern Recognition*, vol. 36, pp. 451–461, 2 2003.

[36] M. S. Durkee, R. Abraham, M. R. Clark, and M. L. Giger, "Artificial intelligence and cellular segmentation in tissue microscopy images," *The American Journal of Pathology*, vol. 191, pp. 1693–1701, 10 2021.

[37] P. Horváth, I. H. Jermyn, Z. Kato, and J. Zerubia, "A higher-order active contour model of a 'gas of circles' and its application to tree crown extraction," *Pattern Recognition*, vol. 42, pp. 699–709, 5 2009.

[38] C. Molnar, I. H. Jermyn, Z. Kato, V. Rahkama, P. Östling, P. Mikkonen, V. Pietiaïnen, and P. Horvath, "Accurate morphology preserving segmentation of overlapping cells based on active contours," *Scientific Reports 2016 6:1*, vol. 6, pp. 1–10, 8 2016.

[39] R. Hollandi, A. Szkalisity, T. Toth, E. Tasnadi, C. Molnar, B. Mathe, I. Grexa, J. Molnar, A. Balind, M. Gorbe, M. Kovacs, E. Migh, A. Goodman, T. Balassa, K. Koos, W. Wang, J. C. Caicedo, N. Bara, F. Kovacs, L. Paavolainen, T. Danka, A. Kriston, A. E. Carpenter, K. Smith, and P. Horvath, "nucleaizer: A parameter-free deep learning framework for nucleus segmentation using image style transfer," *Cell Systems*, vol. 10, pp. 453–458.e6, 5 2020.

[40] B. Ziaie, A. Baldi, M. Lei, Y. Gu, and R. A. Siegel, "Hard and soft micromachining for biomems: review of techniques and examples of applications in microfluidics and drug delivery," *Advanced Drug Delivery Reviews*, vol. 56, pp. 145–172, 2 2004.

[41] MicroChemicals GmbH, "Lift-off processes with photoresist." `https://www.microchemicals.com/technical_information/lift_off_photoresist.pdf`, 2018. Accessed: 2022-07-19.

[42] C. Greenlee, J. Luo, K. Leedy, B. Bayraktaroglu, R. A. Norwood, M. Fallahi, A. K.-Y. Jen, N. Peyghambarian, D. S. Monaghan, U. Gopinathan, B. M. Hennelly, D. P. Kelly, T. J. Naughton, and J. T. Sheridan, "Electro-optic polymer spatial light modulator based on a fabry–perot interferometer configuration," *Optics Express, Vol. 19, Issue 13, pp. 12750-12758*, vol. 19, pp. 12750–12758, 6 2011.

[43] G. H. Kim, K. Kim, E. Lee, T. An, W. Choi, G. Lim, and J. H. Shin, "Recent progress on microelectrodes in neural interfaces," *Materials*, vol. 11, no. 10, p. 1995, 2018.

[44] R. Bashir, "Biomems: state-of-the-art in detection, opportunities and prospects," *Advanced Drug Delivery Reviews*, vol. 56, pp. 1565–1586, 9 2004.

[45] J. K. Nguyen, D. J. Park, J. L. Skousen, A. E. Hess-Dunning, D. J. Tyler, S. J. Rowan, C. Weder, and J. R. Capadona, "Mechanically-compliant intracortical implants reduce the neuroinflammatory response," *Journal of Neural Engineering*, vol. 11, p. 056014, 8 2014.

[46] Z. Fekete and A. Pongrácz, "Multifunctional soft implants to monitor and control neural activity in the central and peripheral nervous system: A review," *Sensors and Actuators B: Chemical*, vol. 243, pp. 1214–1223, 5 2017.

[47] L. J. Tang, M. H. Wang, H. C. Tian, X. Y. Kang, W. Hong, and J. Q. Liu, "Progress in research of flexible mems microelectrodes for neural interface," *Micromachines 2017, Vol. 8, Page 281*, vol. 8, p. 281, 9 2017.

[48] R. Green and M. R. Abidian, "Conducting polymers for neural prosthetic and neural interface applications," *Advanced Materials*, vol. 27, pp. 7620–7637, 12 2015.

[49] A. Zátonyi, Z. Borhegyi, M. Srivastava, D. Cserpán, Z. Somogyvári, Z. Kisvárday, and Z. Fekete, "Functional brain mapping using optical imaging of intrinsic signals and simultaneous high-resolution cortical electrophysiology with a flexible, transparent microelectrode array," *Sensors and Actuators B: Chemical*, vol. 273, pp. 519–526, 11 2018.

[50] S. N. Obaid, R. T. Yin, J. Tian, Z. Chen, S. W. Chen, K. B. Lee, N. Boyajian, A. N. Miniovich, I. R. Efimov, L. Lu, S. N. Obaid, R. T. Yin, J. Tian, Z. Chen, S. W. Chen, K. B. Lee, N. Boyajian, A. N. Miniovich, I. R. Efimov, and L. Lu, "Multifunctional flexible biointerfaces for simultaneous colocalized optophysiology and electrophysiology," *Advanced Functional Materials*, vol. 30, p. 1910027, 6 2020.

[51] W. Yang, Y. Gong, C. Y. Yao, M. Shrestha, Y. Jia, Z. Qiu, Q. H. Fan, A. Weber, and W. Li, "A fully transparent, flexible pedot:pss–ito–ag–ito based microelectrode array for ecog recording," *Lab on a Chip*, vol. 21, pp. 1096–1108, 3 2021.

[52] A. F. Renz, J. Lee, K. Tybrandt, M. Brzezinski, D. A. Lorenzo, C. Cheraka, J. Lee, F. Helmchen, J. Vörös, C. M. Lewis, A. F. Renz, J. Lee, K. Tybrandt, M. Brzezinski, M. C. Cheraka, J. Vörös, D. A. Lorenzo, F. Helmchen, and C. M. Lewis, "Opto-edura: A soft, stretchable ecog array for multimodal, multiscale neuroscience," *Advanced Healthcare Materials*, vol. 9, p. 2000814, 9 2020.

[53] M. V. Sofroniew, "Molecular dissection of reactive astrogliosis and glial scar formation," *Trends in Neurosciences*, vol. 32, pp. 638–647, 12 2009.

[54] A. Campbell and C. Wu, "Chronically implanted intracranial electrodes: Tissue reaction and electrical changes," *Micromachines 2018, Vol. 9, Page 430*, vol. 9, p. 430, 8 2018.

[55] T. D. Kozai, A. S. Jaquins-Gerstl, A. L. Vazquez, A. C. Michael, and X. T. Cui, "Brain tissue responses to neural implants impact signal sensitivity and intervention strategies," *ACS Chemical Neuroscience*, vol. 6, pp. 48–67, 1 2015.

[56] K. Nakajima, S. Honda, Y. Tohyama, Y. Imai, S. Kohsaka, and T. Kurihara, "Neurotrophin secretion from cultured microglia," *Journal of Neuroscience Research*, vol. 65, pp. 322–331, 8 2001.

[57] R. Biran, D. C. Martin, and P. A. Tresco, "Neuronal cell loss accompanies the brain tissue response to chronically implanted silicon microelectrode arrays," *Experimental Neurology*, vol. 195, pp. 115–126, 9 2005.

[58] D. H. Szarowski, M. D. Andersen, S. Retterer, A. J. Spence, M. Isaacson, H. G. Craighead, J. N. Turner, and W. Shain, "Brain responses to micro-machined silicon devices," *Brain Research*, vol. 983, pp. 23–35, 9 2003.

[59] M. Welkenhuysen, A. Andrei, L. Ameye, W. Eberle, and B. Nuttin, "Effect of insertion speed on tissue response and insertion mechanics of a chronically implanted silicon-based neural probe," *IEEE Transactions on Biomedical Engineering*, vol. 58, pp. 3250–3259, 11 2011.

[60] C. S. Bjornsson, S. J. Oh, Y. A. Al-Kofahi, Y. J. Lim, K. L. Smith, J. N. Turner, S. De, B. Roysam, W. Shain, and S. J. Kim, "Effects of insertion conditions on tissue strain and vascular damage during neuroprosthetic device insertion," *Journal of Neural Engineering*, vol. 3, p. 196, 6 2006.

[61] T. D. Kozai, T. C. Marzullo, F. Hooi, N. B. Langhals, A. K. Majewska, E. B. Brown, and D. R. Kipke, "Reduction of neurovascular damage resulting from microelectrode insertion into cerebral cortex using in vivo two-photon mapping," *Journal of neural engineering*, vol. 7, p. 046011, 8 2010.

[62] R. Fiáth, A. L. Márton, F. Mátyás, D. Pinke, G. Márton, K. Tóth, and I. Ulbert, "Slow insertion of silicon probes improves the quality of acute neuronal recordings," *Scientific Reports 2019 9:1*, vol. 9, pp. 1–17, 1 2019.

[63] Y. T. Kim, R. W. Hitchcock, M. J. Bridge, and P. A. Tresco, "Chronic response of adult rat brain tissue to implants anchored to the skull," *Biomaterials*, vol. 25, pp. 2229–2237, 5 2004.

[64] M. Jorfi, J. L. Skousen, C. Weder, and J. R. Capadona, "Progress towards biocompatible intracortical microelectrodes for neural interfacing applications," *Journal of Neural Engineering*, vol. 12, p. 011001, 12 2014.

[65] A. Lecomte, E. Descamps, and C. Bergaud, "A review on mechanical considerations for chronically-implanted neural probes," *Journal of Neural Engineering*, vol. 15, p. 031001, 3 2018.

DOI:10.15774/PPKE.ITK.2023.003

[66] D.-H. Kim, P. P. Provenzano, C. L. Smith, and A. Levchenko, "Matrix nanotopography as a regulator of cell function," *Journal of Cell Biology*, vol. 197, no. 3, pp. 351–360, 2012.

[67] K. V. D. Mark, J. Park, S. Bauer, and P. Schmuki, "Nanoscale engineering of biomimetic surfaces: Cues from the extracellular matrix," *Cell and Tissue Research*, vol. 339, pp. 131–153, 1 2010.

[68] C. J. Bettinger, R. Langer, and J. T. Borenstein, "Engineering substrate topography at the micro- and nanoscale to control cell function," *Angewandte Chemie International Edition*, vol. 48, pp. 5406–5415, 7 2009.

[69] J. Luo, M. Walker, Y. Xiao, H. Donnelly, M. J. Dalby, and M. Salmeron-Sanchez, "The influence of nanotopography on cell behaviour through interactions with the extracellular matrix – a review," *Bioactive Materials*, vol. 15, pp. 145–159, 9 2022.

DOI:10.15774/PPKE.ITK.2023.003

Chapter 2

SU-8 microstructure and astroglia interaction

2.1. Introduction

The diagnostic and therapeutic role of neural implants in the clinical setting is increasing. One of the key issues in the rapidly evolving field is how we can mitigate the inflammatory response of the surrounding tissue, which deteriorates the long-term functionality of implants. One intensively investigated alternative is to imitate the extracellular matrix (ECM) by modifying the chemical or physical properties of the device. The ECM presents essential molecular and topographical cues to cells, which regulate adhesion, cell growth, and cellular connections within the tissue [1]. In the case of neural tissue, the environment of the neurons is defined mostly by the glial cells. These cells are responsible for the protection of neurons, nutrition, or neurotransmitter balance [2, 3, 4]. Astrocytes play an important role in the evolution of the glial scar, as well. In response to an implant penetration into the tissue microglial cells become activated. The inflammatory signals lead to an increased number of activated astrocyte [5] and eventually inhibits long-term electrophysiological measurement or efficient electric stimulation. The schematic representation of the formation of the glial scar is shown in Fig. 2.1.

It is under investigation whether micro-and nanofabricated implant surfaces can reduce this effect. Biomaterial surfaces can be patterned by photolithography, microcontact printing, microfluidic patterning, or electrospinning [6], while inorganic, submicron-scale topography can be created using laser holography [7], or electron beam lithography [8]. The most extensively examined parameters are the geometry, roughness, and orientation of the surfaces because these parameters can be easily engineered. To create highly

DOI:10.15774/PPKE.ITK.2023.003

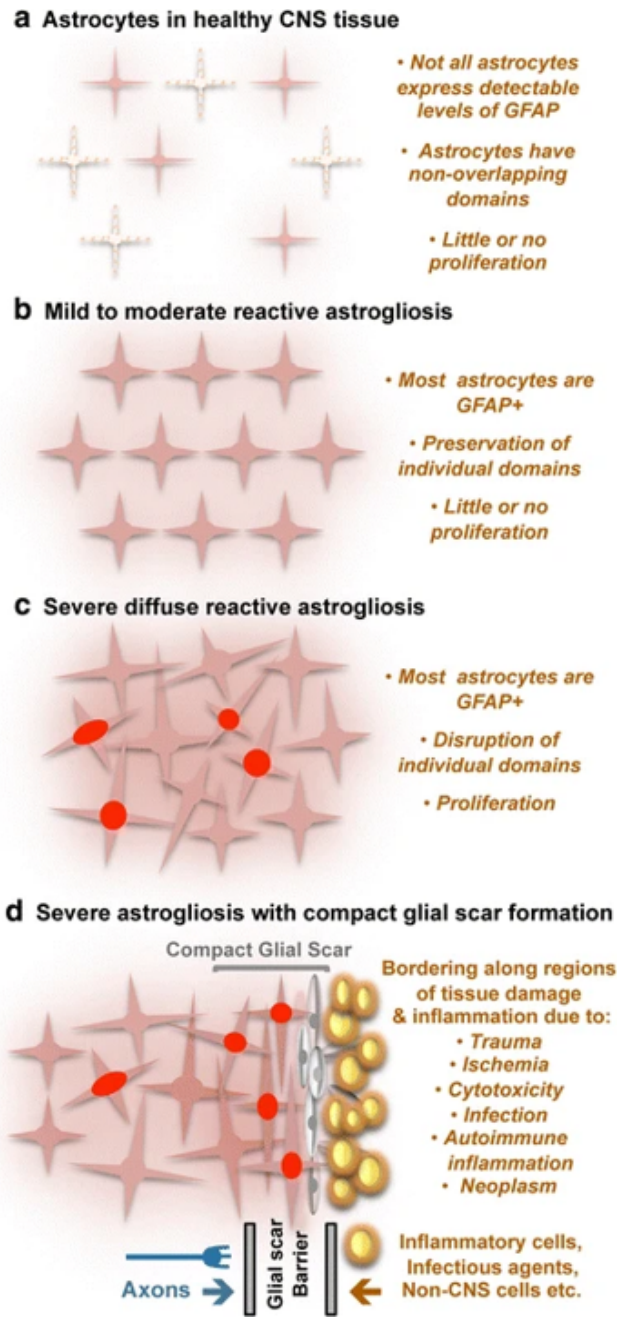

Figure 2.1: Schematic representations of reactive astrogliosis at various extents. a) Astrocytes in healthy CNS tissue. b) Mild to moderate reactive astrogliosis comprises variable changes in molecular expression, functional activity, and variable degrees of cellular hypertrophy. c) Severe diffuse reactive astrogliosis includes substantial changes in molecular expression, functional activity, and cellular hypertrophy. d) Severe reactive astrogliosis with compact glial scar. The overt tissue damage and inflammation define the border of the scar formation. Newly proliferated astrocytes (with red nuclei in the figure) and other cell types (gray in the figure) such as fibromeningeal cells and other glial cells participate in scar formation [3].

DOI:10.15774/PPKE.ITK.2023.003

biocompatible devices showing long-term stability, the response of nearby glial cells to various materials and topography is essential [9, 10, 11]. Human astrocytes can attach to artificial surface relief grating and this pattern affects the elongation of the cells even at a shallower, 250 nm deep groove [7]. Lee et al. studied C6 glioma cells on nanodot arrays based on tantalum nitride thin films [12]. Between the range of 10 to 200 nm dot diameter, the presence of 100-200 nm nanodots reduced focal adhesion, decelerated gap junction protein Cx43 transport, and reduced branch point and mesh numbers. To reduce astrogliosis, nanoporous gold was also suggested by Chapman [13]. The length scale of the nanoporous gold is tunable. By changing the topography, astrocytic coverage can be reduced, while maintaining high neuronal coverage. The random topography of the nanoporous gold surface also inhibits the spreading of astrocytes. The effect of changes in topography was also examined in the case of electrospun fibers, where the diameter dependency was investigated [14]. Researchers found a significant increase in astrocyte elongation in the presence of 808 nm diameter fibers. Due to this elongation, the neuroprotective properties of the glial cells have increased.

Many research groups investigate the effect of surface morphology on cell shape or the cytoskeleton. At the same time, investigating nucleus deformation can provide novelty, since the nucleus deformation regulates gene expression [15] and the change in the nucleus morphology is a rarely researched parameter in surface-cell studies. Detecting the nucleus is a more straightforward problem than detecting the cytoskeleton and it allows more precise detection and fast data processing. In astrogliosis research, it is worthwhile to examine changes in nucleus size, because "the area of the nucleus is directly proportional to the state of reactivity of the astrocyte" [16]. It has been reported that the cell nucleus is also sensitive to microstructured surfaces since it shows viscoelastic properties [17]. Due to the interconnected network that the cytoskeleton forms around the nucleus, the nucleus shows deformation caused by cytoskeleton attachment [18]. In Fig. 2.2. some of the different mechanical and topographical stimuli and the distorted nuclei are illustrated. To control the nucleus by the alteration of topography, bone marrow stromal cells were seeded onto poly(d,l-lactide-co-glycolide) micropillars [19]. The results show that the topography determines the nucleus orientation and that strain has a negligible effect. The connection between cell nucleus deformation and cytoskeleton attachment enables analyzing only the nucleus to study topographical effects. Nucleus detection is more easily resolved since the shape of the nuclei is more homogenous than the cytoskeleton. Therefore, nucleus detection can be automated enabling less time-consuming data analysis.

DOI:10.15774/PPKE.ITK.2023.003

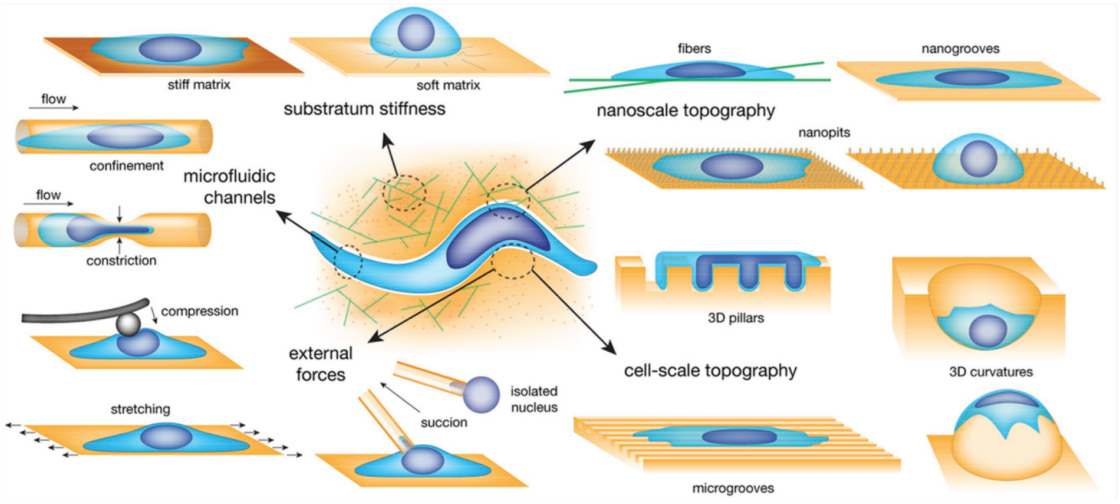

Figure 2.2: Different approaches induce mechanical and topographical stimuli to cells. The cell senses and reacts to the different substrate stiffness, underlying topography, external forces, and confinement. The schematic figures show the various methods to model the different influences. [14]

Cell growth on flat and patterned SU-8 surfaces was compared by Eunhee Kim et al. [20], seeding PC12 cells (cell line derived from a rat adrenal medullary tumor, pheochromocytoma) onto nanopatterned microprobes with 200 nm diameter and depth, aligned to the cell size. The evaluation found that attachment and neurite outgrowth of the neuron-like cells significantly increased on the nanostructured surface compared with the bare SU-8 surface already on day 1. Another study used a quasi-three-dimensional SU-8 microwell structure, cultured with SH-SY5Y human neuroblastoma cells [21]. With confocal microscopy and the potentiometric fluorescent dye TMRM, the cell resting membrane potential was measured, and it was found that the microwell network promotes the cell resting membrane potential establishment. These results show that topographical changes in the substrate lead to changes in cellular function.

In my work, the effect of the SU-8 micropattern on astrocyte nuclei shortly after the surface attachment of the cells was investigated. The biocompatibility of SU-8 has been examined in detail by KV. Nemani [22]. Its biocompatibility specifically with the central nervous system has also been investigated [23]. Patterning of this polymer is feasible using traditional microlithography techniques [24, 25], which allows a low-cost fabrication. SU-8 is also suitable to form high-aspect-ratio microstructures with diverse shapes [26]. The easy detection of the cell nucleus and its important role in cell reaction to the topography also inspired me to investigate the effect of SU-8-based microstructures in my studies.

DOI:10.15774/PPKE.ITK.2023.003

In this thesis, I provide insight into the orientation, elongation, and attachment of glial cells on a micron-scale pillar, stripe, and meander patterns in vitro with underlying SiO_2 (native oxide of bare silicon surfaces) as a reference surface through the study of the cell nuclei. This reference choice allows the comparison of silicon-based neural interfaces with additional SU-8 microstructures to improve and investigate cell guiding properties. My goal is to detect the astroglial cell nuclei with my self-developed algorithm on the created patterned surfaces and examine the effects of the different pattern sizes on the cells. The surface modification can cause changes in the nucleus morphology and indirectly changes in cell function. The long-term goal is to use this information during the development of new implantable devices. My question during this research work is how the astroglial cells, more specifically the cell nuclei react to the patterned SU-8 surface. In this work, I do not answer whether these surfaces are beneficial during long-term in vivo implantation or not.

2.2. Methods

2.2.1 Design of test surfaces

Three different micropatterns (micropillars, microstripes, micromeanders) designs were created with similar size parameters (see Fig.2.3). During preliminary experiments, we manufactured micropillars with 1, 2, or 5 µm diameter and microstripes with the same width as well. We tested spacing between the structures in the following sizes: 1/ 2/ 3/ 4/ 5/ 10/ 20 µm. The SEM monitoring showed that the 1 µm wide patterns are not stable enough and they are too small structures for the astrocytes to have any impact on adhesion. Similarly, the spaces smaller than 3 µm allow the cell to spread on the patterns without any major effect (Fig.2.4 C-D). On the other end of the parameter range, the 20 µm spaces are large enough to allow the cell to sit between the patterns and so the surface-cell interaction is the same as in the case of a flat surface (Fig.2.4 A-B). In the final parameter set, the micropillars are columnar structures 5.7 µm high, 2 or 5 µm in diameter with an inter-pillar distance of 3/5/10 µm. Microstripes are stripes 2 or 5 µm wide, spaced at 3/5/10 µm.

DOI:10.15774/PPKE.ITK.2023.003

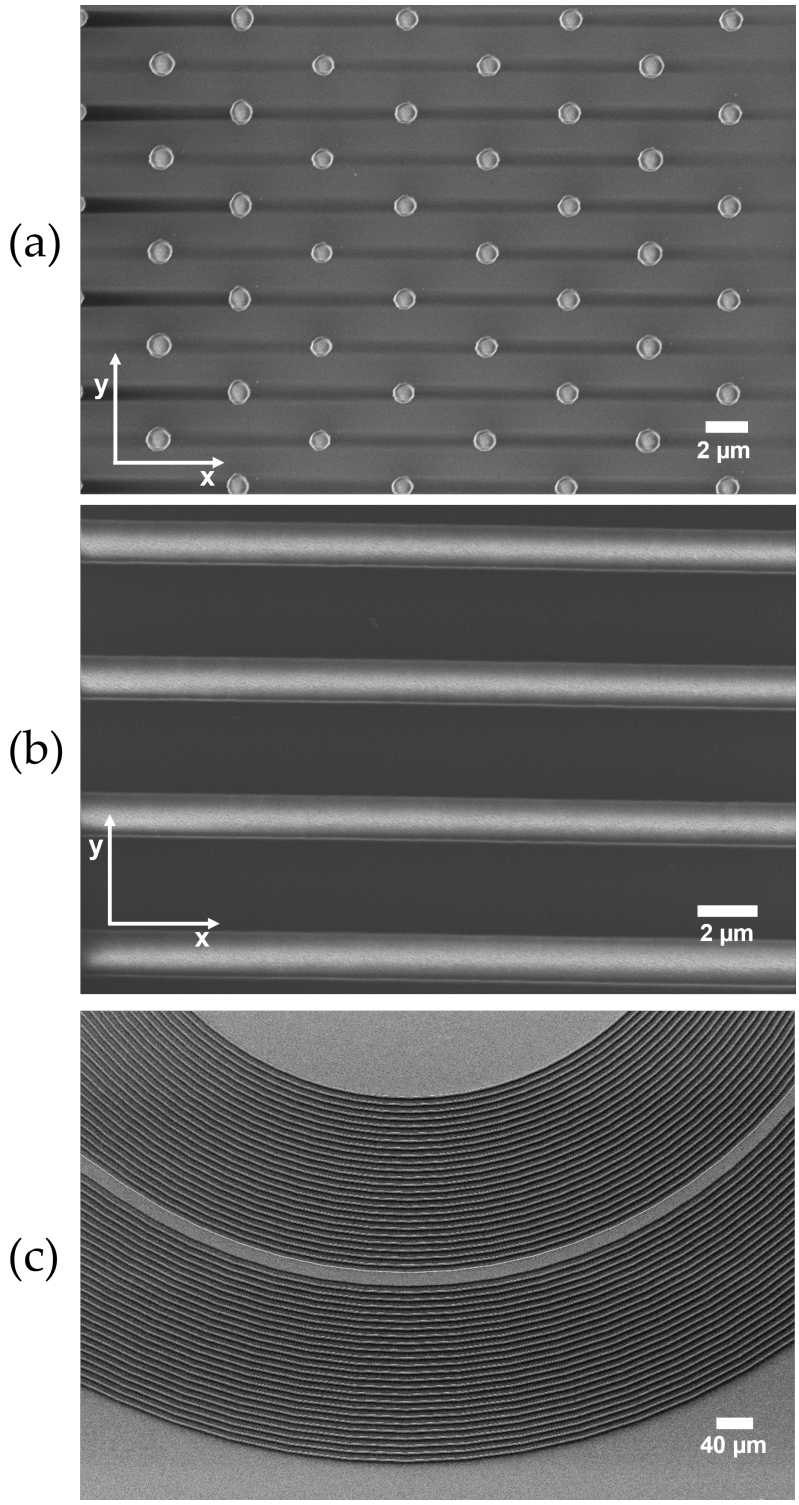

Figure 2.3: Scanning electron microscope (SEM) images of SU-8 micropatterns. (a): micropillars; (b): microstripes; (c): micromeander. Y and x represent the orientation axes.

DOI:10.15774/PPKE.ITK.2023.003

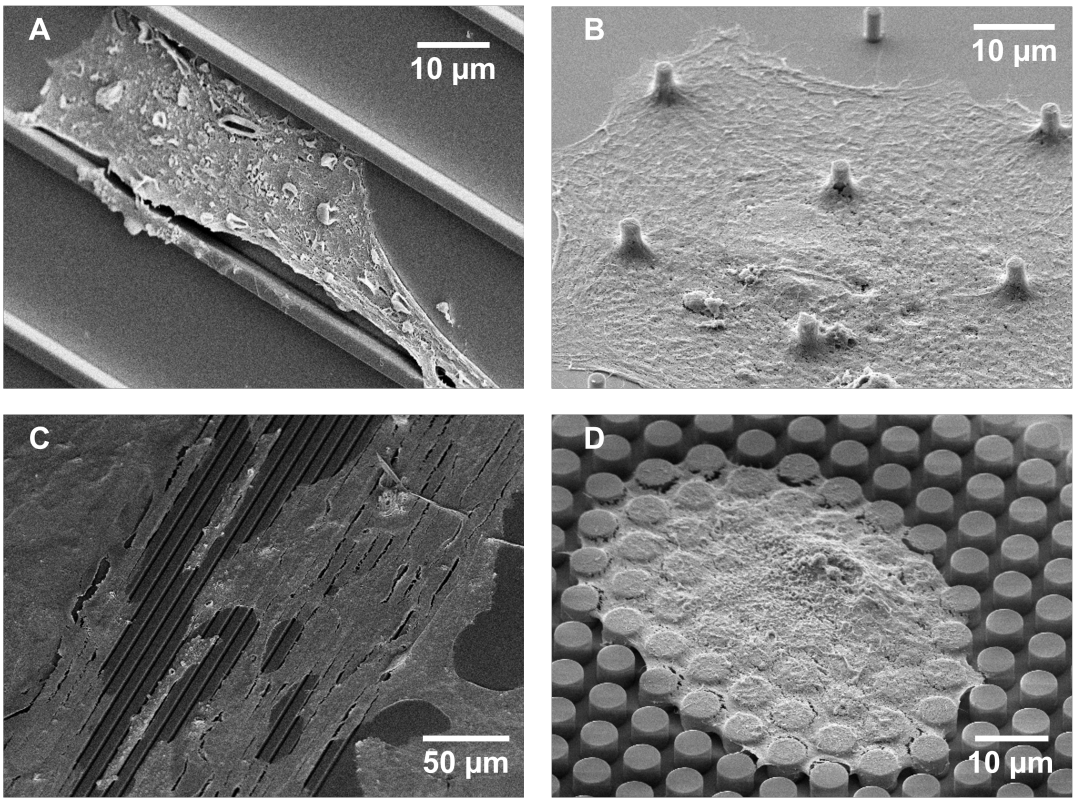

Figure 2.4: SEM images of SU-8 micropatterns with unselected spacing sizes and astrocytes. A: 2 µm wide microstripes with 20 µm spacing; B: 2 µm micropillars in diameter with 20 µm spacing. 20 µm means too much space to allow the astrocytes to spread out. C: 5 µm wide microstripes with 2 µm spacing; D: 5 µm diameter micropillars with 2 µm spacing. The 2 µm spacing means no difference during attachment since the cells can bridge so little space.

A third pattern, called micromeander, consists of parallel curved stripes where the width is 2 or 5 µm and the spacing of the trench is 5 µm. A representative SEM image of the whole structure is shown in Fig.2.5. Creating the micromeander pattern aimed to investigate the alignment of the cell nuclei to curvilinear structures.

DOI:10.15774/PPKE.ITK.2023.003

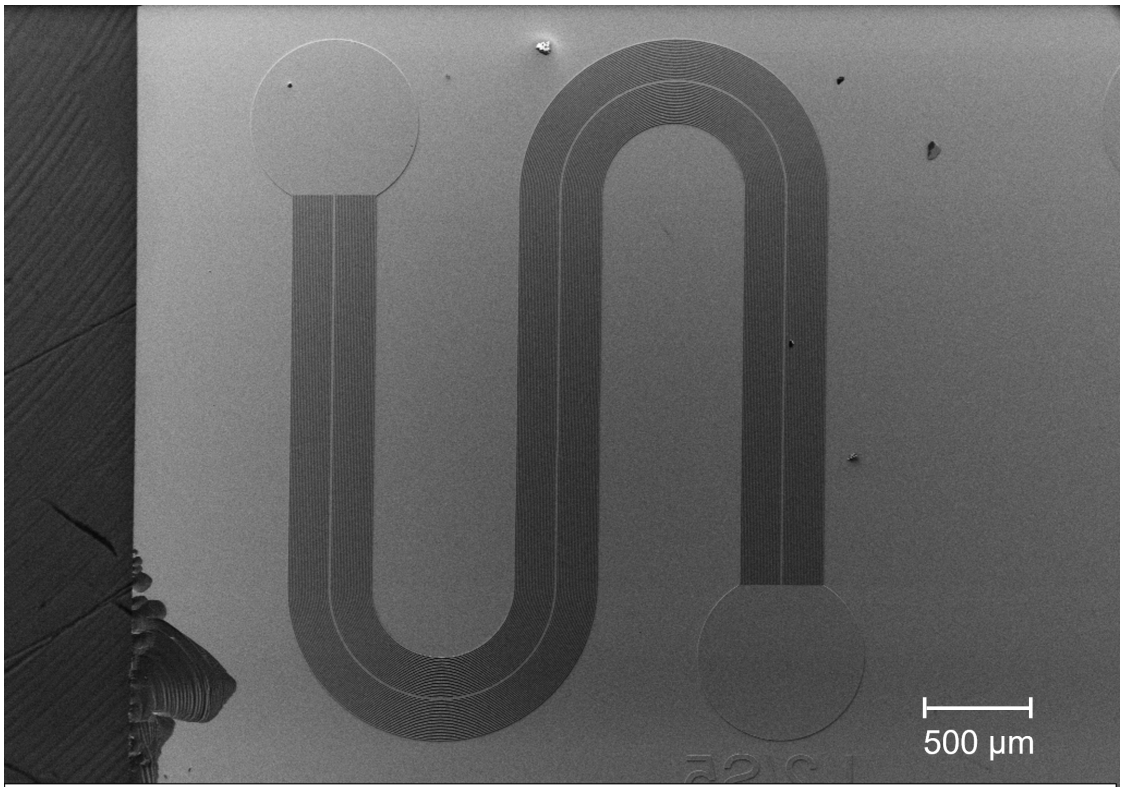

Figure 2.5: Representative SEM image about a whole micromeander structure. The line width is 2 µm and the spacing is 5 µm

These three pattern types are organized on chips of 7.1 by 7.1 mm, which also contain smooth, unpatterned areas of SiO_2 as control surfaces. Each chip contains one pattern type with all possible parameter combinations. The used pattern height (∼5.7 µm) is sufficiently large to have an impact on the cell nuclei. Based on the article of Pan Z. et al., a structure height over a critical height (5 µm) is beneficial to achieve self-deformation of cell nuclei [19]. The notations used in the following as 2/5 or 5/10 specify the line width (in case of stripes) or diameter (in case of pillars) of the structure as the first number while the spacing is indicated as the second number. Representative tiled view images are shown in Fig.2.6.

DOI:10.15774/PPKE.ITK.2023.003

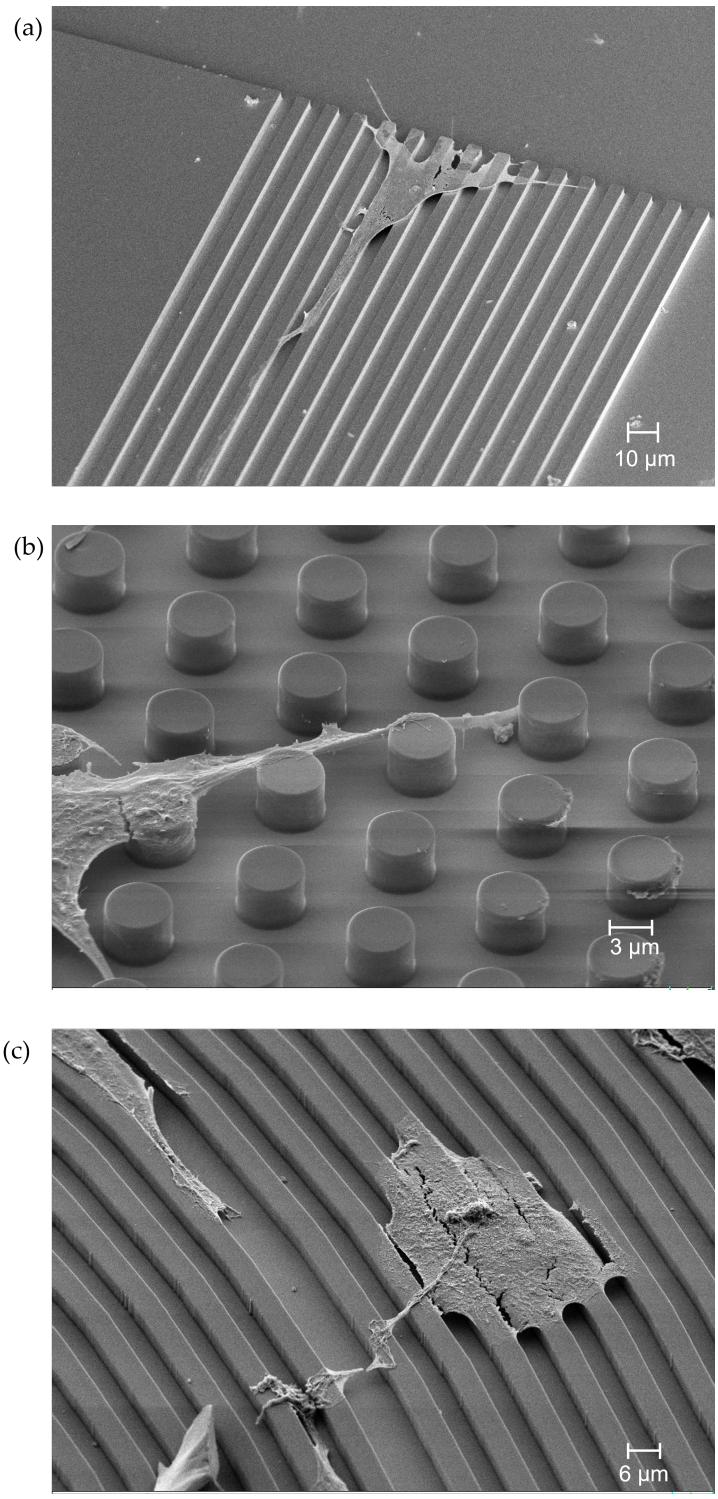

Figure 2.6: Representative SEM tiled view (45°) on microstructures with cells. A) 5/5 microstripes, B) 5/5 micropillars, C) 5/5 micromeander

DOI:10.15774/PPKE.ITK.2023.003

2.2.2 Material and fabrication

Micropatterned surfaces were created on a 4" 380 µm thick (100) silicon wafer using SU-8 2005, a high contrast, epoxy-based negative photoresist (Kayaku Advanced Materials, USA) at the Microsystems Laboratory of the Centre for Energy Research, Institute of Technical Physics and Materials Science.

The silicon substrate was cleaned with nitric acid, followed by HF dip and a dehydration step for an hour at 300 C° to promote the adhesion of SU-8 on the wafer. SU-8 2005 was spin-coated at 2500 RPM for 30 s to form 5-6 µm thick layers. After a soft bake at 95 C° for 2 minutes, the material was relaxed for 20 minutes before photolithography. Patterns were transferred in an MA6 Mask aligner (Süss Microtec SE, Germany) using chrome photomasks and 100 mJ/cm^2 exposure dose. Post-exposure bake was performed at 95 C° for 10 minutes and was followed by another relaxation step. After developing the pattern, a hard bake was completed at 150 C° for 30 minutes in a convection oven. The used temperatures and time parameters are consistent with the published datasheet of SU-8 2005 [27].

2.2.3 Cell culture

Primary astrocytes were prepared from 3-day-old mouse CD1 pups according to the method described in [28]. Cultures were maintained in HDMEM (Merck KGaA, Germany) with 10% FCS (Gibco), 2 mM glutamine (Merck KGaA, Germany), 40 µg/ml gentamicin (Hungaropharma Ltd, Hungary), and 2.5 µg/ml amphotericin B (Merck KGaA, Germany). Cells were passaged twice using 0.05% trypsin - 0.02% EDTA (Merck KGaA, Germany) before being seeded onto the test surfaces. Test surfaces were sterilized at 180°C for 4 hours and placed in 24-well culture plates under aseptic conditions. No additional surface treatment was applied. Astrocytes were seeded at starting densities of 40.000 cells/well in 500 µl of culture medium, completely covering the test surfaces. Cultures were kept at 37°C in a 5% CO_2 atmosphere and fixed with 4% PFA (20', RT) after 24 and 48 hours. The cell culturing and seeding to the surface was made at the Department of Physiology and Neurobiology, Faculty of Science, Eötvös Lóránd University (ELTE TTK) by Hanna Liliom and Katalin Schlett.

2.2.4 Imaging cell nuclei

Fixed cells were permeabilized using 0.1% Triton-x-100 in PBS for 5' at RT, followed by blocking with 2% bovine serum albumin in PBS. Nuclei of the cultured cells were stained

DOI:10.15774/PPKE.ITK.2023.003

with DAPI (4',6-diamidino-2-phenylindole) and images were taken at 24 and 48 hours after seeding using a fluorescence microscope (Zeiss Axio Observer.Z1) at ELTE TTK by Hanna Liliom and Katalin Schlett.

The microfabricated chip surfaces were analyzed with scanning electron microscopy (SEM) using a Zeiss LEO 1540 XB microscope at the Microsystems Laboratory of the Centre for Energy Research, Institute of Technical Physics and Materials Science by Anita Pongrácz. Samples were rinsed with 0.1 M cacodylate buffer (pH 7.4) and fixed with 2.5% glutaraldehyde and 5% sucrose in 0.1 M cacodylate buffer for 48 hours. Rinsing with 0.1 M cacodylate buffer was repeated three times, followed by 20-20 minutes of rinses with 50 %, 60 %, 75%, 90 %, and 100% ethanol. Samples were then immersed in amyl-acetate, which was left to evaporate in ambient air. Finally, samples were coated with a thin layer of gold by vacuum evaporation or cathodic sputtering. The sample pictures are shown in Fig.2.7.

DOI:10.15774/PPKE.ITK.2023.003

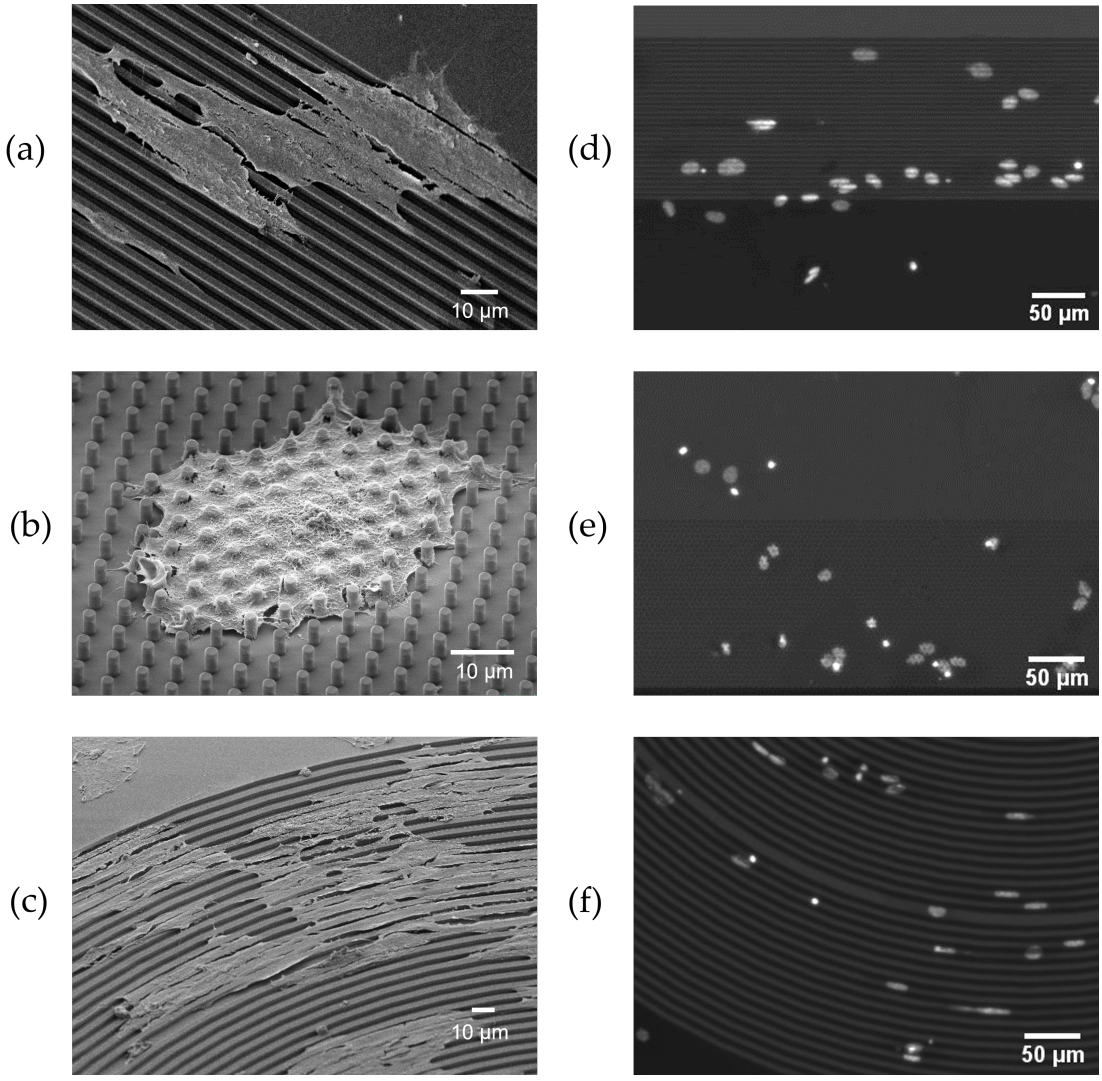

Figure 2.7: Representative scanning electron microscope images of astrocytes (a-c) and fluorescence images of astrocyte nuclei (d-f) on different micropatterns. 2 µm wide microstripes with 3 µm spacing (2/3) (a), (d); 2 µm in diameter micropillars with 3 µm spacing (2/3) (b), (e); micromeanders with 5 µm wide stripes with 5 µm spacing (5/5) (c), (f).

DOI:10.15774/PPKE.ITK.2023.003

2.2.5 Image processing, data analysis

The fluorescence images were analyzed by a custom-made, Matlab-based code with a graphical user interface (GUI). The core of my self-developed program was introduced in the supplementary material in an earlier publication [8]. The analysis began with the manual selection of the region of interest (ROI). For the statistical data analysis, the selection of a control ROI over the smooth, SiO_2 surface was required. Each pattern combination had a specific control ROI. The specific control ROI was selected between two patterned areas with the same pattern size. This manual selection was based on the visual borders of the topography, represented in Fig. 2.8. One chip contained two parts with the same pattern type, pattern width, and spacing. These areas had visible borders which helped to define the border of the ROIs (Fig. 2.8 ROI 1 and ROI 2). Between these ROIs was the control area with a lighter shade on the fluorescent image. This selection protocol helped to create similar size patterned ROIs and control ROIs. After the manual region selection, the image was processed, starting with segmentation. The detailed segmentation steps are shown in Fig.2.9.

The segmentation started with an adaptive thresholding step that separated the background from the foreground and gave a binary matrix as output. After the binarization, some non-cellular objects remained in the mask, originating mostly from the pattern or the borders between different surfaces. These elements formed the "bad mask", which, being bigger than a cell nucleus, could be removed from the binary image based on the area and skeleton area. The next steps refined the segmentation more precisely. Morphological opening and small object removal removed cell debris and other contamination from the mask. The last step of the segmentation was the Watershed algorithm, which separates objects in close contact.

Orientation and eccentricity are the two main parameters used to evaluate the outline of the nuclei. The calculation of these parameters is based on the measurement of the Matlab built-in "regionprops" function. The orientation is the angle between the nucleus's main axis and the pattern direction, as it is used in a previous study [29]. The lines of the microstripes unambiguously define the direction, the x-axis (Fig. 2.3. panel (b)). In the case of micropillars, the horizontal line (x-axis) was defined as the reference line of the orientation (Fig. 2.3. panel (a)). The curved micromeander lines require a circle ROI selection that gives the data for the orientation calculation. The specific ROI selection is illustrated in Fig. 2.10. Based on the center points and the radii of the circles, the program calculates the angle of the tangent line in the center point of the detected object.

DOI:10.15774/PPKE.ITK.2023.003

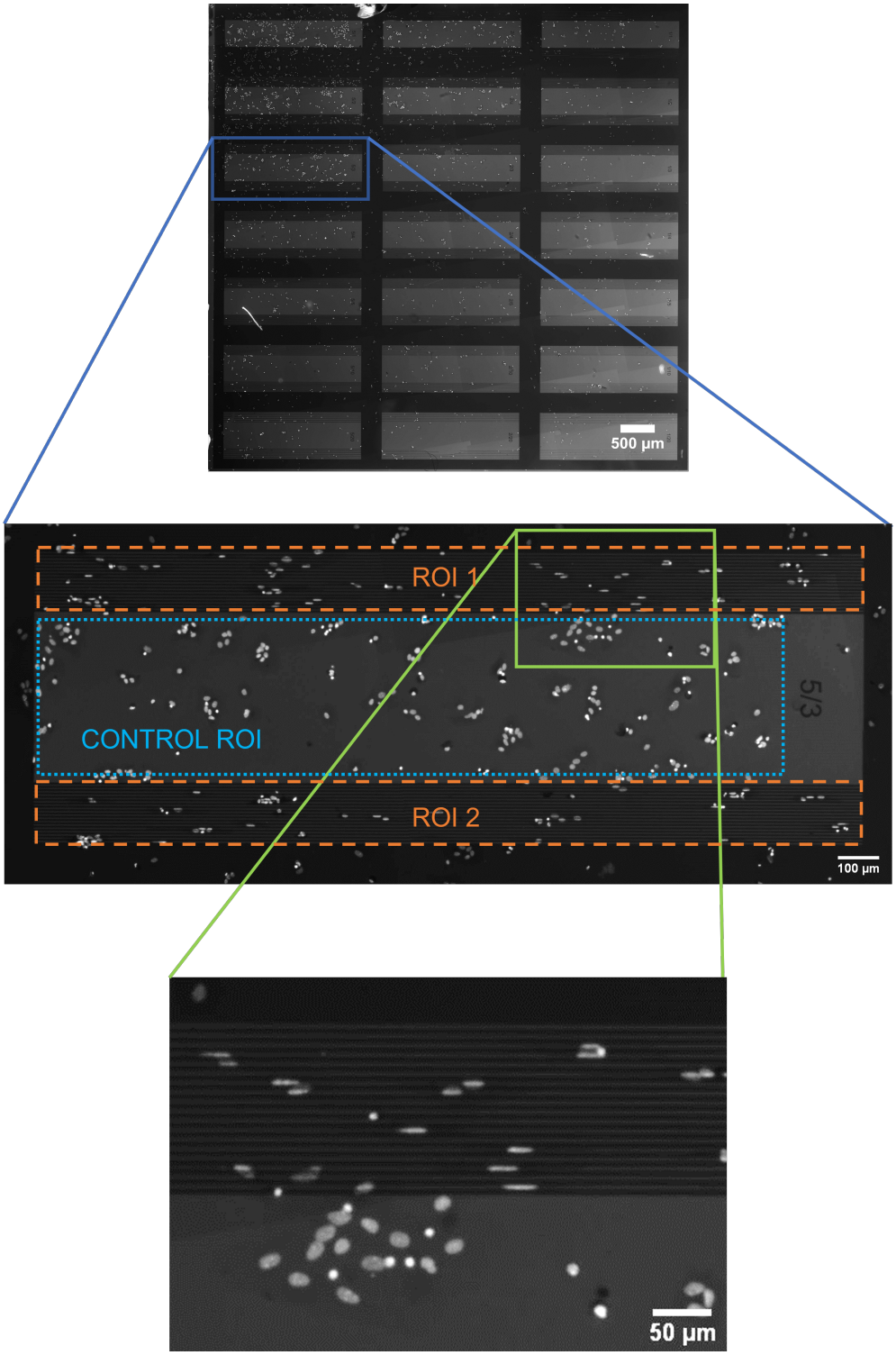

Figure 2.8: ROI selection on fluorescence image and a magnified portion of the chip. One topography feature combination (in this case 5 µm wide stripes with 3 µm spacing; 5/3) has two ROIs and one control ROI. With this method, the control ROI area and the combined patterned ROI area (ROI 1 + ROI 2) are the same. The bottom image represents a part of the microstripe sample.

DOI:10.15774/PPKE.ITK.2023.003

Figure 2.9: Workflow of the segmentation steps. The "bad mask" represents large elements remaining from the background such as the pattern lines or the border lines between different surfaces.

The calculated orientation is the difference between the nucleus's main axis angle and the previously calculated tangent line angle. One control data was selected for micromeanders on one chip. So for one fixation time, there is only one control data.

The eccentricity is derived from the major axis length (Major AL) and minor axis length (Minor AL) of the ellipse that has the same normalized second central moments as the nucleus (delimiting ellipse) [30]. Fig. 2.11. is an explanatory figure about these parameters on a sample image. The calculation method is:

$$Eccentricity = \frac{2\sqrt{\left(\frac{MajorAL}{2}\right)^2 - \left(\frac{MinorAL}{2}\right)^2}}{MajorAL} \tag{2.1}$$

This way, zero eccentricity indicates a perfect circle, and an eccentricity of 1 indicates a line. Based on this definition the elements with an eccentricity greater than 0.5 were determined as elongated cells.

Next to the orientation and eccentricity, two other major parameters were examined. The cell number was derived from the detected nucleus number and the nucleus area was calculated with the previously mentioned "regionprops" function. The manual selection of the ROIs can add a possible difference to the sizes of the ROIs. To eliminate this difference from the data comparison, the cell numbers ($N_{pattern}$ and $N_{control}$) were normalized to the corresponding ROI size ($A_{pattern}$ and $A_{control}$). The final comparison between the patterned and control surface was performed from this cell number normalized to the region:

$$\text{Normalized cell number} = \frac{\frac{N_{pattern}}{A_{pattern}}}{\frac{N_{control}}{A_{control}}} \tag{2.2}$$

.

The comparison of different featured surface effects was done along these four parameters. The cell numbers and area data were normalized to the data from the corresponding control ROI. In the case of orientation, the data were visualized with a cumulative histogram. The elongation data is presented as the rate of the above-defined elongated nuclei (with an eccentricity value greater than 0.5).

DOI:10.15774/PPKE.ITK.2023.003

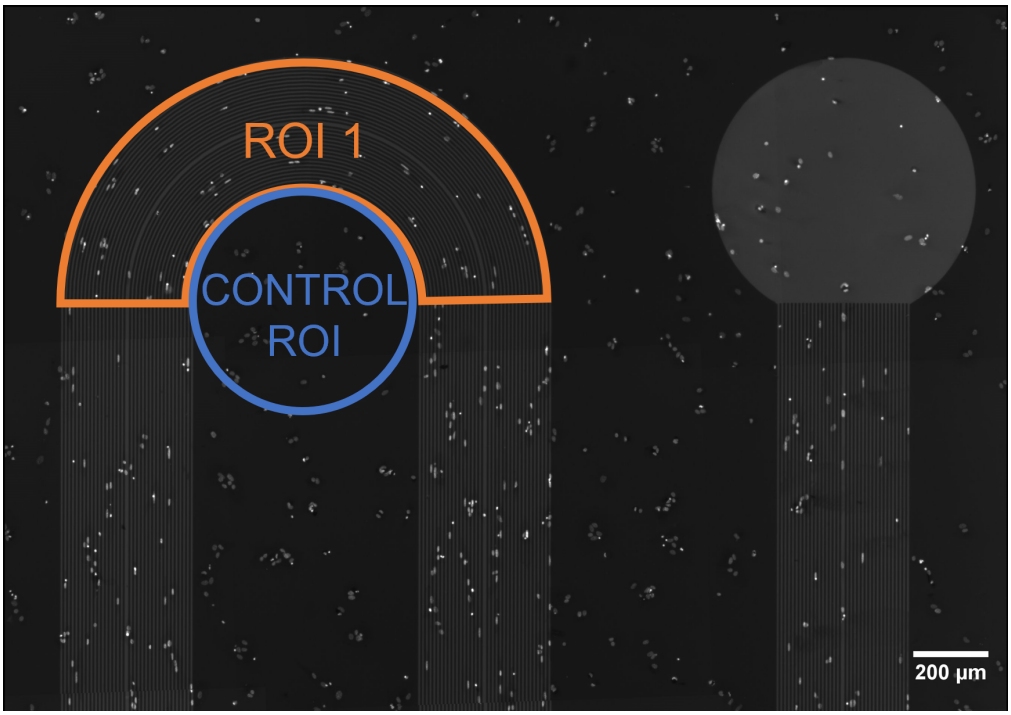

Figure 2.10: ROI selection on micromeander patterned samples. ROI 1 is a circle with the patterned surface. The two separation lines are calculated from the center coordinations automatically. The control ROI's center point is the base of the orientation calculation.

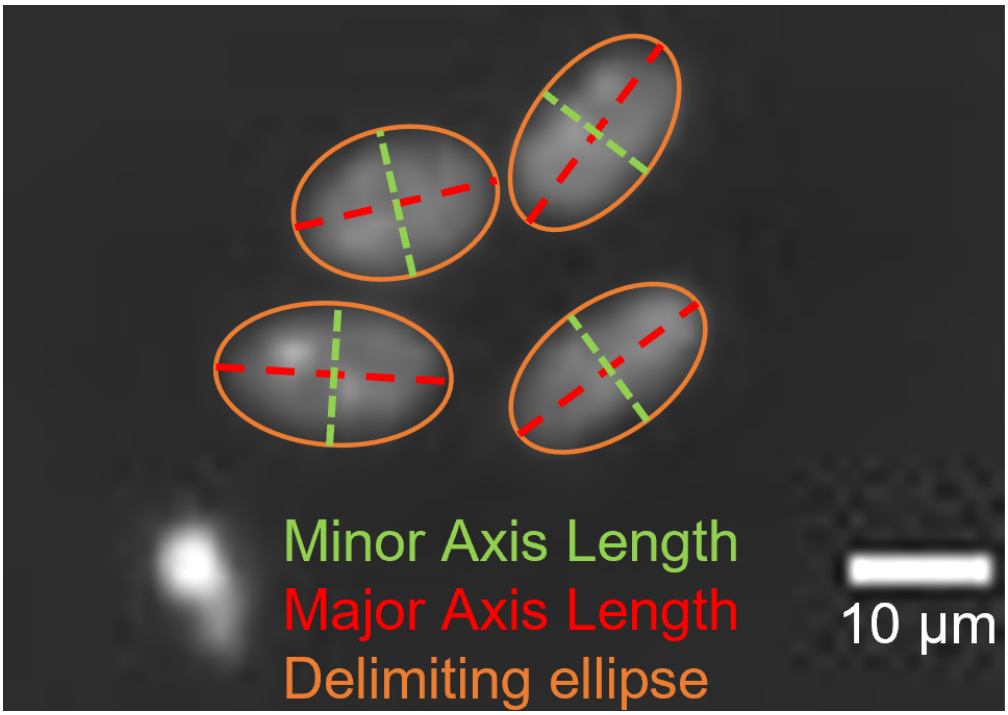

Figure 2.11: Representation of the Minor Axis Lenght (green), Major Axis Lenght (red), and the delimiting ellipse of the nucleus (orange) on fluorescent microscope image.

DOI:10.15774/PPKE.ITK.2023.003

2.2.6 Performance of the detection program

Since the image analysis is based on a custom evaluation code, error measurement was performed to prove the reliability of the analysis. The detection was examined at 10 randomly selected ROI. The performance is calculated from the number of correctly detected objects (true positive; TP) – including the separated overlapped nuclei – the number of erroneously detected objects (false positive; FP) – mostly not deleted larger fragments, or background residual pieces – and the number of non-detected, false negative (FN) objects. The 10 test ROIs were analyzed manually to quantify the error of the program. The 10 samples had overall 438 detected cell nuclei and the error measurement gave a 0.8541 precision and a 0.9305 recall based on the following, commonly used equations:

$$Precision = \frac{TP}{TP + FP} \tag{2.3}$$

$$Recall = \frac{TP}{TP + FN} \tag{2.4}$$

2.3. Results and discussion

In this study, I investigated the interaction between micropatterned SU-8 surface and astrocytes through three parameters. These aspects are the adhesion - analyzed through cell number and nucleus size, - orientation, and elongation. These parameters are presented in the following three sections.

2.3.1 Adhesion and spreading of astrocyte nuclei on SU-8 micropatterns

The diameter of the primary mouse astrocyte nucleus is within a 10-µm range. Former studies investigated the effects of smaller, 3 µm wide micropillars [19], and 30 µm parallel lines [31]. In the present study, we created patterns with 3, 5, and 10 µm spacing which are closer to the nucleus size range. Therefore, we expected to see actual effects on the chosen astrocyte nuclei. To investigate how astrocytes can attach to the surface, the cell number was counted and normalized to the selected region area. The same calculation was measured on the smooth SiO_2 control surface. The calculated cell counts normalized to the ROI area were then compared with the control normalized cell count, belonging to the specific parameter size pattern. The results are represented in Fig.2.12, the cell numbers are the same as the N numbers in Table 2.1. The bars represent the cell number

DOI:10.15774/PPKE.ITK.2023.003

rate between the control (SiO_2) surface and the patterned surface (SU-8). With this method, we compensate for the different cell densities between samples. It is visible on the diagram, that more cells were detected on all surfaces with both fixating times compared to the control surface, except for the 5 µm wide microstripes with 3 µm spacing surface after 24 hours. The cell numbers compared to the control show that after 48 hours more cells are detected over any patterned SU-8 surface than over the flat SiO_2 surface. This different cell number matches with a previous study [16], where unpatterned SU-8 showed a significantly higher volume of initial cell adhesion than plain silicon. Another study using other polymer surfaces concluded that astrocytes from human teratocarcinoma cell line (hNT) had a higher nuclear percentage coverage on Parylene-C than on SiO_2 [32].

Since the area of the nuclei reflects the spreading of cells on a given surface and nucleus detection is more precise and can be easily automated, the average nucleus area was measured and normalized to the previously presented control surface. The results are shown in Fig.2.13. The average nucleus area in the presence of microstripes and micropillars is smaller than on a smooth SiO_2 surface. The nucleus area is an important characteristic of cell viability. In case of an apoptotic cell, a shrunken cell nucleus can be detected. Although no separate viability test was performed, based on a previous study [16] the average nucleus sizes imply living astrocytes. In this study, they found the average area of live cells was 80 μm^2, with C6 rat astrocytoma cell line on the SU-8 surface. If we examine the cell numbers together with the average nucleus size, we can conclude that the cells adhered to the patterned surface to a greater extent than to the flat control surface, but the patterns caused a smaller nucleus size.

The cell numbers and average nuclei area were also examined in the presence of the micromeander. The results are represented in Fig. 2.14. The detected cell nucleus number is presented in Table 2.1. When comparing the cell nuclei on micromeander and microstripes, we found no significant difference in the case of 2 µm wide micropatterns, while in the case of 5 µm wide patterns with 5 µm spacing, there was a significant difference. (Two-sample Student t-test on non-normalized data: 24 hours - $p \ll 0.05$; 48 hours - $p=0.02$, average, and standard deviation values are shown in Table 2.1).

DOI:10.15774/PPKE.ITK.2023.003

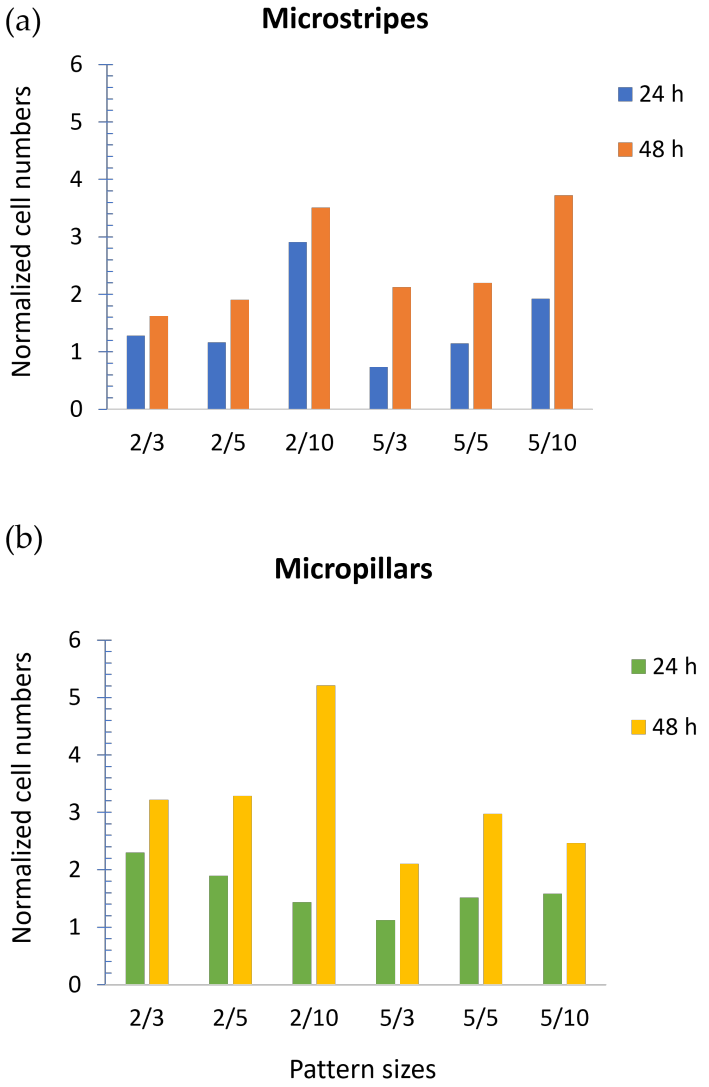

Figure 2.12: Cell numbers normalized to the control surface. The bars represent the ratio of the cell number normalized to the ROI area between the patterned surface and the corresponding control surface. One panel shows one pattern type (microstripes or micropillars) with all topography sizes. Along the x-axis, columns are labeled in the following way: the first number indicates the width of microstripes or micropillars while spacing is represented by the second number (all in µm). 24h or 48h fixation times are represented in different colors. (a): normalized cell number by microstripes with different stripe widths and spacing; (b): normalized cell number by micropillars with different diameters and spacings. The cell number normalized to the ROI area eliminates possible region size differences resulting from the manual selection. Corresponding N numbers are represented in Table 2.1. The bars show that on patterned SU-8 surfaces more astroglial cells were detected than on plain SiO_2, except of 5 µm microstripes with 3 µm spacing after 24 hours fixation time.

DOI:10.15774/PPKE.ITK.2023.003

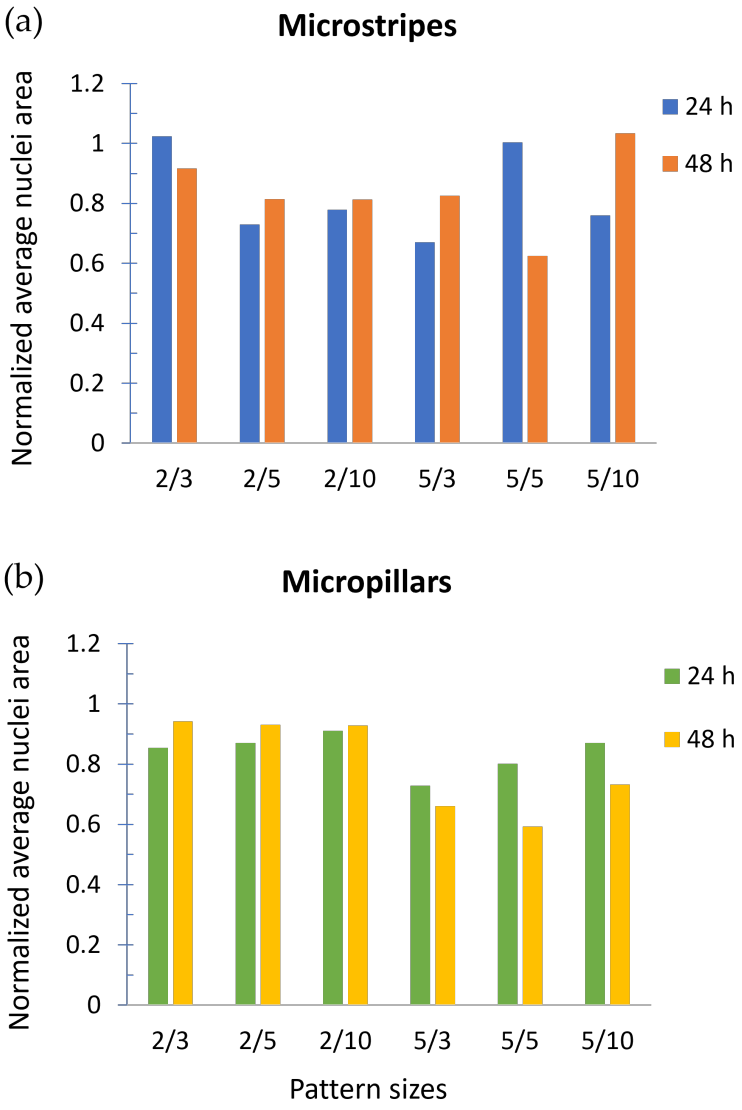

Figure 2.13: Average nuclei area data normalized to the control surface. The bars represent the ratio of the average nuclei area between the patterned surface and the corresponding control surface. One panel shows one pattern type (microstripes or micropillars) with all topography sizes. Along the x-axis, columns are labeled in the following way: the first number indicates the width of microstripes or micropillars while spacing is represented by the second number (all in µm). 24h or 48h fixation times are represented in different colors. (a): normalized average nucleus area by microstripes; (b): normalized average nucleus area by micropillars. The corresponding statistical data are represented in Table 2.1. Only in one case was the average nucleus area greater on a patterned surface than on the control surface: after 48 hours on 5 µm microstripes with 10 µm spacing. Any other pattern parameters caused a smaller astroglial cell nucleus compare to a plain SiO_2 surface.

DOI:10.15774/PPKE.ITK.2023.003

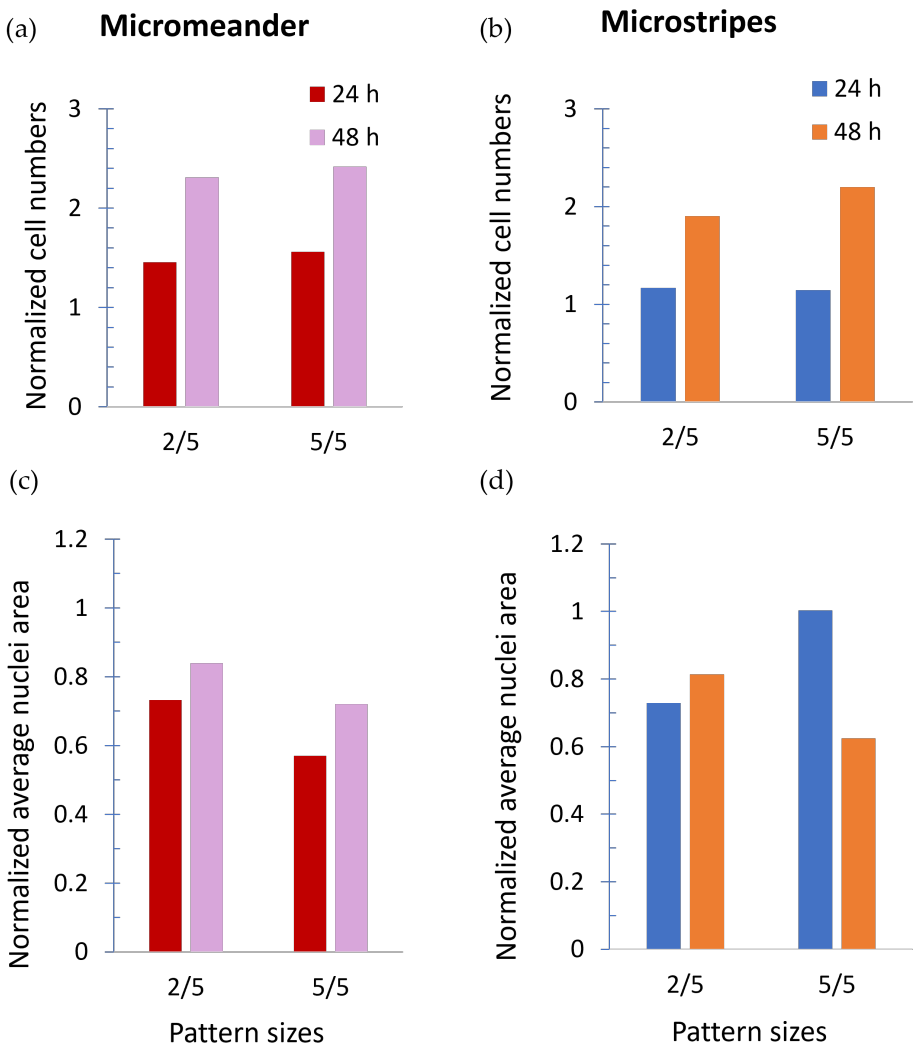

Figure 2.14: Cell numbers and average nuclei area data normalized to the control surface. The bars represent the ratio of the cell number and average nucleus area on the patterned surface and the corresponding control surface. One panel shows one pattern type (micromeander or microstripes) with the two, same topography sizes. Along the x-axis, columns are labeled in the following way: the first number indicates micromeander or microstripes width while spacing is represented by the second number (all in µm). 24h or 48h fixation times are represented in different colors. (a): normalized cell number by micromeander with different stripe width and spacing; (b): normalized cell number by microstripes with different diameter and spacing; (c): normalized average nucleus area by micromeander; (d): normalized average nucleus area microstripes. The normalization with the control areas allows the comparison between the different feature-sized areas.

DOI:10.15774/PPKE.ITK.2023.003

Microstripes

	24 hours			48 hours			24 hours			48 hours		
	2/3	2/5	2/10	2/3	2/5	2/10	5/3	5/5	5/10	5/3	5/5	5/10
avg	86.15	63.89	68.31	93.97	83.52	86.11	72.54	96.11	71.31	111.17	78.80	127.26
SD	46.61	25.16	34.52	54.05	39.52	50.90	38.59	81.76	52.94	53.35	40.79	149.55
N	64	30	70	90	53	78	115	58	72	82	55	107

Micropillars

	24 hours			48 hours			24 hours			48 hours		
	2/3	2/5	2/10	2/3	2/5	2/10	5/3	5/5	5/10	5/3	5/5	5/10
avg	85.10	85.92	89.61	83.70	81.18	79.02	75.41	79.18	86.73	64.37	56.75	70.06
SD	41.11	43.04	42.61	36.75	37.17	43.76	41.29	44.60	43.80	32.50	27.50	40.74
N	123	133	120	140	146	156	105	108	123	83	100	48

Microstripes control

	24 hours			48 hours			24 hours			48 hours		
	2/3	2/5	2/10	2/3	2/5	2/10	5/3	5/5	5/10	5/3	5/5	5/10
avg	88.87	77.16	86.32	108.33	104.50	95.30	88.77	133.41	86.48	122.92	107.60	209.78
SD	54.60	39.67	61.47	59.58	64.49	54.67	46.44	208.61	39.46	64.39	42.85	608.03
N	54	28	30	60	34	25	185	54	39	37	26	28

Micropillars control

	24 hours			48 hours			24 hours			48 hours		
	2/3	2/5	2/10	2/3	2/5	2/10	5/3	5/5	5/10	5/3	5/5	5/10
avg	95.79	98.99	96.43	93.28	81.34	102.88	84.20	102.61	101.08	99.69	78.23	114.23
SD	46.68	61.94	62.30	57.31	40.70	51.28	39.13	55.01	52.38	46.77	48.23	65.88
N	52	68	90	48	49	29	96	70	78	35	23	9

Micromeander

	24 hours			48 hours		
	2/5	5/5	control	2/5	5/5	control
avg	79.26	61.73	108.22	75.36	64.64	89.74
SD	60.63	50.13	45.39	50.97	39.51	45.03
N	124	130	85	158	166	69

Table 2.1: Statistics of the nucleus area data. The unit of measure of the average (avg) and the standard deviation (SD) is μm^2. The N numbers are the same in the case of cell number, orientation, and elongation data.

DOI:10.15774/PPKE.ITK.2023.003

2.3.2 Nuclei orientation

The orientation of the cells is one of the most important parameters in the case of research on engineered culturing surfaces. There are several studies on the cytoskeleton alignment [33, 34, 35], but the alignment of the cell nucleus is a rarely addressed question. Although it gives less information about the cell, the automation of nuclei detection is an easier task than automating the detection of the cytoskeleton, because of their more uniform shape. Fig. 2.15 - 2.19 show the cumulative histogram of the orientation in the different parameter spaces and after the two different fixation times. The x-axis shows the angle between the main axis of the detected object and the microstripes direction (Fig. 2.15-2.16) and the main axis and the x-axis (horizontal line) in the case of the micropillars (Fig. 2.17-2.18). In the case of micromeanders (Fig. 2.19) the orientation angle is measured between the nucleus's main axis and the tangential line of the curvature. The orientation diagrams are cumulative, that is, the values show the proportion of nuclei with orientation in the given or smaller angles.

Microstripes force more than 50% of the cells to accommodate the pattern at an angle less than 15° with respect to the pattern direction in the case of 2 µm wide microstripes with 5 µm and 10 µm spacing, and 5 µm stripe width with all spacing sizes after 24 hours. After 48 hours all topographical parameters oriented more than half of the nuclei. Based on a previous study [36], we considered these cells with less than 15° orientation angle as aligned cells. In the presence of micropillars, the angle distribution is even, so no favored topography would alter the direction of the nuclei growth. Patterns with micropillars have no major effect on astrocyte nuclei compared to a smooth control surface. Similar results were shown in [37], where osteosarcoma cells grow on 2–4 µm micropillars separated by 10–12 µm without any obvious effect on cell morphology. The different distribution of the measured orientation angles between the plain and the striped surface was earlier published with the presence of PDMS with a laminin cover [38, 39].

I found that both 2 µm and 5 µm wide microstripes align the cell nucleus already after 24 hours. The 2 µm wide microstripes with 10 µm spacing have the greatest effect on orientation after cell adhesion. This difference between the pattern effects ceases by the second day. Comparing the orientation between microstripes and micromeander with the same pattern dimensions revealed similar trends. The curvature of the micromeander has no main effects on the orientation of the cell nuclei. (Fig. 2.19).

DOI:10.15774/PPKE.ITK.2023.003

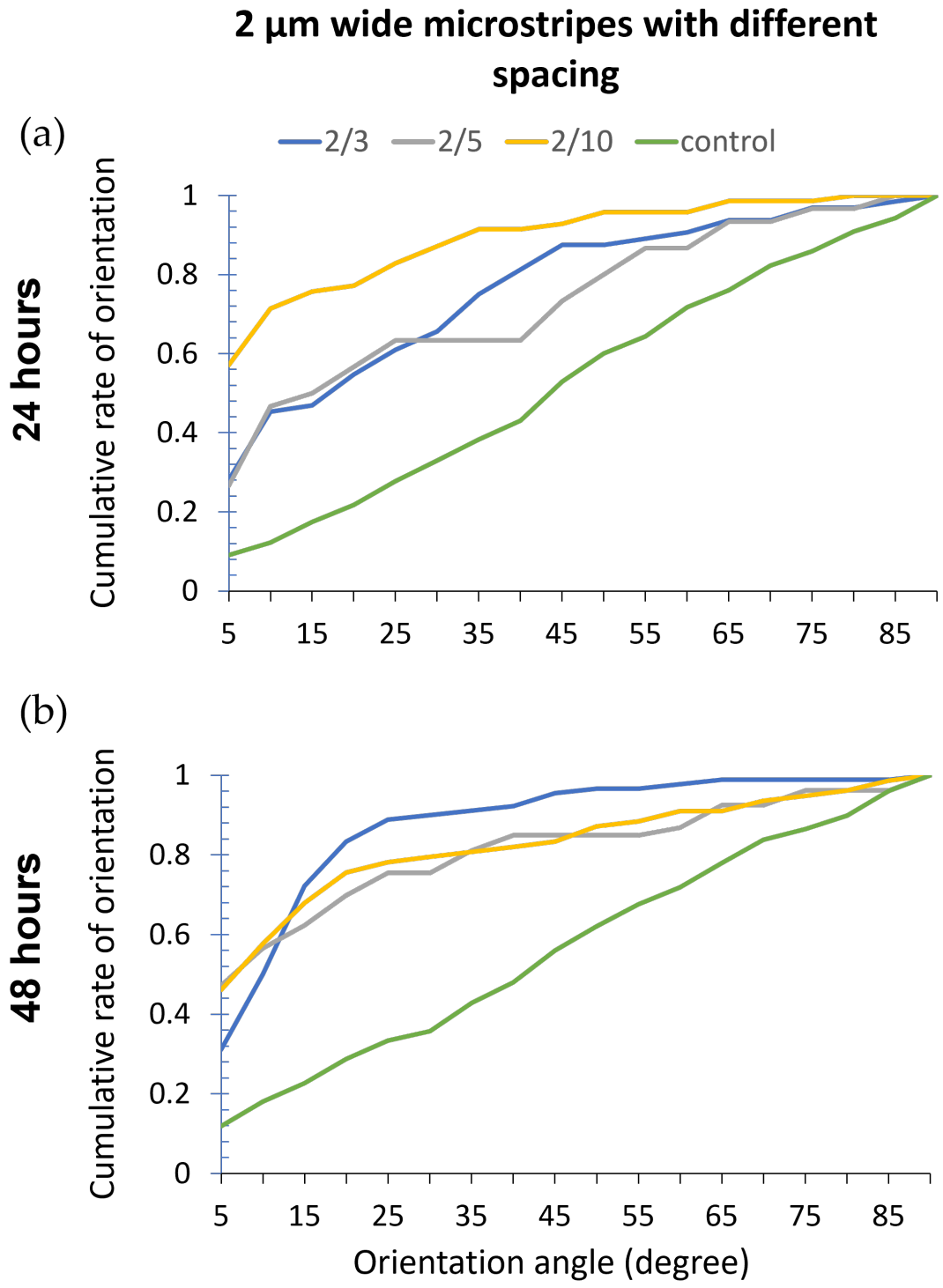

Figure 2.15: Orientation data on microstripes. The cumulative histogram of the angle between the nuclei main axis and the stripe direction in case of (a): 2 µm microstripes with different spacing and 24 hours fixation time; (b): 2 µm microstripes with different spacing and 48 hours fixation time.

DOI:10.15774/PPKE.ITK.2023.003

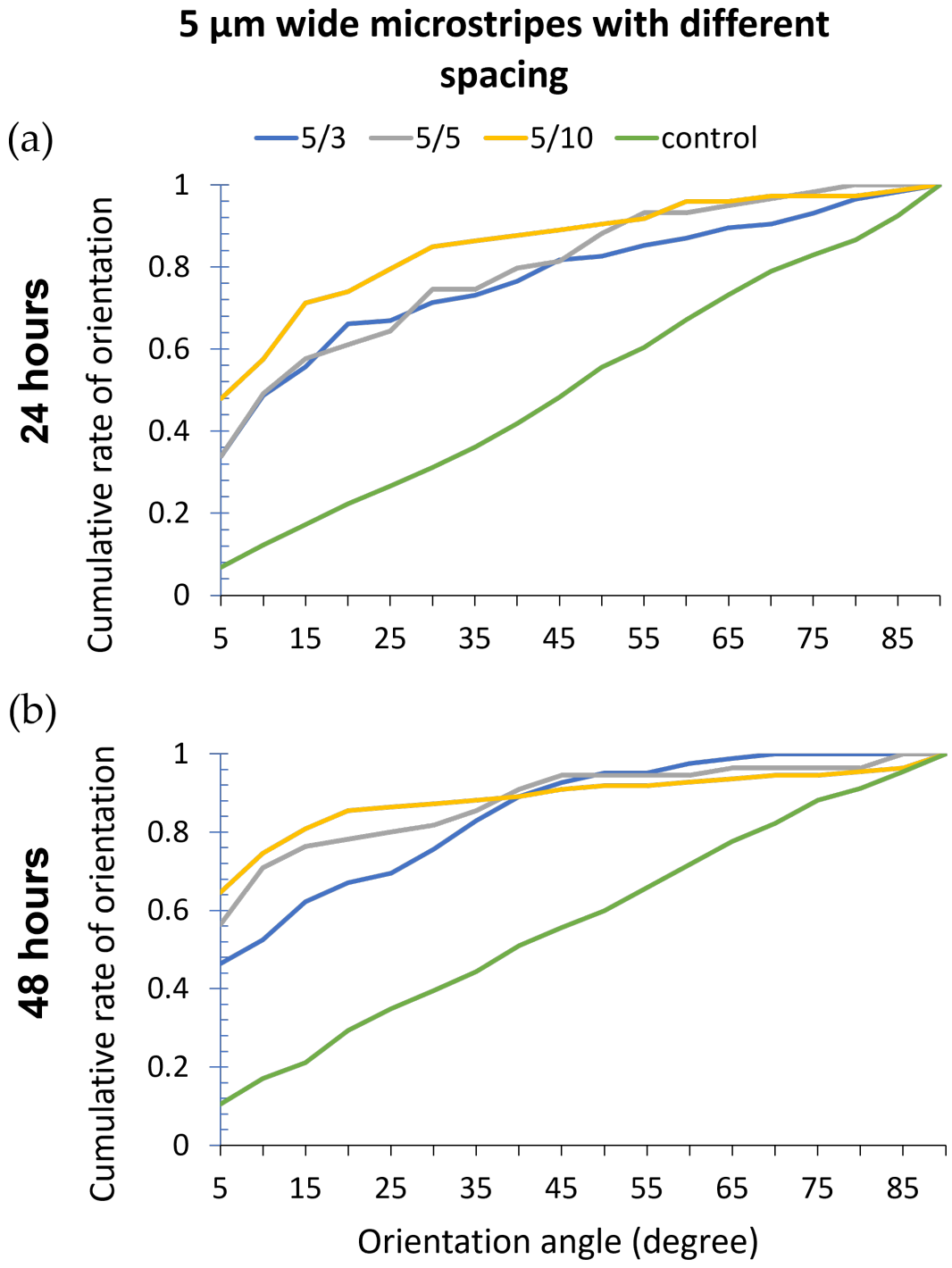

Figure 2.16: Orientation data on microstripes. The cumulative histogram of the angle between the nuclei main axis and the stripe direction in case of (a): 5 µm microstripes with different spacing and 24 hours fixation time; (b): 5 µm microstripes with different spacing and 48 hours fixation time.

DOI:10.15774/PPKE.ITK.2023.003

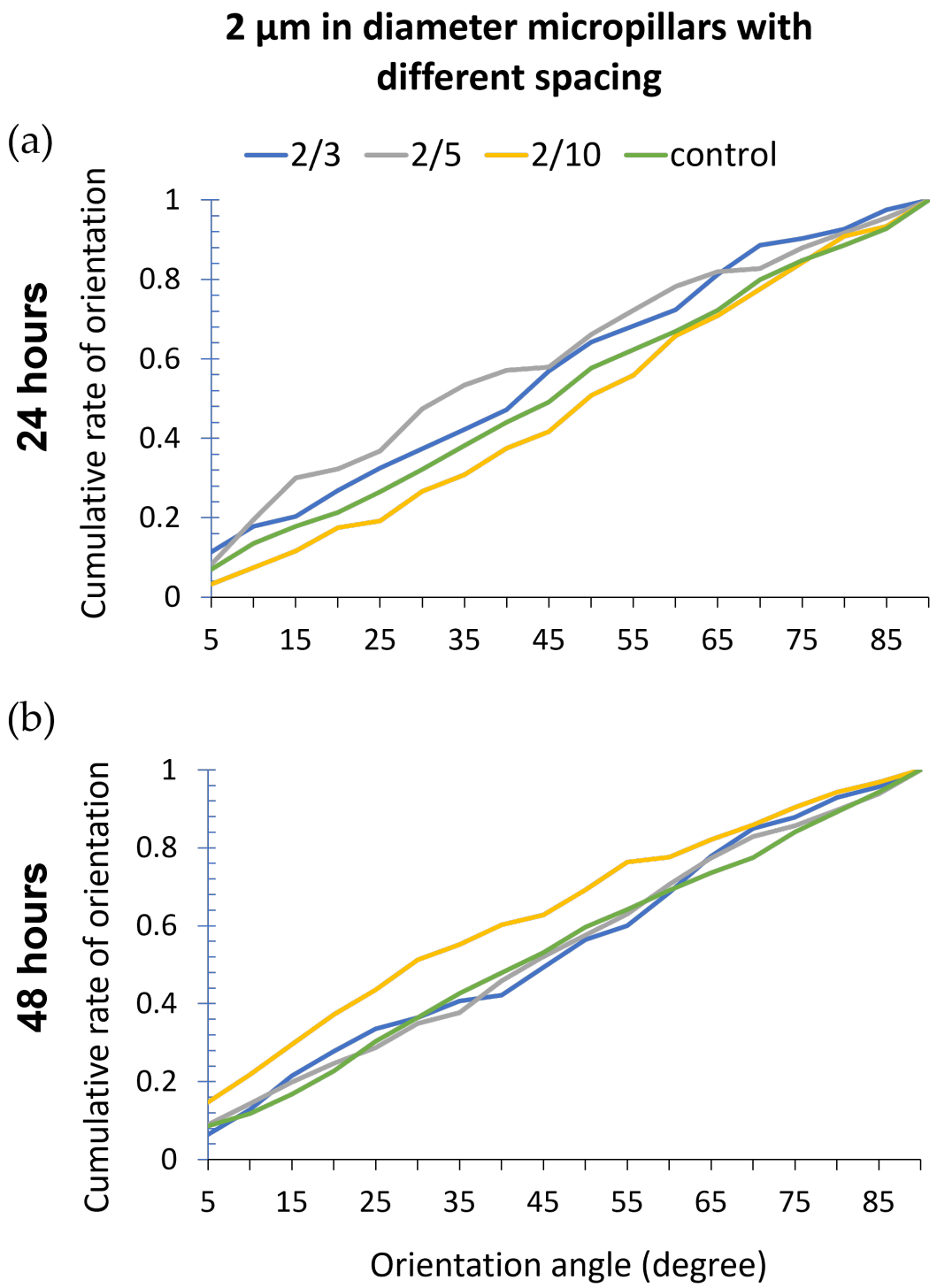

Figure 2.17: Orientation data on micropillar. The cumulative histogram of the angle between the nuclei main axis and the x-axis in case of (a): 2 µm in diameter micropillars with different spacing and 24 hours fixation time; (b): 2 µm in diameter micropillars with different spacing and 48 hours fixation time.

DOI:10.15774/PPKE.ITK.2023.003

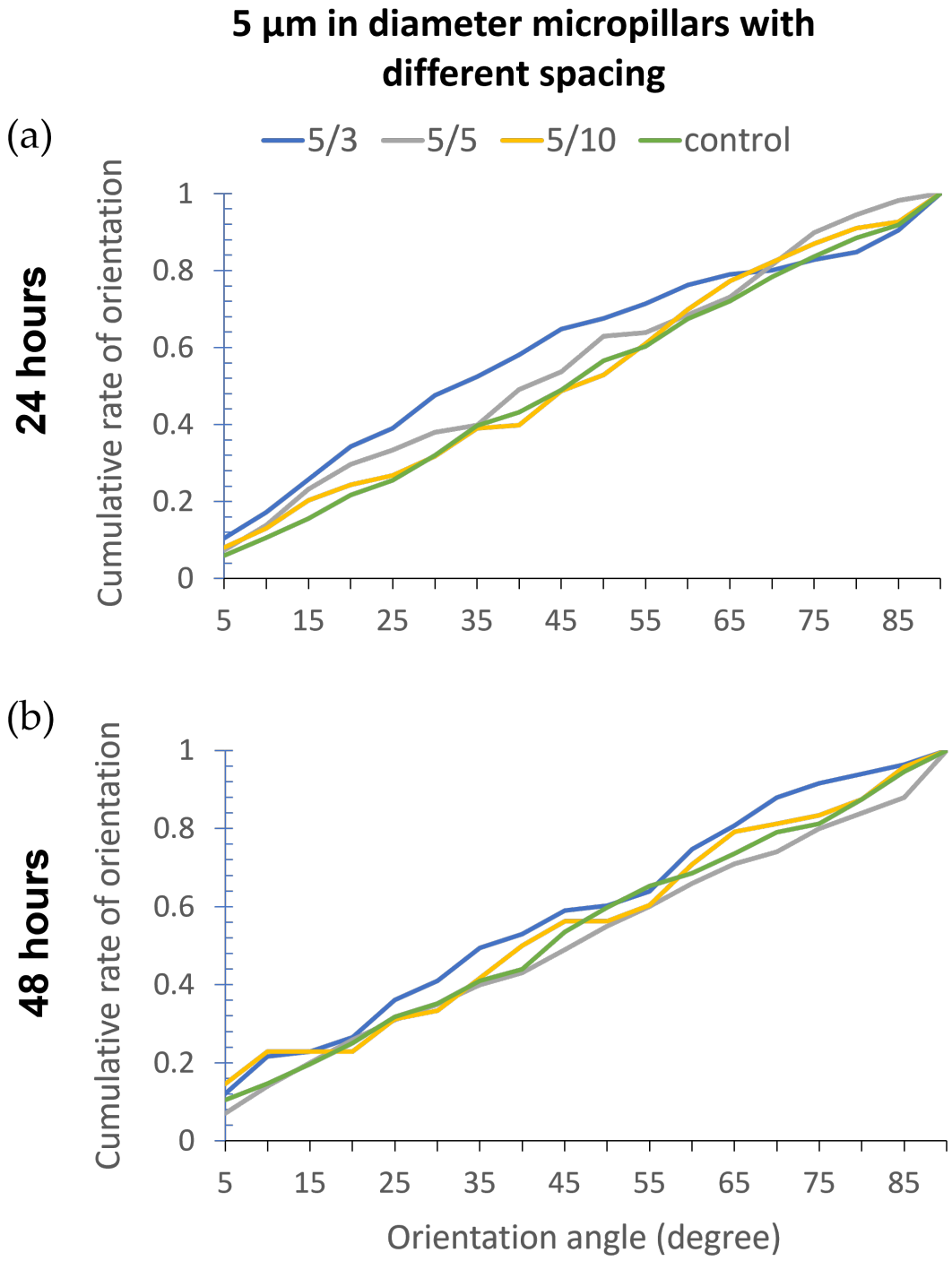

Figure 2.18: Orientation data on micropillar. The cumulative histogram of the angle between the nuclei main axis and the x-axis in case of (a): 5 µm in diameter micropillars with different spacing and 24 hours fixation time; (b): 5 µm in diameter micropillars with different spacing and 48 hours fixation time.

DOI:10.15774/PPKE.ITK.2023.003

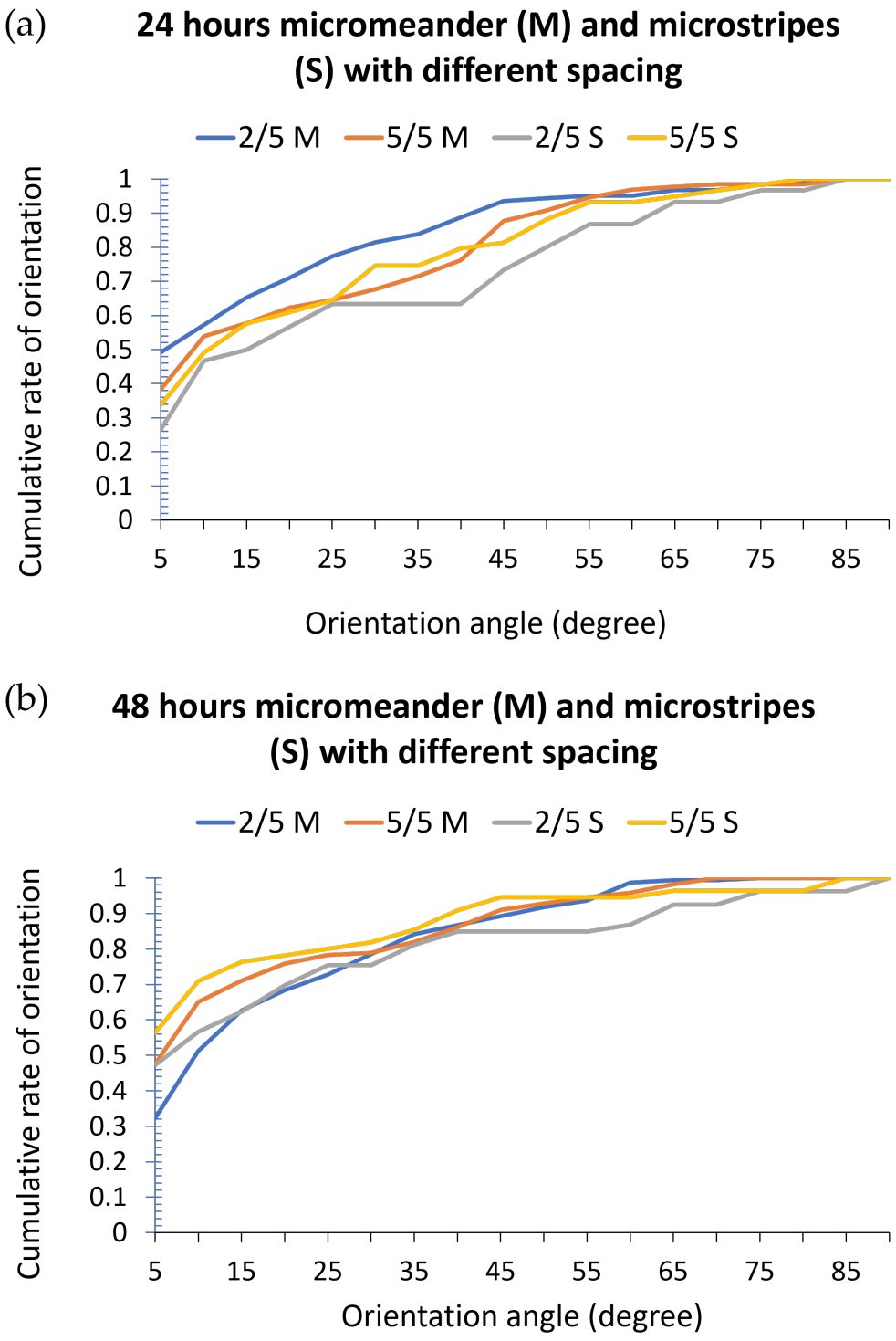

Figure 2.19: Orientation data on micromeander and microstripes. The cumulative histogram of the angle between the nuclei main axis and the stripe direction in case of (a): different pattern dimensions (2/5, 5/5) after 24 hours fixation time; (b): different pattern dimensions (2/5, 5/5) after 48 hours fixation time. The letters M and S in the legends indicate micromeander and microstripes.

DOI:10.15774/PPKE.ITK.2023.003

2.3.3 Nuclei elongation

The cell nucleus is especially sensitive to changes in its microenvironment. Table 2.2. shows the rate of elongated nuclei after 2 days. I defined the elongated elements as the nuclei that have at least 0.5 eccentricity value, defined in section 2.5. The represented rate originates from the cumulative density of the eccentricity values of the nuclei. The numbers in Table 2.2 show the rate of the nuclei that have greater than 0.5 eccentricity values. I compared the elongation rate between the 2 µm wide microstripes, 2 µm diameter micropillars, and 2 µm wide micromeander data with 5 µm spacing (2/5) and also the different pattern types with 5 µm pattern width (and diameter in case of micropillars) and 5 µm spacing (5/5). These two parameter combinations were created with all three pattern types.

	Microstructures						
Pattern size/ spacing		Microstripes		Micropillars		Micromeander	
		pattern	*control*	*pattern*	*control*	*pattern*	*control*
	2/5	0.94	0.80	0.86	0.82	0.92	0.84
	5/5	0.93	0.87	0.88	0.72	0.94	

Table 2.2: The ratio of elongated nuclei in the presence of different microstructures. We defined elongated nuclei as nuclei that have a greater than 0.5 eccentricity value.

To help understand the elongation, the distribution of eccentricity values is presented in Fig. 2.20. In the case of micropillars, the outliers show that there are more circular nuclei - almost perfect circles - in the presence of this topography than in the case of linear patterns. The figure also represents the significant differences, calculated with Mann-Whitney U-test, since the elongation data were not normally distributed. The statistical results are listed in Table 2.3.

As we expected, the micromeander stripes have a great elongation effect on the nuclei. The microstripes resulted in a high rate of elongated nuclei. The results show that the linear surfaces, the microstripes, and the micromeanders cause large-scale elongation on astrocytes while the micropillars have a smaller impact on the nuclei elongation. In the case of microstripes and micromeander, all patterned surfaces caused a significant difference compared to the control surface. Although the 2 µm diameter micropillars showed no significant difference from the control, the rate of the elongated nuclei is

DOI:10.15774/PPKE.ITK.2023.003

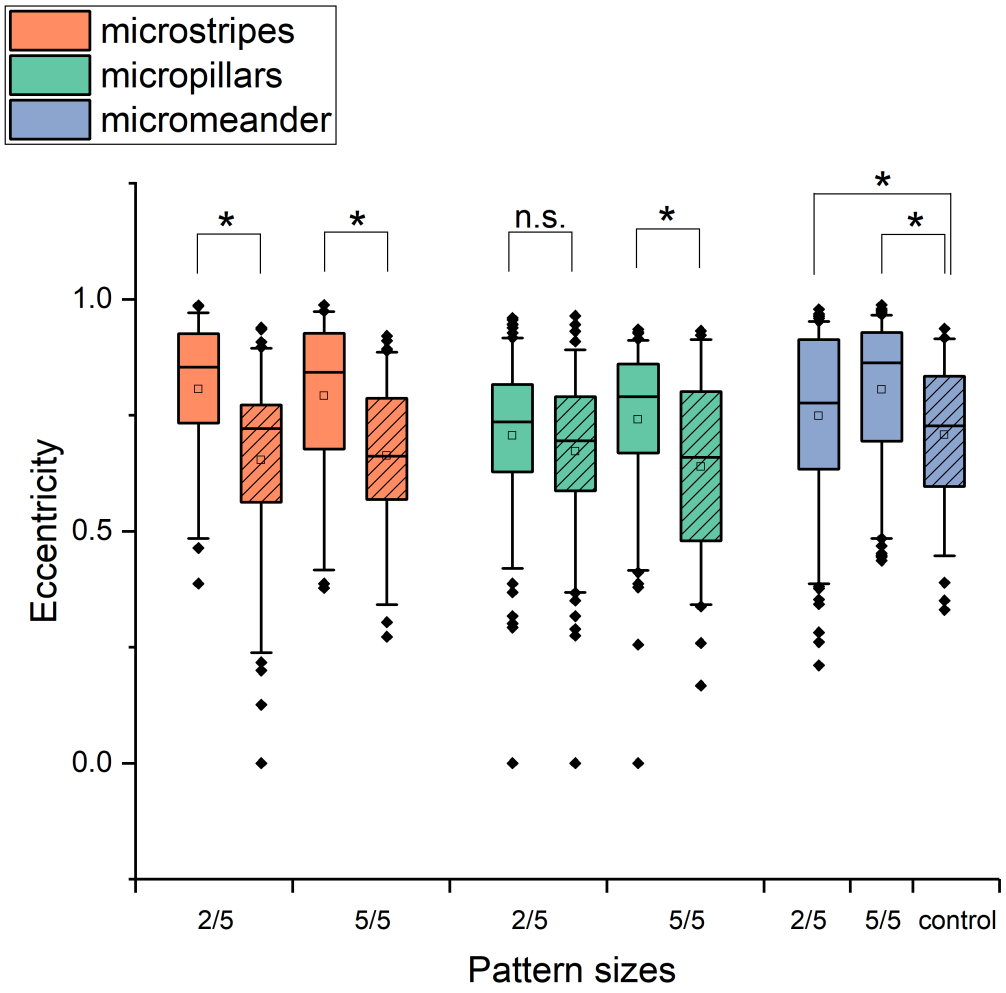

Figure 2.20: Boxplot of the eccentricity values. The lines are the median, small rectangles are the mean values. The Whisker is 5-95, the diamonds represent the outliers. The colors represent the different topographies, the x-axis ticks the different pattern sizes and the box pattern indicates the control case. * symbol implies the significant difference between two datasets based on the Mann-Whitney U-test, shown in Table 2.3.

significantly lower in the case of the control of the 5 µm diameter micropillars. Similar nucleus morphology change was reported on microgrooves in the case of human fibroblasts [29]. Another study also presented a morphological change, where hNT astrocytes altered their typical flat-egg or star-like morphology to conform to the linear grid networks [40].

DOI:10.15774/PPKE.ITK.2023.003

			Microstripes		Micropillars		Micromeander	
			2/5	5/5	2/5	5/5	2/5	5/5
			n=53	n=55	n=146	n=100	n=158	n=166
Microstripes	2/5	n=119	U=4732 p«0.05					
control	5/5	n=91		U=3706 p«0.05				
Micropillars	2/5	n=126			U=10281.5 p=0.09			
control	5/5	n=67				U=4509 p«0.05		
Micromeander control		n=69					U=6431 p=0.03	U=7917 p«0.05

Table 2.3: Result of the Mann-Whitney U-test about the elongation distribution. Blue represents the significant difference and orange represents the non-significant difference.

2.4. Conclusion

In my work, I investigated the effect of SU-8 micropatterns on parameters of astrocyte nuclei shortly after attachment in vitro. I showed that the surface effects can be studied due to the cell nuclei that allow simple detection of fluorescent microscope images. The cell numbers and average nuclei sizes indicate that astrocytes can attach to the patterned SU-8 surfaces better than to the flat SiO_2 surface and the patterns affect the nucleus sizes. The results suggest that the microgrooves orient the nuclei of the astrocytes even in an early stage of cell attachment, while micropillars do not influence the elongation of the attached cells' nuclei. The elongation rate was examined with grooves, pillars, and meander patterns and we found that the surfaces with linear elements as the microstripes, and micromeander elongate astrocyte nuclei by both 2 and 5 µm pattern width and 5 µm spacing. Although the presented SEM images suggest that the cells attach primarily to the surface of the microstructures and span the distance between them, we did not investigate this question in more detail as nuclear staining in itself was not suitable to provide an answer. To equip the surface of silicon-based neural interfaces with additional SU-8 microstructures, microstripes can improve the cell guiding properties and enhance the number of attached astrocytes. According to my observations, microstripes with

DOI:10.15774/PPKE.ITK.2023.003

10 µm spacing oriented astrocyte nuclei are the most efficient. This study shows the pattern surface effects can be investigated due to the cell nucleus and astrocytes can attach differently to a patterned SU-8 surface and a flat SiO_2.

2.5. Thesis statement related to this chapter

I investigated the interaction of micropatterned SU-8 surface - 2 or 5 µm in diameter micropillars with an inter-pillar distance of 3/5/10 µm, 2 or 5 µm wide microsrtipes, spaced 3/5/10 µm and micromeander with the width of 2 or 5 µm and 5 µm spacing - and primer mice astrocytes with a custom-made automatic detection program on fluorescent microscope images after 24 and 48 hours of the seeding.

T1.1. I counted the cell numbers and the area of the nuclei on different patterns with different fixation times. I showed based on the cell numbers compared to the control that after 48 hours more cells are detected over any patterned SU-8 surface than over the flat SiO_2 surface. The average nucleus area in the presence of microstripes and micropillars is smaller than on a smooth SiO_2 surface. I examined the cell numbers together with the average nucleus size and I found that the cells adhered to the patterned surface to a greater extent than to the flat control surface, but the patterns caused a smaller nucleus size.

T1.2. I studied the orientation of the cell nuclei and I found that microstripes force more than 50% of the cells to accommodate the pattern at an angle less than 15° with respect to pattern direction in case of all used spacing size with 2 µm wide microstripes both after 24 and 48 hours. In the case of the 5 µm wide microstripes, the 5 and 10 µm spacing align the cell nucleus after 24 hours, and this alignment happens for all three examined spacing after 48 hours. The 2 µm wide microstripes with 10 µm spacing have the greatest effect on orientation after the cell adhesion. Patterns with micropillars have no major effect on astrocyte nuclei compared to a smooth control surface.

T1.3. The elongation rate was examined with grooves, pillars, and meander pattern and I found that the surfaces with linear elements as the microstripes, and micromeander elongate astrocyte nuclei by both 2 and 5 µm pattern width and 5 µm spacing. The results confirmed that the morphology of the nucleus is an appropriate indicator to examine the effect of micropattern surfaces on cell culture evolution.

DOI:10.15774/PPKE.ITK.2023.003

2.6. Publications related to the thesis points

J1. **Szabó, Á.**, Liliom, H., Fekete, Z., Schlett, K., & Pongrácz, A, "SU-8 microstructures alter the attachment and growth of glial cells in vitro," *Materials Today Communications, 27, 102336*, 2021. Available: `https://doi.org/10.1016/j.mtcomm.2021.102336`. Impact factor: 3.383

C1. Pongrácz A, Barna S, Lukács I, Illés L, Liliom H, Lajer P, Csernyus B, **Szabó Á**, Bérces Z, Fekete Z, Lőw P, Schlett K, "Modification of Glial Attachment by Surface Nanostructuring of SU-8 Thin Films," *Proceedings.* 2(13):1016, 2018. Available: `https://doi.org/10.3390/proceedings2131016`

Other publications:

Szabó, Á., "The effects on cell attachment of surface nanostructuring of SU-8 thin films," *Phd Proceedings Annual Issues of the Doctoral School Faculty of Information Technology and Bionics*, vol. 14 : 2019 p. 131, 2019.

Szabó, Á., "How do astroglia cells react to structured SU-8 thin films?," *Phd Proceedings Annual Issues of the Doctoral School Faculty of Information Technology and Bionics*, vol. 15 : 2020 p. 131, 2020.

2.7. References

[1] K. V. D. Mark, J. Park, S. Bauer, and P. Schmuki, "Nanoscale engineering of biomimetic surfaces: Cues from the extracellular matrix," *Cell and Tissue Research*, vol. 339, pp. 131–153, 1 2010.

[2] A. Schousboe, L. K. Bak, and H. S. Waagepetersen, "Astrocytic control of biosynthesis and turnover of the neurotransmitters glutamate and gaba," *Frontiers in Endocrinology*, vol. 4, p. 102, 8 2013.

[3] M. V. Sofroniew and H. V. Vinters, "Astrocytes: Biology and pathology," *Acta Neuropathologica*, vol. 119, pp. 7–35, 1 2010.

[4] B. A. Macvicar and E. A. Newman, "Astrocyte regulation of blood flow in the brain," *Cold Spring Harbor Perspectives in Biology*, vol. 7, p. a020388, 5 2015.

DOI:10.15774/PPKE.ITK.2023.003

[5] J. W. Salatino, K. A. Ludwig, T. D. Kozai, and E. K. Purcell, "Glial responses to implanted electrodes in the brain," *Nature biomedical engineering*, vol. 1, no. 11, pp. 862–877, 2017.

[6] C. Simitzi, A. Ranella, and E. Stratakis, "Controlling the morphology and outgrowth of nerve and neuroglial cells: The effect of surface topography," *Acta Biomaterialia*, vol. 51, pp. 21–52, 3 2017.

[7] H. Baac, J. H. Lee, J. M. Seo, T. H. Park, H. Chung, S. D. Lee, and S. J. Kim, "Submicron-scale topographical control of cell growth using holographic surface relief grating," *Materials Science and Engineering C*, vol. 24, pp. 209–212, 1 2004.

[8] O. Dial, C. C. Cheng, and A. Scherer, "Fabrication of high-density nanostructures by electron beam lithography," *Journal of Vacuum Science & Technology B: Microelectronics and Nanometer Structures Processing, Measurement, and Phenomena*, vol. 16, p. 3887, 12 1998.

[9] Z. Bérces, K. Tóth, G. Márton, I. Pál, B. Kováts-Megyesi, Z. Fekete, I. Ulbert, and A. Pongrácz, "Neurobiochemical changes in the vicinity of a nanostructured neural implant," *Scientific Reports 2016 6:1*, vol. 6, pp. 1–11, 10 2016.

[10] H. Liliom, P. Lajer, Z. Bérces, B. Csernyus, Ágnes Szabó, D. Pinke, P. Lőw, Z. Fekete, A. Pongrácz, and K. Schlett, "Comparing the effects of uncoated nanostructured surfaces on primary neurons and astrocytes," *Journal of Biomedical Materials Research - Part A*, vol. 107, pp. 2350–2359, 2019.

[11] Z. Bérces, J. Pomothy, C. Horváth, T. Kohidi, Benyei, Z. Fekete, E. Madarász, and A. Pongrácz, "Effect of nanostructures on anchoring stem cell-derived neural tissue to artificial surfaces," *Journal of Neural Engineering*, vol. 15, p. 056030, 9 2018.

[12] C. H. Lee, Y. W. Cheng, and G. S. Huang, "Topographical control of cell-cell interaction in c6 glioma by nanodot arrays," *Nanoscale Research Letters*, vol. 9, pp. 1–11, 2014.

[13] C. A. Chapman, H. Chen, M. Stamou, J. Biener, M. M. Biener, P. J. Lein, and E. Seker, "Nanoporous gold as a neural interface coating: Effects of topography, surface chemistry, and feature size," *ACS Applied Materials and Interfaces*, vol. 7, pp. 7093–7100, 4 2015.

[14] C. D. Johnson, J. M. Zuidema, K. R. Kearns, A. B. Maguire, G. P. Desmond, D. M. Thompson, and R. J. Gilbert, "The effect of electrospun fiber diameter on astrocyte-mediated neurite guidance and protection," *ACS Applied Bio Materials*, vol. 2, pp. 104–117, 1 2019.

[15] K. Anselme, N. T. Wakhloo, P. Rougerie, and L. Pieuchot, "Role of the nucleus as a sensor of cell environment topography," *Advanced Healthcare Materials*, vol. 7, p. 1701154, 4 2018.

[16] E. S. Ereifej, S. Khan, G. Newaz, J. Zhang, G. W. Auner, and P. J. VandeVord, "Characterization of astrocyte reactivity and gene expression on biomaterials for neural electrodes," *Journal of Biomedical Materials Research Part A*, vol. 99A, pp. 141–150, 10 2011.

[17] P. M. Davidson, H. Özçelik, V. Hasirci, G. Reiter, and K. Anselme, "Microstructured surfaces cause severe but non-detrimental deformation of the cell nucleus," *Advanced Materials*, vol. 21, pp. 3586–3590, 9 2009.

[18] P. M. Davidson, O. Fromigué, P. J. Marie, V. Hasirci, G. Reiter, and K. Anselme, "Topographically induced self-deformation of the nuclei of cells: Dependence on cell type and proposed mechanisms," *Journal of Materials Science: Materials in Medicine*, vol. 21, pp. 939–946, 3 2010.

[19] Z. Pan, C. Yan, R. Peng, Y. Zhao, Y. He, and J. Ding, "Control of cell nucleus shapes via micropillar patterns," *Biomaterials*, vol. 33, pp. 1730–1735, 2 2012.

[20] E. Kim, J. Y. Kim, and H. Choi, "An su-8-based microprobe with a nanostructured surface enhances neuronal cell attachment and growth," *Micro and Nano Systems Letters*, vol. 5, p. 28, 12 2017.

[21] Z. Z. Wu, Y. Zhao, and W. S. Kisaalita, "Interfacing sh-sy5y human neuroblastoma cells with su-8 microstructures," *Colloids and Surfaces B: Biointerfaces*, vol. 52, pp. 14–21, 9 2006.

[22] K. V. Nemani, K. L. Moodie, J. B. Brennick, A. Su, and B. Gimi, "In vitro and in vivo evaluation of su-8 biocompatibility," *Materials Science and Engineering: C*, vol. 33, pp. 4453–4459, 10 2013.

[23] G. Márton, E. Z. Tóth, L. Wittner, R. Fiáth, D. Pinke, G. Orbán, D. Meszéna, I. Pál, E. L. Győri, Z. Bereczki, Ágnes Kandrács, K. T. Hofer, A. Pongrácz, I. Ul-

bert, and K. Tóth, "The neural tissue around su-8 implants: A quantitative in vivo biocompatibility study," *Materials Science and Engineering C*, vol. 112, p. 110870, 7 2020.

[24] A. D. Campo and C. Greiner, "Su-8: a photoresist for high-aspect-ratio and 3d submicron lithography," *Journal of Micromechanics and Microengineering*, vol. 17, p. R81, 5 2007.

[25] R. Daunton, A. J. Gallant, and D. Wood, "Manipulation of exposure dose parameters to improve production of high aspect ratio structures using su-8," *Journal of Micromechanics and Microengineering*, vol. 22, p. 075016, 7 2012.

[26] S. Arscott, "Su-8 as a material for lab-on-a-chip-based mass spectrometry," *Lab on a Chip*, vol. 14, pp. 3668–3689, 8 2014.

[27] Kayaku Advanced Materials, "Su-8 2000.5-2015 data sheet." `https://kayakuam.com/wp-content/uploads/2020/08/KAM-SU-8-2000-2000.5-2015-Datasheet-8.13.20-final.pdf`, 2020. Accessed: 2022-07-18.

[28] K. Tárnok, L. Szilágyi, T. Berki, P. Németh, L. Gráf, and K. Schlett, "Anoxia leads to a rapid translocation of human trypsinogen 4 to the plasma membrane of cultured astrocytes," *Journal of Neurochemistry*, vol. 115, pp. 314–324, 10 2010.

[29] M. J. Dalby, M. O. Riehle, S. J. Yarwood, C. D. Wilkinson, and A. S. Curtis, "Nucleus alignment and cell signaling in fibroblasts: Response to a micro-grooved topography," *Experimental Cell Research*, vol. 284, pp. 272–280, 4 2003.

[30] K. Wang, A. Bruce, R. Mezan, A. Kadiyala, L. Wang, J. Dawson, Y. Rojanasakul, and Y. Yang, "Nanotopographical modulation of cell function through nuclear deformation," *ACS Applied Materials and Interfaces*, vol. 8, pp. 5082–5092, 3 2016.

[31] W. W. Ahmed, T. Wolfram, A. M. Goldyn, K. Bruellhoff, B. A. Rioja, M. Möller, J. P. Spatz, T. A. Saif, J. Groll, and R. Kemkemer, "Myoblast morphology and organization on biochemically micro-patterned hydrogel coatings under cyclic mechanical strain," *Biomaterials*, vol. 31, pp. 250–258, 1 2010.

[32] C. P. Unsworth, H. Holloway, E. Delivopoulos, A. F. Murray, M. C. Simpson, M. E. Dickinson, and E. S. Graham, "Patterning and detailed study of human hnt astrocytes on parylene-c/silicon dioxide substrates to the single cell level," *Biomaterials*, vol. 32, no. 27, pp. 6541–6550, 2011.

[33] T. Vignaud, L. Blanchoin, and M. Théry, "Directed cytoskeleton self-organization," *Trends in Cell Biology*, vol. 22, pp. 671–682, 12 2012.

[34] E. K. Yim, E. M. Darling, K. Kulangara, F. Guilak, and K. W. Leong, "Nanotopography-induced changes in focal adhesions, cytoskeletal organization, and mechanical properties of human mesenchymal stem cells," *Biomaterials*, vol. 31, pp. 1299–1306, 2 2010.

[35] H. Y. Lou, W. Zhao, X. Li, L. Duan, A. Powers, M. Akamatsu, F. Santoro, A. F. McGuire, Y. Cui, D. G. Drubin, and B. Cui, "Membrane curvature underlies actin reorganization in response to nanoscale surface topography," *Proceedings of the National Academy of Sciences of the United States of America*, vol. 116, pp. 23143–23151, 11 2019.

[36] S. Ankam, M. Suryana, L. Y. Chan, A. A. K. Moe, B. K. Teo, J. B. Law, M. P. Sheetz, H. Y. Low, and E. K. Yim, "Substrate topography and size determine the fate of human embryonic stem cells to neuronal or glial lineage," *Acta Biomaterialia*, vol. 9, pp. 4535–4545, 1 2013.

[37] F. Badique, D. R. Stamov, P. M. Davidson, M. Veuillet, G. Reiter, J.-N. Freund, C. M. Franz, and K. Anselme, "Directing nuclear deformation on micropillared surfaces by substrate geometry and cytoskeleton organization," *Biomaterials*, vol. 34, no. 12, pp. 2991–3001, 2013.

[38] F. Meng, V. Hlady, and P. A. Tresco, "Inducing alignment in astrocyte tissue constructs by surface ligands patterned on biomaterials," *Biomaterials*, vol. 33, no. 5, pp. 1323–1335, 2012.

[39] T. W. Hsiao, P. A. Tresco, and V. Hlady, "Astrocytes alignment and reactivity on collagen hydrogels patterned with ecm proteins," *Biomaterials*, vol. 39, pp. 124–130, 2015.

[40] M. D. Jordan, B. J. Raos, A. Bunting, A. Murray, E. S. Graham, and C. P. Unsworth, "Human astrocytic grid networks patterned in parylene-c inlayed sio2 trenches," *Biomaterials*, vol. 105, pp. 117–126, 2016.

DOI:10.15774/PPKE.ITK.2023.003

Chapter 3

Characterization of a multimodal neuroimaging method

3.1. Introduction

Several neuroimaging techniques are used to record neural activity and map brain connectivity [1]. These methods used in fundamental research and clinical practice help to understand brain mechanisms and to identify pathological changes that can imply clinical diagnosis. Electrophysiology is the most common neuroimaging method that is still considered as a gold standard [2]. Electrocorticogram (ECoG) is an electrophysiological recording type, where the electrodes are placed on top of the cortex, under the skull [3]. Although ECoG needs surgical implantation, the parameters of signal quality, longevity, and reliability are advantageous compared to the most commonly used electroencephalography (EEG).

Another neuroimaging technique is fluorescence microscopy which allows the examination of intact brain tissue [4]. Before the examination, fluorescent dyes are used to label the cells so the cells can be visualized. One of these fluorescent microscope methods is two-photon microscopy. This method is a laser-scanning technique, where near-infrared light excites the fluorescent labels using two photons, so lower energy and smaller volume are required compared to other fluorescent microscope techniques [5]. Two-photon microscopy indirectly detects cellular changes, so combining it with electrophysiology allows connecting these changes with physiological measures. During the design of such a multimodal experiment, it is important to consider the parameters of the imaging technique that may affect the other modality. The two main requirements from the ECoG device are (1) to be transparent to provide an optical window for the imaging, and (2) to have

DOI:10.15774/PPKE.ITK.2023.003

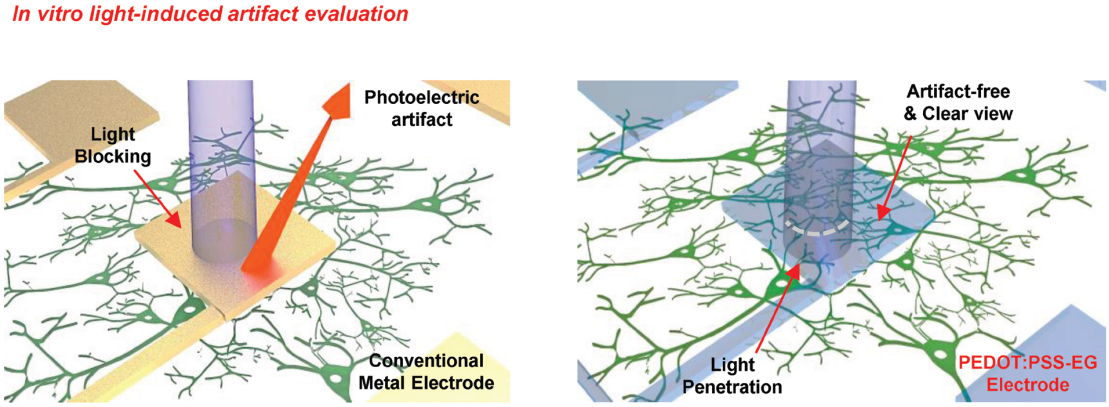

Figure 3.1: Illustration of a light-induced artifact with a conventional metal electrode array (left) and PEDOT:PSS electrode (right) by Cho et al. [24]. The transparency of the proposed device allows imaging neurons through the device and the choosen conductive material is not sensitive to the blue laser pulse, so the measured neural activity pattern is artifact free.

such conductive layers that react with minimal photoartefacts upon laser exposure (Fig. 3.1).

Among transparent substrate materials, Parylene [6, 7] (Fig.3.2.C), SU-8 [8], Polyimide [9, 10], Polydimethylsiloxane (PDMS) [11, 12] (Fig.3.2.A-B), Polyethylene terephthalate (PET) [13, 14], and also a combination of multiple transparent substrates (PET /graphene /SU-8 layers) [15, 16] were proposed. As for the conductive layers, the following materials were presented as transparent, imaging-compatible materials: metal-oxides, e.g. indium-tin-oxide (ITO) [17], metal nanowires[12, 18], nanomeshes [19, 20], carbon nanotubes [21], graphene [16, 22], and conductive polymers, such as Poly(3,4-ethylenedioxythiophene) (PEDOT) [23], and PEDOT:PSS [6, 24, 25] (Fig.3.3).

Previously reported transparent microarrays for two-photon microscopy applications have been tested for multiple parameters to ensure the compatibility of the two recording methods. Impedance spectroscopy is a standard method to test the conductive electrode sites. The average value of the impedance at 1 kHz is an often used form of representation of the measured data [26, 22, 16, 15]. The impedance of the contacts depends on the diameter of the contact point and it changes with time and with the changes in the microenvironment of the device. The long-term stability of the device can be tested with a simulation of the degradation mechanism of electrode material, called the accelerated aging test [27]. The mechanical stability of cortical microarrays is often tested with bending tests with different cycle numbers [26, 16]. Next to the mechanical and electrical

DOI:10.15774/PPKE.ITK.2023.003

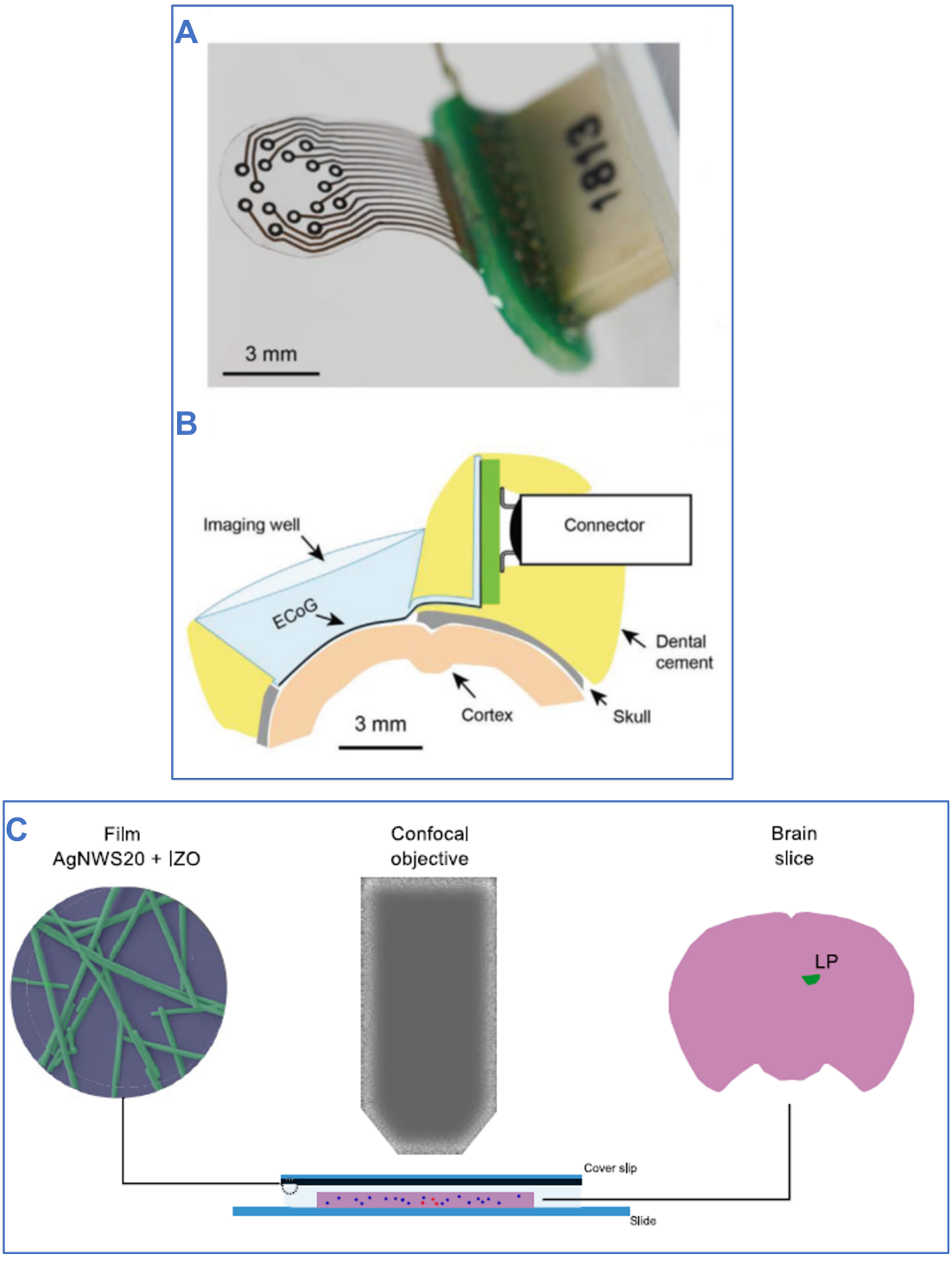

Figure 3.2: Previously presented multimodal applications. A-B) Opto-e-Dura by Renz et al. [11] A) photograph of the ECoG array. B) shematic cross section of the implanted device with the used imaging well. C) Schematic setup of Neto's Parylene C based device with silver nanowires (AgNWs) with indium zinc oxide electrodes using confocal microscopy. Mouse brain slice was placed between the glass slide and a cover slip during imaging [7].

DOI:10.15774/PPKE.ITK.2023.003

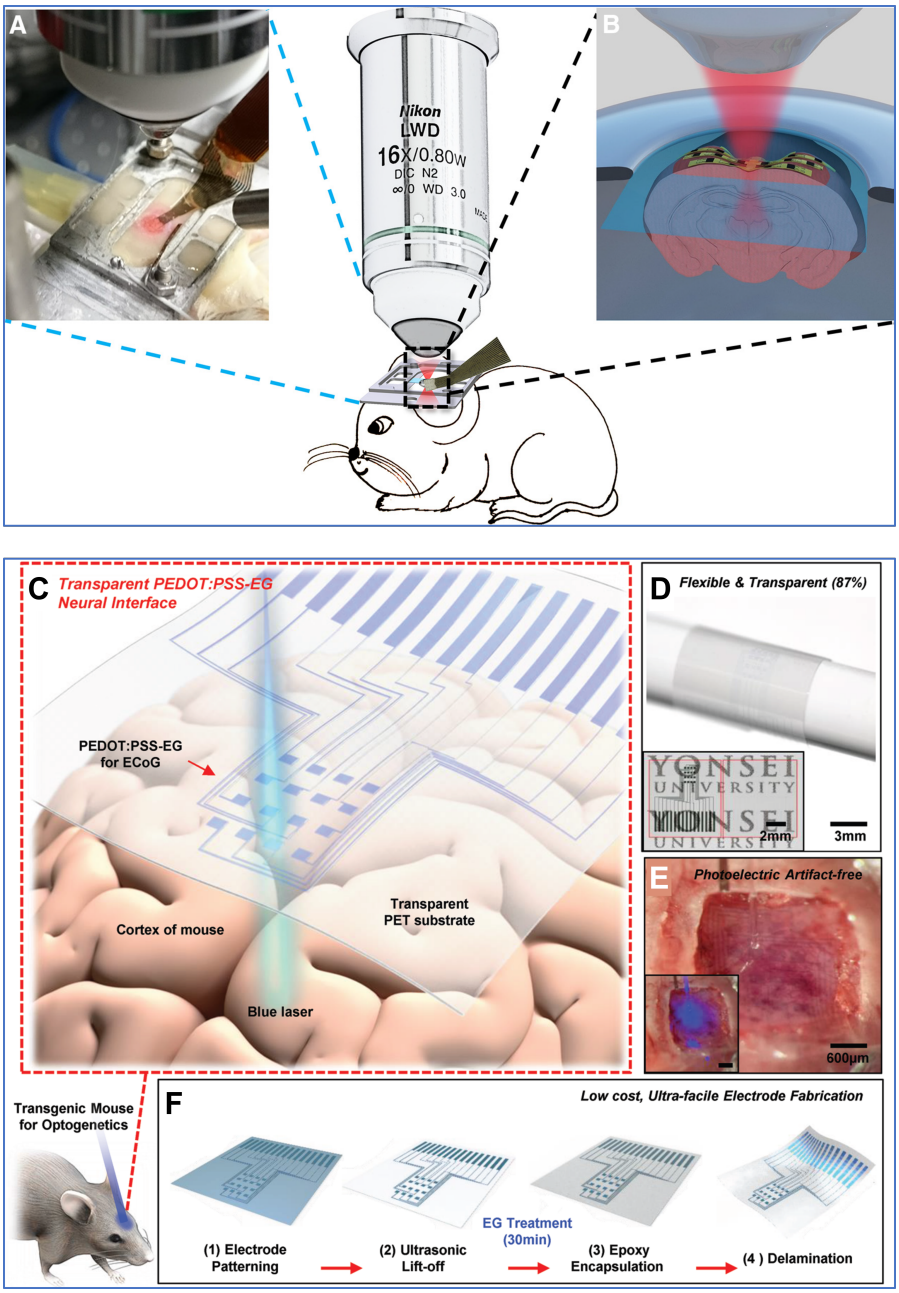

Figure 3.3: Previously presented multimodal applications. A-B) Layout of PEDOT:PSS-based device with a two-photon microscope by Donahue et al. [25] A) Photo of anesthetized animal's headplate with the probe positioned on the cortex under the objective. B) The infrared laser beam passes through the grid of organic electrodes. C-F) Simultaneous electrophysiology and optogenetics with ethylene-glycol-treated PEDOT:PSS device by Cho et al. [24] C) schematic illustration of the experimental setup. D) Representing the flexibility (wrapped around a 5-mm diameter cylindrical rod) and transparency of the device. E) image of the photoelectric artifact-free PEDOT:PSS-EG electrode array implanted on the rodent cerebral cortex. F) Fabrication process of the device.

DOI:10.15774/PPKE.ITK.2023.003

stability of the device, it is important to test the optical parameters of these materials, since they are between the sample plane and the microscope objective. The transmittance in different ranges of wavelength with the measured percentage [26, 22, 16] and the autofluorescence [26] of the material are important parameters in terms of compatibility with a microscope technique. Photoartefact is another important optical parameter of multimodal neuroimaging. This measurement is possible ex vivo [22, 15] and also in vitro [26, 16]. The image quality and spatial resolution are also tested with different methods. Next to the usage of fluorescent microbeads [16], the Ca^{2+} imaging on hippocampal slices [26, 22, 15] is also used to measure the changes in image quality that may occur in the presence of the transparent device.

The characteristics of ITO, such as its flexibility, optical, and photovoltaic characteristics, and biocompatibility, make this conductive material appropriate for measurements with concurrent microscope imaging. ITO is a large bandgap semiconductor that exhibits high optical transparency (generally >80 %, depending on the thickness) [28, 29]. The application of large bandgap semiconductors limits light-induced artefacts [30], which is beneficial to maintain high quality electrophysiological recording during image acquisition as well. Transparency, flexibility, and biocompatibility are important in the case of substrate materials. Next to the widespread Parylene C, Parylene HT is a rarely used polymer, although its transmittance and autofluorescence level [31] are outstanding. In this work, the goal was to present the compatibility of Parylene HT/ITO/Parylene HT based microECoG array with two-photon Ca^{2+} imaging. My work specifically focused on analyzing the influence of the concurrent use of electrophysiology and calcium imaging on optical and electrical signals.

3.2. Methods

3.2.1 Microfabrication and packaging

The 16 micron-thick 32-channel microelectrode array is composed of Parylene HT (SCS, UK) substrate and 100 nm thick indium-tin-oxide (ITO) conductive layer. Its microfabrication relies on MEMS technologies including photolithography, bulk micromachining, and high-aspect-ratio micromachining steps. The microfabrication steps are shown in Fig. 3.4. The design and manufacturing were made by Anita Zátonyi and Zoltán Fekete at the Microsystems Laboratory of the Centre for Energy Research, Institute of Technical Physics and Materials Science. First, a DSP silicon wafer was immersed to a 1:20 HF

DOI:10.15774/PPKE.ITK.2023.003

solution for 30 seconds. 8 microns thick Parylene HT is chemical vapour deposited on the wafer. Before the deposition, a releasing agent was used then the dimer is vaporized at 150 °C under vacuum into a dimeric gas form then the gas is pyrolyzed (690°C, 0.5 torr) to cleave the dimer to its monomeric form. In the room temperature deposition chamber the monomer gas deposits on silicon wafer surfaces and becomes a transparent polymer layer. The lift-off pattern for the conductive layer was created with Ti35 Image reversal resist (Microchemicals GmbH, Germany) (Fig.3.4/1.). The photoresist was spin-coated at 4000 rpm for 45 seconds, then baked at 100 °C for 2 minutes on a hotplate. Karl Süss MA6 Mask Aligner (Suss Microtec Ag, Germany) was used for UV light exposure using a UV dose of 200 mJ/cm^2 followed by a relaxation time of 10 minutes, and a reversal bake at 130°C for 2 minutes on a hotplate. Second exposure was applied with a UV dose of 500 mJ/cm^2. Oxygen plasma strip at 80 W for 30 seconds (Diener Pico, PCCE, RFG 13.56/300, Diener electronic GmbH + Co. KG) was used before the sputtering to improve the adhesion between the polymer and the metal oxide layer. Indium-tin-oxide was deposited in a Leybold-Heraeus Z550 RF sputtering equipment (Leybold GmbH, Germany) (Fig.3.4/2.). Flow rate of the Ar gas, and RF power to form the plasma were 50 sccm and 300 W, respectively. After ITO deposition wafers were left in the acetone bath until the lift-off was completed (Fig.3.4/3.). Adhesion promoter was applied prior encapsulating layer of 8 micron thick Parylene HT (Fig.3.4/4.). 100 nm aluminium thin film as a hard mask for Deep Reactive Ion Etching an ATC 1800-HY was deposited by an e-beam evaporator equipment (AJA International, Inc., USA) at 2 nm/minutes (step 6). Thin layer of photoresist (Microposit 1818, Rohm and Haas Company, USA) was spin coated at the top of the aluminium layer to form a photolithographic (Fig.3.4/5.). Before UV exposure photoresist was soft baked at 115 °C for 90 seconds on a hotplate. UV light intensity was set to 100 mJ/cm^2, a photolithographic pattern was developed then hard-baked at 110 °C for 30 minutes in a convection oven. Aluminium was wet-etched in a solution of phosphoric acid, acetic acid, and nitric acid (H_2O:H_3PO_4:CH_3COOH:HNO_3 = 2:16:1:1). The exposed Parylene HT surfaces were removed in high-density ICP O2 plasma in a Deep RIE System (Plasmalab 100, Oxford Instruments, UK) at 1000 W power (Fig.3.4/6.). The aluminium masking layer was then removed in 0.025 M NaOH solution at room temperature (Fig.3.4/7.). After soaking the wafers in distilled water for about 2 weeks, arrays were released from the silicon surface (Fig.3.4/8.). Electrode structures were mounted on a 32 channel PreciDiP electrical connector (Preci-dip SA, Switzerland) with a two-component conductive epoxy material (CW2400, Chemtronics,

DOI:10.15774/PPKE.ITK.2023.003

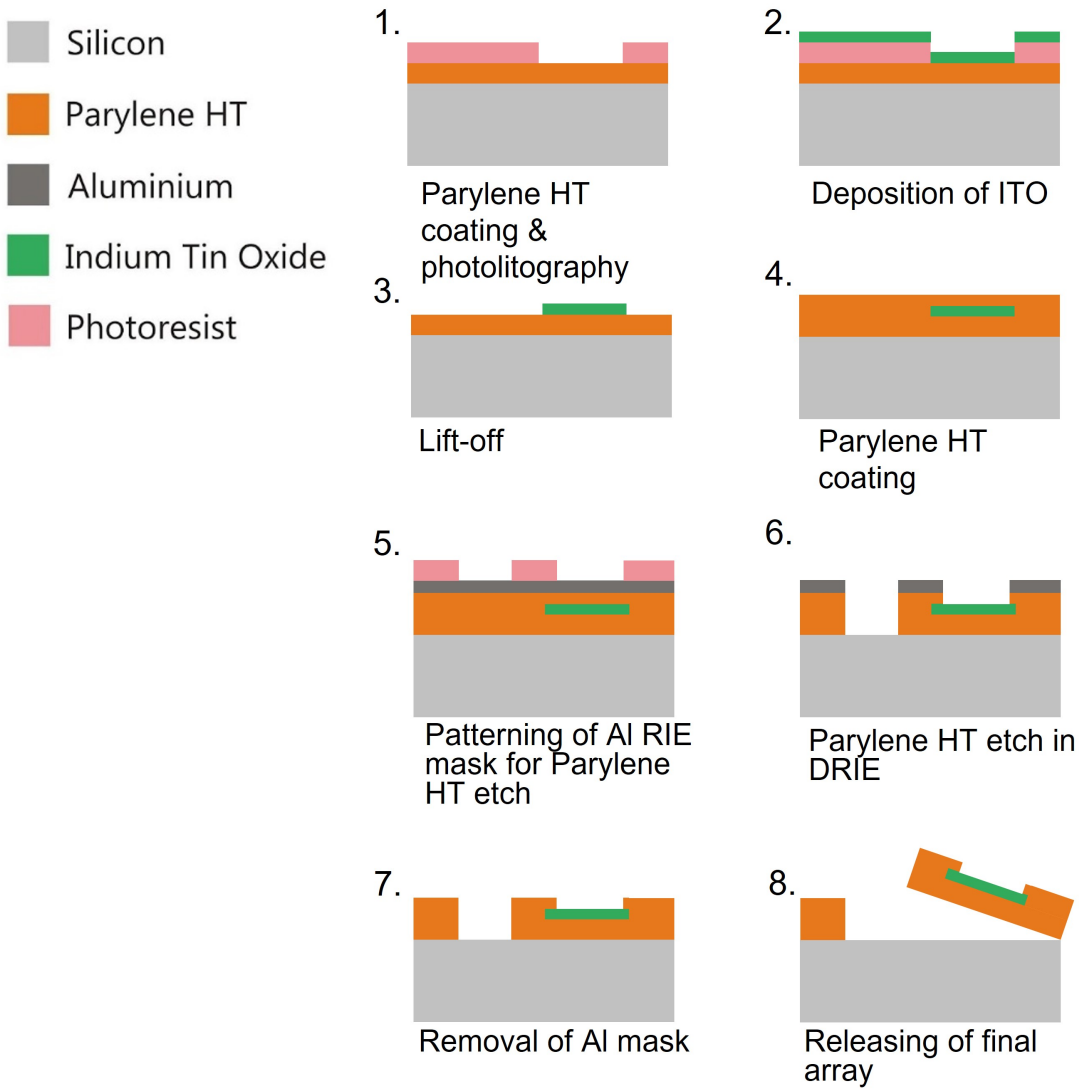

Figure 3.4: Schematic process flow of device fabrication. The detailed steps are described in Section 3.2.1.

Georgia, US). The back of the connector pins was protected by a two-component adhesive epoxy paste (Araldite 2014-1, Huntsman Advanced Materials GmbH, Switzerland).

3.2.2 Animals

All of the procedures were in accordance with the Hungarian Act of Animal Care and Experimentation (2013, (II.14), section 40/2013) and approved by the Animal Care and Use Committee of the Government Office (approval: PE/EA/674-2/2019). For in vitro experiments, transgenic FVB/Ant mice of either sex, expressing GCaMP6f under the thy1 promoter and aged 12-15 weeks were used. Animals were housed under controlled temperature, humidity, and lighting, and had free access to food and water.

DOI:10.15774/PPKE.ITK.2023.003

3.2.3 Slice preparation

Acute hippocampal slices were prepared as described previously [32]. Briefly, FVB/Ant transgenic mice expressing GCaMP6f under the thy1 promoter were deeply anesthetized with isoflurane and decapitated. The brain was quickly excised and put into an ice-cold intermediate cutting solution containing (in mM): 2.8 KCl, 1 $MgCl_2$, 2 $MgSO_4$, 1.25 NaH_2PO_4, 1 $CaCl_2$, 10 D-glucose, 26 $NaHCO_3$ and 206 sucrose. 350 µm thick horizontal slices of the hippocampus were prepared with a vibratome (Leica VT1000S) and stored at room temperature in artificial cerebrospinal fluid (aCSF) containing (in mM): 126 NaCl, 2.5 KCl, 2 $CaCl_2$, 2 $MgCl_2$, 1.25 NaH_2PO_2, 26 $NaHCO_3$ and 10 glucose and oxygenated with carbogen gas. For two-photon imaging, slices were transferred to a recording chamber with continuous aCSF perfusion and oxygenation. The slice preparation took place at the Faculty of Information Technology and Bionics by Tibor Lőrincz.

3.2.4 Two-photon imaging

In vitro two-photon imaging was performed on a Femto2D microscope (Femtonics Ltd.). Laser pulses were generated by a Mai Tai HP laser (SpectraPhysics) at 900 nm and delivered through a 20x/1.0NA objective (XLUMPLFLN-W 20x/1.0 NA, Olympus). Signals were detected by a PMT (H7422P-40-MOD, Hamamatsu) separated by a dichroic mirror (700dcxru, Chroma Technology). The beam path in the case of galvanic and resonant scanning is shown in Fig. 3.5. The two-photon imaging was performed by Miklós Madarász and Tibor Lőrincz.

DOI:10.15774/PPKE.ITK.2023.003

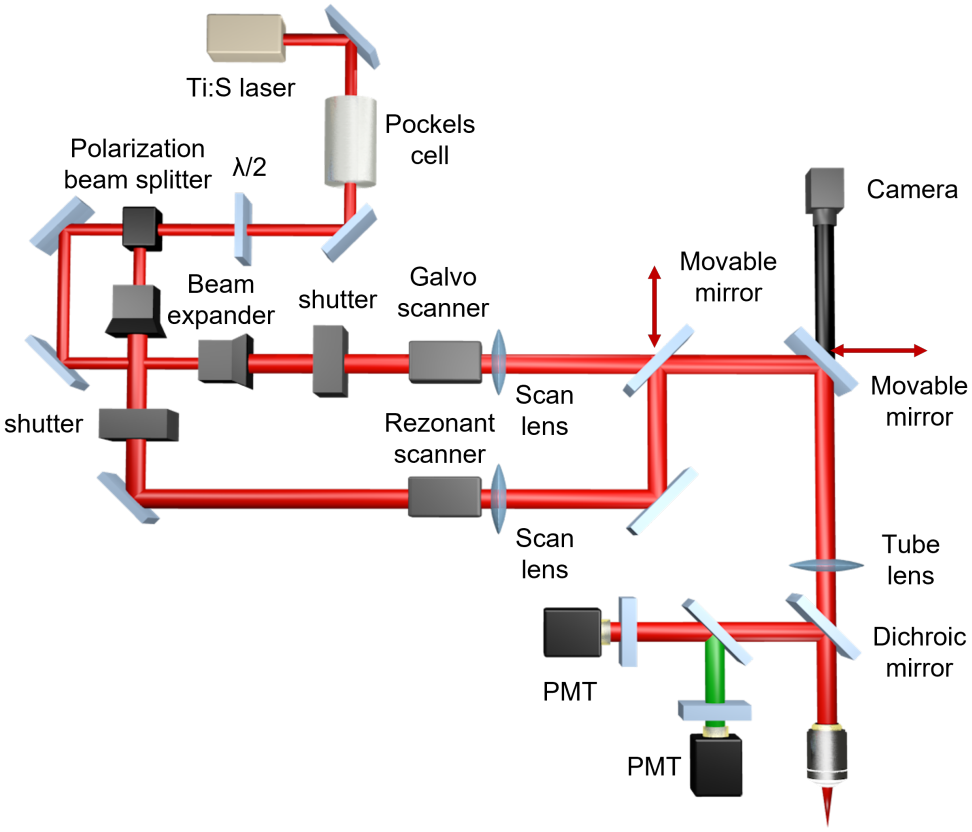

Figure 3.5: Beam path used for in vivo imaging. Key elements are depicted and labeled.

3.2.5 Image quality and spatial resolution

To define the optical distortion of the polymer substrate and indium-tin-oxide, two-photon images were recorded with and without fully fabricated but nonfunctional microelectrode arrays placed on fluorescent microbeads. 6 µm beads (P7220, ThermoFisher) were sealed between two glass coverslips and used for comparison of spatial resolution. Point Spread Function (PSF) was calculated as the FWHM of the gaussian fit of the microbead profile and corrected for the microbead size and normalized to the average PSF size of control beads. Analysis of images was performed with the Matlab-based MES program (Femtonics Ltd.). Mann-Whitney U-test was used to compare apparent bead size between groups of fluorescent microbeads (n=10) with or without the presence of Parylene HT/ITO structure.

A similar test was performed ex vivo, on hippocampal slices. Two-photon images

DOI:10.15774/PPKE.ITK.2023.003

Figure 3.6: Workflow of image processing during the detection of neurites using a custom Matlab-based algorithm, used for the detection of the neurites.

of the CA1 region of the hippocampus were recorded with and without microelectrode arrays. The fluorescence images were analyzed with a custom-made Matlab script (Fig. 3.6). Three-three images were chosen to measure the average diameter of neurites in the same field of view, different z-level. To ensure, that the detected neurite originated from the same depth, the statistical data contains only the neurites detected at a distance between 30 and 70 µm from the cell soma. The used laser power was 72 mW without the device and 22.3 mW with the array in the light path. The significance was examined with Mann-Whitney U-test.

3.2.6 Tests on photoelectric artefacts

To test laser power tolerance and the presence of scanning artefacts, Parylene HT/ITO was immersed into Ringer solution and imaged with both galvanic and resonant scanning while recording with the electrodes. The exact sites of the array were identified according to the layout of the electrode. The field of view was chosen to contain only one site. Laser power was increased step by step (range: 7.7 - 132.4 mW) while recording with the electrode, to characterize photoelectric artefacts of scanning and to determine the maximum laser power to use with the electrode. The highest safe laser power was determined according to the settings of the last image not to cause visible damage. In galvanic mode, we varied laser power between 9.6 mW and 34 mW and Z-level between 0 µm and -30 µm relative to Parylene HT/ITO surface. For galvanic scanning, all images were 500x500 pixels in size (pixel size is 0.95 µm), acquired with a 2.11 Hz frame rate (10 frames) at every focal plane and laser power used. In resonant mode, we used laser power between 7.7 mW and 132.4 mW and a Z-level between 0 µm and -30 µm. For resonant scanning, all images were 512x512 pixels, 0.88 µm pixel size, acquired with a 30.98 Hz frame rate (155 frames) at every focal plane and laser power used. Electrode data was recorded with an RHD2000 amplifier board and an RHD 2132 amplifier chip and sampled at 2 kHz. The described measurement was performed by Miklós Madarász.

DOI:10.15774/PPKE.ITK.2023.003

Photoelectric artefacts were evaluated in the frequency domain of the electrical signals, and one case (laser power and focus plane) was analyzed from one scanning recording.

3.3. Results

3.3.1 Spatial resolution of two-photon imaging through the transparent ECoG device

Preliminary bench-top tests on spatial resolution through the Parylene HT/ITO multilayer structure were performed using fluorescent microbeads with a nominal diameter of 6.0 µm (Fig. 3.7.A). Comparison between groups of fluorescent microbeads (covered and not covered with ECoG substrate) was performed using Mann-Whitney U-test. PSF size was found not significantly different when beads were covered with Parylene HT/ITO (control: 6.11 µm (SD=0.18 µm), covered: 6.06 µm (SD=0.16 µm), $p>0.05$, $U=39$, $n=10$).

As an additional test to verify the combined use of Parylene HT/ITO and two-photon imaging before in vivo experiments, I compared image quality with and without Parylene HT/ITO based ECoG using in vitro hippocampal slices of GCaMP6f expressing mice. Cells in the CA1 subregion were clearly visible together with fine dendritic structures in the stratum radiatum when slices were covered with the ECoG array (see Fig.3.7.C and D). The mean size of the neurites under the array was 2.17 µm (SD=0.89 µm) (n=26), while without the array, the mean size of the neurites was 1.73 µm (SD=0.61 µm) (n=29) (Fig. 3.7.B). Comparing the two cases with Mann-Whitney U-test there was a significant difference ($U=234$, $p<0.05$). Despite the significant difference, the presented electrode mesh does not cause greater distortion than the resolution limit (0.5 µm) when placed in the light path. The fine dendritic structures remain detectable.

DOI:10.15774/PPKE.ITK.2023.003

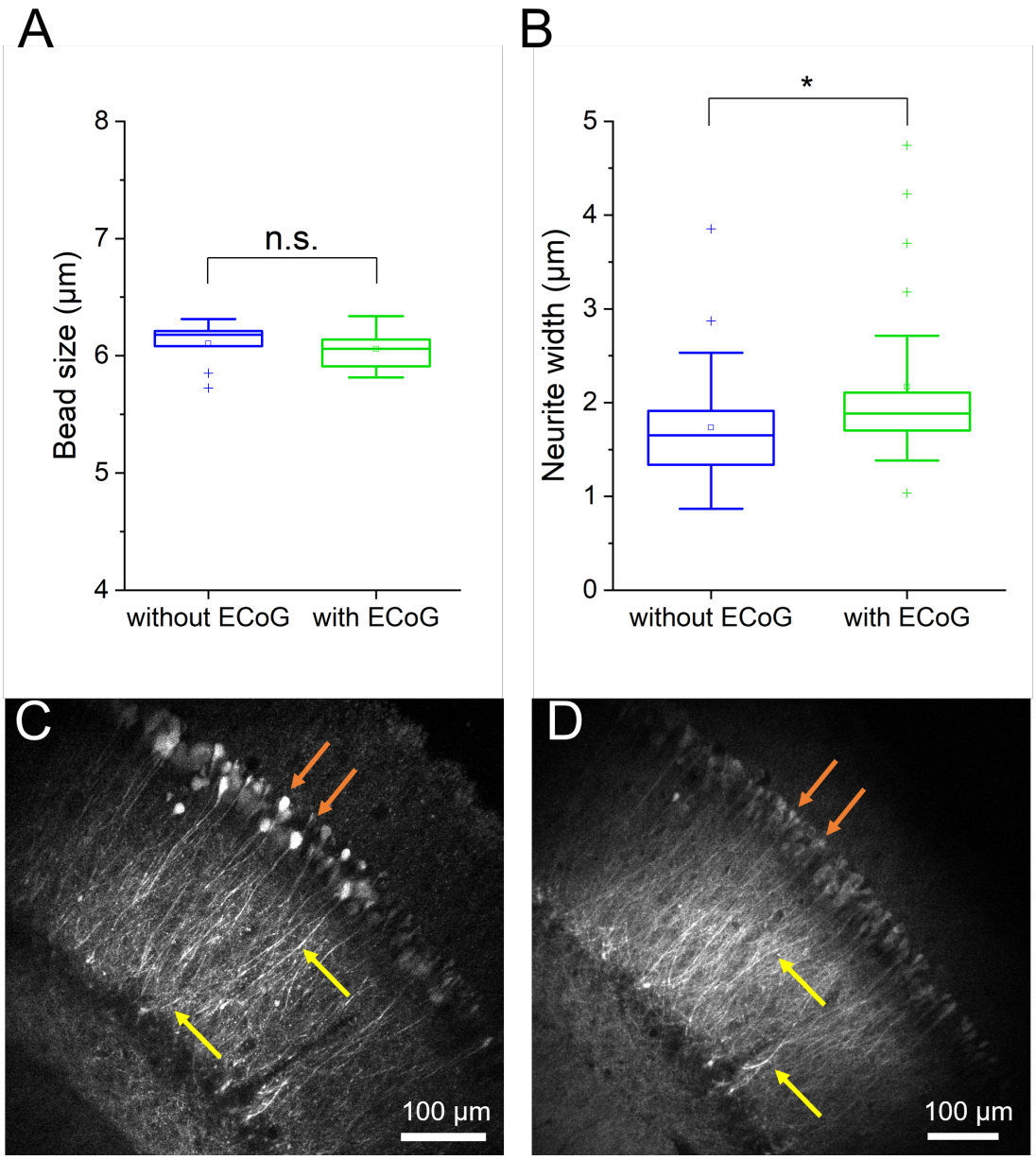

Figure 3.7: (A) Boxplots of microbead size of the 6.0 µm nominal diameter microbeads. Average size without Parylene HT: 6.11 µm (SD=0.18 µm), with Parylene HT: 6.06 µm (SD=0.16 µm). Mann-Whitney U-test, $p>0.05$, U=39, n=10. (B) Boxplot about the measured in vitro neurite width in a distance between 30 and 70 µm from the cell soma. Average neurite width without Parylene HT: 1.73 µm (SD=0.61 µm, n=29), with Parylene HT: 2.17 µm (SD=0.89 µm, n=26). Mann-Whitney U-test, $p<0.05$, U=234. The bottom and top edges of the boxes indicate the 25th and 75th percentiles. The whiskers extend to the most extreme data points not considered outliers, and the outliers are plotted individually using the '+' symbol (Origin built-in boxplot function). Representative fluorescent images of CA1 neurons resolved in hippocampal slices not covered (C) and covered (D) with our transparent ECoG using 72 mW and 22.3 mW. Red and yellow arrows show cell soma and dendrites, respectively. One image is the average of three images from different depths.

DOI:10.15774/PPKE.ITK.2023.003

3.3.2 Evaluation of photoartefacts on two-photon exposed recording sites

Photoelectric artefacts were evaluated with two-photon microscopy using several scanning modes (galvanic and resonant), depth of focal plane with respect to the device plane (distance), and at various intensities of irradiation (laser power) in Ringer solution. The characteristic patterns of photoelectric artefacts are shown in Fig.3.8.A. In both scanning modes, the amplitude of the induced noise is negligible when the laser beam is focused under the contact point. This is the case during in vivo operation, where we are scanning the cells under the ECoG array. When we focus on the plane of the contact, the galvanic scanning mode causes a larger artefact than the resonant mode. Parylene C samples holding Ti/Au metallization were tested in galvanic scanning as control material to compare the light-induced intensity of artefact signals (Fig.3.8.B). The power densities of artefact signals in the focal plane (z=0) of indium-tin-oxide surfaces are well below the value of the control metallization. This trend remained stable at various laser powers (Fig.3.8.B). Power density spectrums also revealed that ITO is more sensitive to galvanic scanning mode than to resonant scanning mode, with respect to light-induced artefacts (Fig.3.8.C). Regarding the investigations at various depths, we noticed that focusing the laser beam at Z = -5 µm in resonant and at Z = -10 µm in galvanic scanning mode under the ITO recording site apparently suppressed the power density of noise using 33 mW and 13 mW laser power in resonant and galvanic scanning mode, respectively (Fig.3.8.D).

DOI:10.15774/PPKE.ITK.2023.003

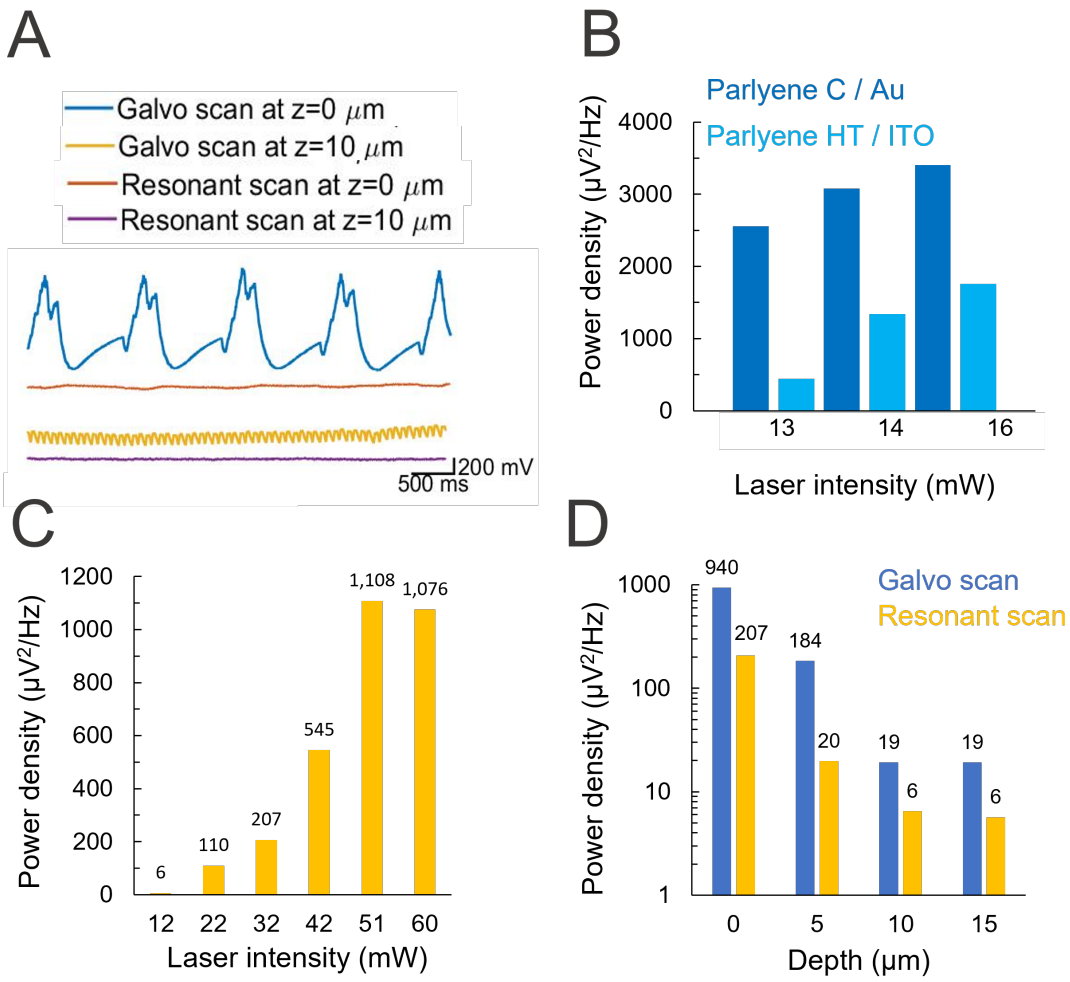

Figure 3.8: (A) Representative curves on the sensitivity of signal recording to photoelectric artefacts at galvanic and resonant scanning modes measured on the device plane (Z = 0 µm) and at Z = -10 µm. (B) Comparison of the photo artefacts of Parylene C/Ti/Au electrodes and Parylene HT/ITO electrodes at various light intensities at the fundamental harmonic for galvanic scanning (2.11 Hz). (C) Maximum power density of noise using various light intensities on a recording site (Z = 0 µm) at the fundamental harmonic of resonant mode (30.98 Hz). (D) Maximum power density of noise at different distances from the device plane. The laser was focused on the site (Z = 0 µm) and under the site in the shown depth. Laser intensities are 13 mW and 33 mW for galvanic and resonant mode, respectively.

DOI:10.15774/PPKE.ITK.2023.003

I compared the spectrum of different laser powers and also the photoartefacts recorded with the same scanning mode but different focal planes. As previously described, with galvanic scanning mode the same laser power generates a smaller artefact on Parylene HT/ ITO electrode, compare to Parylene C/Ti/Au (Fig.3.9 A). Focusing the laser beam by 10 µm under the device plane efficiently reduces the power density of the noise by 13 mW laser power (Fig. 3.9 B). Similarly, I compared the spectrum of the different laser powers and focal planes in the case of resonant scanning (Fig. 3.10). The power density of the noise is reduced using a beam power of 32 mW in the device plane (Fig. 3.10 A). Based on spectrums recorded at various laser powers, we concluded that power values below 12 mW in resonant mode at the device plane (Z = 0) can be safely used without substantial photoelectric artefacts. The scanning with 33 mW laser power showed a reduced power density by setting the focus to 5 µm under the transparent ECoG (Fig. 3.10 B).

With this wide range of measurements, we determined the safety guidelines for our proposed device with two-photon microscopy. During an in vivo measurement, the multimodal recording would operate by focusing the laser under the transparent electrode array, in the second cortical layer. Measuring the noise in case of focusing to the contact point we specified further parameters for a safe operation.

DOI:10.15774/PPKE.ITK.2023.003

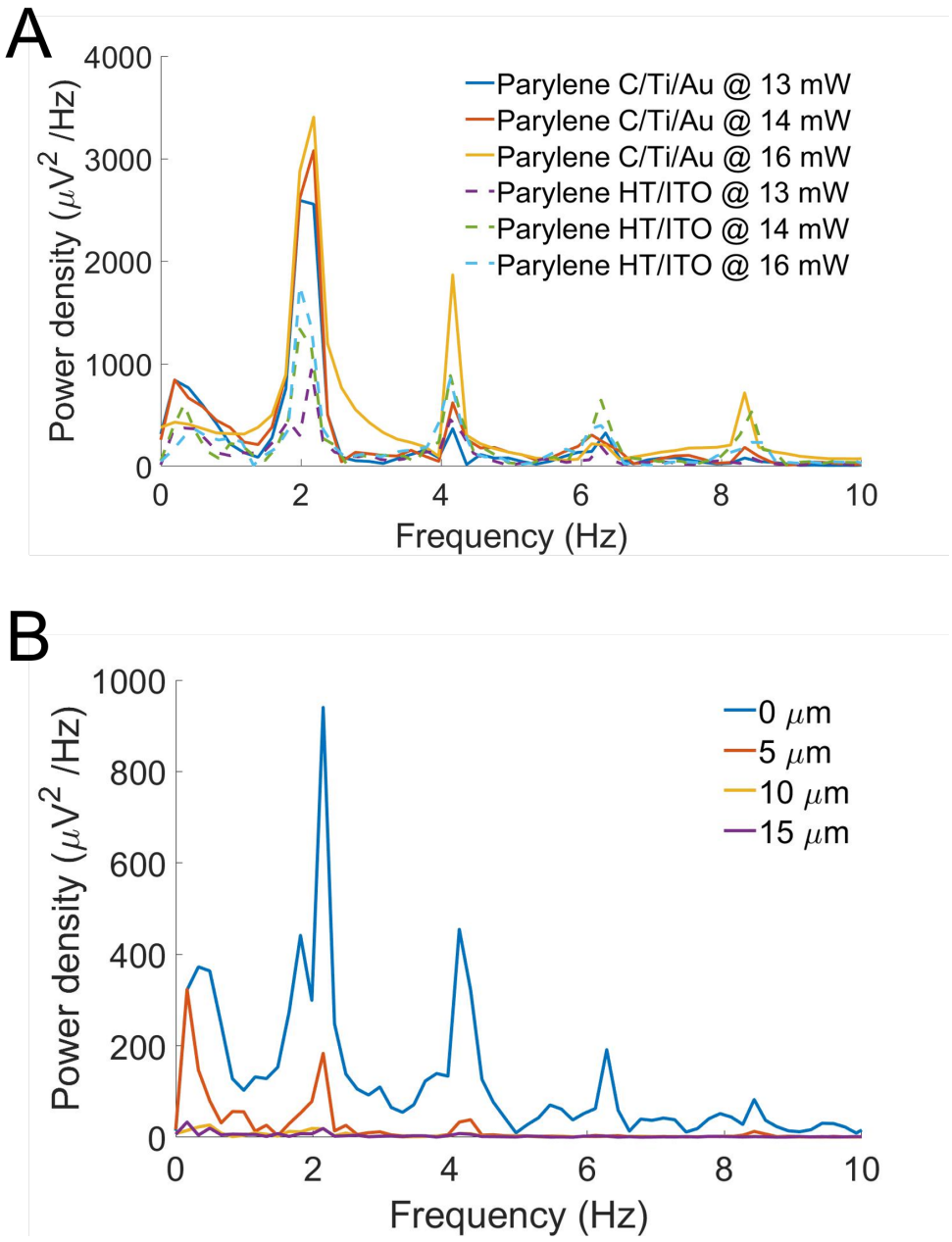

Figure 3.9: A) Comparison of the photo artefacts of Parylene C/Ti/Au electrodes and Parylene HT/ITO electrodes. The used microscope parameters: galvanic scanning with 13, 14, and 16 mW laser power. (B) Galvanic scanning with 13 mW laser power at different distances from the device plane.

DOI:10.15774/PPKE.ITK.2023.003

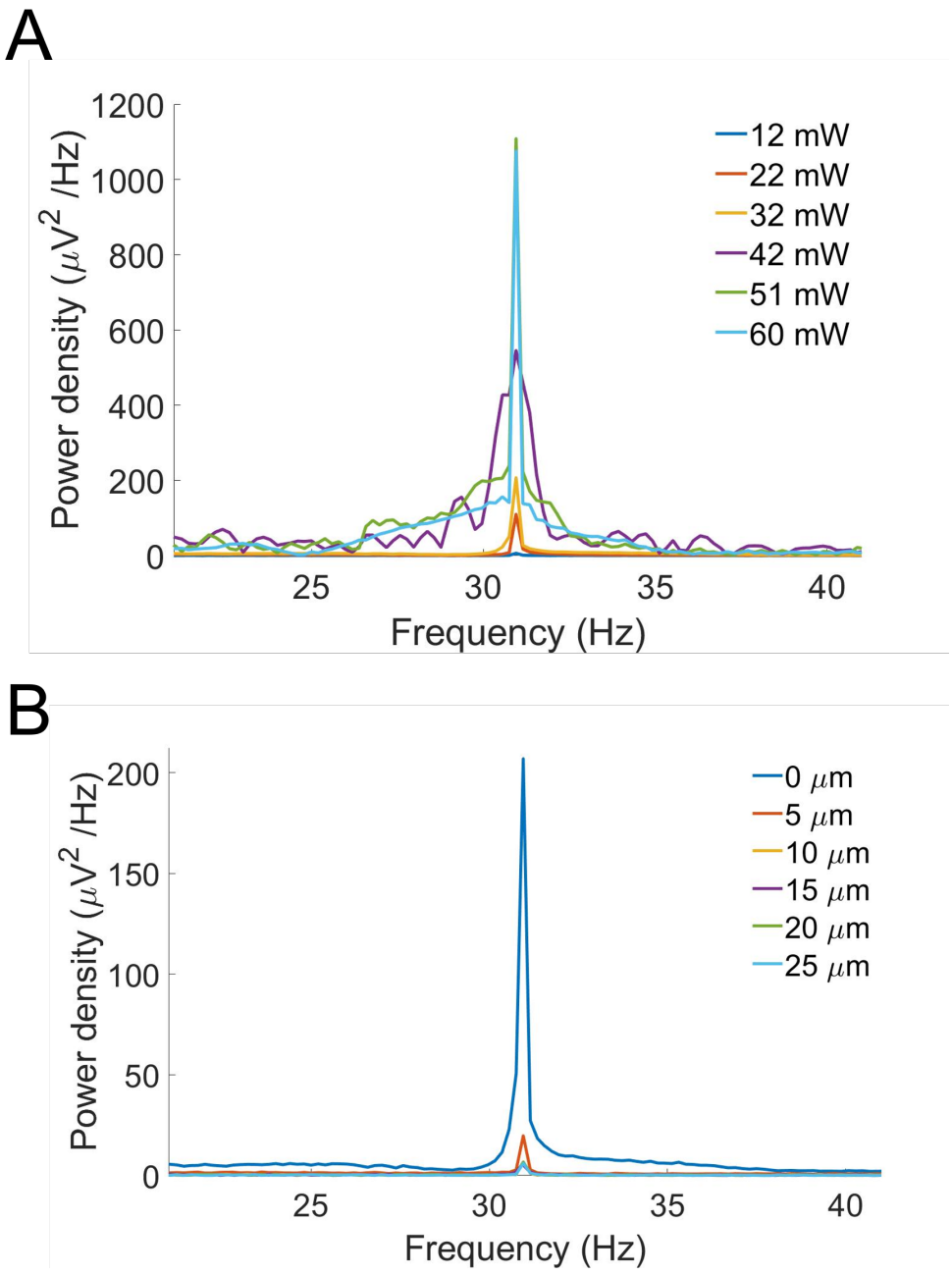

Figure 3.10: A) Resonant scanning spectrum using various laser powers in the device plane (Z = 0 µm). B) Resonant scanning spectrum at different distances from the device plane. The laser was focused on the site (Z = 0 µm) and under the site in the shown depth with the same 33 mW laser power.

DOI:10.15774/PPKE.ITK.2023.003

3.4. Outlook on further carried out tests

Further optical and mechanical tests were carried out on the proposed Parylene HT device by my fellow researchers. Although these results are not part of my dissertation, they highlight the feasibility of a multimodal recording with Parylene HT ECoG and two-photon microscopy.

To investigate the optical properties of Parylene HT substrate materials, visible–near-infrared (VIS-NIR, wavelength of 380 - 980 nm) and autofluorescence (260 – 600 nm excitation, 270 – 800 nm emission wavelength) spectroscopy with a fluorimetric device were performed by Anita Zátonyi. Besides Parylene HT, Parylene C was also evaluated as a reference material frequently used in other studies. Based on the fluorescence and transmittance spectra, Parylene HT is far superior for the proposed imaging task than Parylene C.

High-intensity laser scanning is known to have possible adverse effects on the sample due to heating. While this is taken into consideration for living tissue, it is also important to quantify this effect on implanted devices, as deformation of the ECoG array would impair long-term experiments. To address this issue, Miklós Madarász investigated the vulnerability of the array to two-photon scanning by exposing it to high laser power in Ringer solution. The safe-to-use laser intensity limits were determined based on these photodegradation tests.

Furthermore, in vivo measurements were made. To test the suitability of the electrode array in long-lasting chronic experiments my fellow researchers have been monitoring the visibility of cells for weeks and could conclude that it was limited by GCaMP6f expression and not by the continuous presence of the electrode array.

3.5. Discussion and conclusion

This work aimed to demonstrate the application of Parylene HT as a biocompatible polymer substrate and encapsulation material with indium-tin-oxide (ITO) as a conductive layer in transparent microECoG devices. My study revealed several advantages that maintained the performance of two-photon imaging when such a device is implanted and located in between the microscope objective and the living tissue.

Prior studies used non-transparent metal traces, which limited the active surface for neuroimaging through the ECoG device to the close vicinity of the recording sites made of graphene [33, 34] or bilayer-nanomesh [26] structures. Previously, the use of ITO

DOI:10.15774/PPKE.ITK.2023.003

for ECoG recording has been successfully demonstrated for recording purposes without additional metal layers by this group [10].

To show the outstanding optical performance of the proposed ECoG structure, the spatial resolution of two-photon imaging was tested using microbeads, and hippocampal slices. Based on statistical analysis, there was no remarkable difference in measured bead sizes when beads were covered and not covered with the transparent ECoG. Dendritic structures were clearly identified on brain slices without remarkable optical distortion. These experiments also revealed that scanned volume even underneath the ITO recording site arrays and wirings provides high resolution of neuronal structures.

Besides the optical, electrical, and mechanical performance of the transparent ECoG device, its integrity under two-photon exposure was also tested. These data serve as a safety guideline for future users to avoid either device failure or injury of the investigated tissue. Maximum laser powers were determined for both galvanic and resonant scanning modes at different depths relative to the surface of the device. Our results revealed that below the limits of 13 mW in galvanic and 33 mW in resonant scanning mode, direct exposure on the device layer does not cause any visible degradation. In real experiments, neural cells are located well below the superficial layer of the cortex, so the explicit scanning of the laser beam on the surface of the device is not a practical issue. Focusing the laser beam below the ECoG device, the amount of permissible optical power can be remarkably increased without the impairment of the transparent device.

Light-induced artefacts have to be considered, next to photodegradation, when the optimal distance of the focal plane from the device is determined. Electrical artefacts on both ITO and Ti/Au (control) recording sites were quantified during galvanic and resonant scanning with various laser powers and at various distances from the device plane. In general, laser exposure 10 µm below the device plane does not induce apparent noise in the signal, while low power exposure close to the device plane contributes to parasite peaks in the power density spectra, where the fundamental frequency is corresponding to the frame rate of image acquisition.

Altogether, the presented approach supports a high-resolution cortical mapping of electrophysiology and simultaneous optical observation of neuronal ensembles.

3.6. Thesis statement related to this chapter

A transparent microECoG device with Parylene HT as a biocompatible polymer substrate and encapsulation material with indium-tin-oxide (ITO) as a conductive layer was pre-

DOI:10.15774/PPKE.ITK.2023.003

sented. I investigated the optical properties and photoelectric artefacts with concurrent two-photon microscope imaging.

T2.1. I measured the optical distortion of the device that appeared on the microscope images. The measured fluorescent microbeads with a 6 µm nominal size were not distorted in the presence of the device (control: 6.11 µm (SD=0.18 µm), covered: 6.06 µm (SD=0.16 µm), p>0.05, n=10). The quality of two-photon imaging of Ca^{2+} signals in hippocampal slices was performed. Cells in the CA1 subregion were clearly visible together with fine dendritic structures in the stratum radiatum when slices were covered with the ECoG array. The mean size of the neurites under the array was 2.17 µm (SD=0.89 µm) (n=26), while without the array, the mean size of the neurites was 1.73 µm (SD=0.61 µm) (n=29).

T2.2. I investigated the sensitivity of the proposed recording sites to two-photon illumination. In resonant mode, the used laser power was between 7.7 mW and 132.4 mW, and Z-level was between 0 µm and -30 µm. Based on my analyses on the photoartefact from the different laser power, power values below 12 mW in resonant mode at the device plane (Z = 0) can be safely used without substantial photoelectric artefacts. Laser exposure 10 µm below the device plane does not induce apparent noise in the signal, while low power exposure close to the device plane contributes to parasite peaks in the power density spectra, where the fundamental frequency is corresponding to the frame rate of image acquisition. Focusing the laser beam at Z = -5 µm in resonant and Z = -10 µm in galvanic scanning mode under the ITO recording site apparently suppressed the power density of noise using 33 mW and 13 mW laser power in resonant and galvanic scanning mode, respectively.

3.7. Publications related to the thesis points

J2. Zátonyi, A.*, Madarász, M.*, **Szabó, Á.***, Lőrincz, T., Hodován, R., Rózsa, B., & Fekete, Z., "Transparent, low-autofluorescence microECoG device for simultaneous Ca^{2+} imaging and cortical electrophysiology in vivo," *Journal of Neural Engineering, 17(1), 016062*, 2020. Available: `https://doi.org/10.1088/1741-2552/ab603f`. Impact factor: 5.379.

*These authors contributed equally.

DOI:10.15774/PPKE.ITK.2023.003

3.8. References

[1] E. M. C. Hillman, "Optical brain imaging in vivo: techniques and applications from animal to man," *Journal of biomedical optics*, vol. 12, p. 051402, 9 2007.

[2] N. A. Steinmetz, C. Koch, K. D. Harris, and M. Carandini, "Challenges and opportunities for large-scale electrophysiology with neuropixels probes," *Current Opinion in Neurobiology*, vol. 50, pp. 92–100, 6 2018.

[3] C. Im and J. M. Seo, "A review of electrodes for the electrical brain signal recording," *Biomedical Engineering Letters 2016 6:3*, vol. 6, pp. 104–112, 9 2017.

[4] B. A. Wilt, L. D. Burns, E. T. Ho, K. K. Ghosh, E. A. Mukamel, and M. J. Schnitzer, "Advances in light microscopy for neuroscience," *Annual review of neuroscience*, vol. 32, p. 435, 6 2009.

[5] F. Helmchen and W. Denk, "Deep tissue two-photon microscopy," *Nature Methods 2005 2:12*, vol. 2, pp. 932–940, 11 2005.

[6] W. Yang, Y. Gong, C. Y. Yao, M. Shrestha, Y. Jia, Z. Qiu, Q. H. Fan, A. Weber, and W. Li, "A fully transparent, flexible pedot:pss–ito–ag–ito based microelectrode array for ecog recording," *Lab on a Chip*, vol. 21, pp. 1096–1108, 3 2021.

[7] J. P. Neto, A. Costa, J. V. Pinto, A. Marques-Smith, J. C. Costa, R. Martins, E. Fortunato, A. R. Kampff, and P. Barquinha, "Transparent and flexible electrocorticography electrode arrays based on silver nanowire networks for neural recordings," *ACS Applied Nano Materials*, vol. 4, pp. 5737–5747, 6 2021.

[8] S. N. Obaid, R. T. Yin, J. Tian, Z. Chen, S. W. Chen, K. B. Lee, N. Boyajian, A. N. Miniovich, I. R. Efimov, L. Lu, S. N. Obaid, R. T. Yin, J. Tian, Z. Chen, S. W. Chen, K. B. Lee, N. Boyajian, A. N. Miniovich, I. R. Efimov, and L. Lu, "Multifunctional flexible biointerfaces for simultaneous colocalized optophysiology and electrophysiology," *Advanced Functional Materials*, vol. 30, p. 1910027, 6 2020.

[9] B. Rubehn and T. Stieglitz, "In vitro evaluation of the long-term stability of polyimide as a material for neural implants," *Biomaterials*, vol. 31, pp. 3449–3458, 5 2010.

DOI:10.15774/PPKE.ITK.2023.003

[10] A. Zátonyi, Z. Borhegyi, M. Srivastava, D. Cserpán, Z. Somogyvári, Z. Kisvárday, and Z. Fekete, "Functional brain mapping using optical imaging of intrinsic signals and simultaneous high-resolution cortical electrophysiology with a flexible, transparent microelectrode array," *Sensors and Actuators B: Chemical*, vol. 273, pp. 519–526, 11 2018.

[11] A. F. Renz, J. Lee, K. Tybrandt, M. Brzezinski, D. A. Lorenzo, C. Cheraka, J. Lee, F. Helmchen, J. Vörös, C. M. Lewis, A. F. Renz, J. Lee, K. Tybrandt, M. Brzezinski, M. C. Cheraka, J. Vörös, D. A. Lorenzo, F. Helmchen, and C. M. Lewis, "Opto-edura: A soft, stretchable ecog array for multimodal, multiscale neuroscience," *Advanced Healthcare Materials*, vol. 9, p. 2000814, 9 2020.

[12] J. Tian, Z. Lin, Z. Chen, S. N. Obaid, I. R. Efimov, and L. Lu, "Stretchable and transparent metal nanowire microelectrodes for simultaneous electrophysiology and optogenetics applications," *Photonics 2021, Vol. 8, Page 220*, vol. 8, p. 220, 6 2021.

[13] Z. Chen, N. Boyajian, Z. Lin, R. T. Yin, S. N. Obaid, J. Tian, J. A. Brennan, S. W. Chen, A. N. Miniovich, L. Lin, Y. Qi, X. Liu, I. R. Efimov, L. Lu, Z. Chen, N. Boyajian, Z. Lin, R. T. Yin, S. N. Obaid, J. Tian, J. A. Brennan, S. W. Chen, A. N. Miniovich, L. Lin, I. R. Efimov, L. Lu, Y. Qi, and X. Liu, "Flexible and transparent metal nanowire microelectrode arrays and interconnects for electrophysiology, optogenetics, and optical mapping," *Advanced Materials Technologies*, vol. 6, p. 2100225, 7 2021.

[14] L. D. Vos, B. V. de Voorde, L. V. Daele, P. Dubruel, and S. V. Vlierberghe, "Poly(alkylene terephthalate)s: From current developments in synthetic strategies towards applications," *European Polymer Journal*, vol. 161, p. 110840, 12 2021.

[15] Y. Lu, X. Liu, R. Hattori, C. Ren, X. Zhang, T. Komiyama, D. Kuzum, Y. Lu, X. Liu, D. Kuzum, R. Hattori, C. Ren, T. Komiyama, and X. Zhang, "Ultralow impedance graphene microelectrodes with high optical transparency for simultaneous deep two-photon imaging in transgenic mice," *Advanced Functional Materials*, vol. 28, p. 1800002, 8 2018.

DOI:10.15774/PPKE.ITK.2023.003

[16] M. Thunemann, Y. Lu, X. Liu, K. Kılıç, M. Desjardins, M. Vandenberghe, S. Sadegh, P. A. Saisan, Q. Cheng, K. L. Weldy, H. Lyu, S. Djurovic, O. A. Andreassen, A. M. Dale, A. Devor, and D. Kuzum, "Deep 2-photon imaging and artifact-free optogenetics through transparent graphene microelectrode arrays," *Nature Communications 2018 9:1*, vol. 9, pp. 1–12, 5 2018.

[17] K. Y. Kwon, B. Sirowatka, A. Weber, and W. Li, "Opto-µ ecog array: A hybrid neural interface with transparent µ ecog electrode array and integrated leds for optogenetics," *IEEE Transactions on Biomedical Circuits and Systems*, vol. 7, pp. 593–600, 2013.

[18] Q. Huang and Y. Zhu, "Printing conductive nanomaterials for flexible and stretchable electronics: A review of materials, processes, and applications," *Advanced Materials Technologies*, vol. 4, p. 1800546, 5 2019.

[19] Y. Qiang, K. J. Seo, X. Zhao, P. Artoni, N. H. Golshan, S. Culaclii, P.-M. Wang, W. Liu, K. S. Ziemer, M. Fagiolini, H. Fang, Y. Qiang, K. J. Seo, X. Zhao, H. Fang, P. Artoni, M. Fagiolini, N. H. Golshan, K. S. Ziemer, S. Culaclii, P. m Wang, and W. Liu, "Bilayer nanomesh structures for transparent recording and stimulating microelectrodes," *Advanced Functional Materials*, vol. 27, p. 1704117, 12 2017.

[20] K. J. Seo, Y. Qiang, I. Bilgin, S. Kar, C. Vinegoni, R. Weissleder, and H. Fang, "Transparent electrophysiology microelectrodes and interconnects from metal nanomesh," *ACS Nano*, vol. 11, pp. 4365–4372, 4 2017.

[21] J. Zhang, X. Liu, W. Xu, W. Luo, M. Li, F. Chu, L. Xu, A. Cao, J. Guan, S. Tang, and X. Duan, "Stretchable transparent electrode arrays for simultaneous electrical and optical interrogation of neural circuits in vivo," *Nano Letters*, vol. 18, pp. 2903–2911, 5 2018.

[22] D. Kuzum, H. Takano, E. Shim, J. C. Reed, H. Juul, A. G. Richardson, J. D. Vries, H. Bink, M. A. Dichter, T. H. Lucas, D. A. Coulter, E. Cubukcu, and B. Litt, "Transparent and flexible low noise graphene electrodes for simultaneous electrophysiology and neuroimaging," *Nature Communications 2014 5:1*, vol. 5, pp. 1–10, 10 2014.

[23] L. V. Kayser and D. J. Lipomi, "Stretchable conductive polymers and composites based on pedot and pedot:pss," *Advanced Materials*, vol. 31, p. 1806133, 3 2019.

DOI:10.15774/PPKE.ITK.2023.003

[24] Y. U. Cho, J. Y. Lee, U. J. Jeong, S. H. Park, S. L. Lim, K. Y. Kim, J. W. Jang, J. H. Park, H. W. Kim, H. Shin, H. Jeon, Y. M. Jung, I. J. Cho, and K. J. Yu, "Ultra-low cost, facile fabrication of transparent neural electrode array for electrocorticography with photoelectric artifact-free optogenetics," *Advanced Functional Materials*, vol. 32, p. 2105568, 3 2022.

[25] M. J. Donahue, A. Kaszas, G. F. Turi, B. Rózsa, A. Slézia, I. Vanzetta, G. Katona, C. Bernard, G. G. Malliaras, and A. Williamson, "Multimodal characterization of neural networks using highly transparent electrode arrays," *eNeuro*, vol. 5, 11 2018.

[26] Y. Qiang, P. Artoni, K. J. Seo, S. Culaclii, V. Hogan, X. Zhao, Y. Zhong, X. Han, P. M. Wang, Y. K. Lo, Y. Li, H. A. Patel, Y. Huang, A. Sambangi, J. S. V. Chu, W. Liu, M. Fagiolini, and H. Fang, "Transparent arrays of bilayer-nanomesh microelectrodes for simultaneous electrophysiology and two-photon imaging in the brain," *Science Advances*, vol. 4, 2018.

[27] D. W. Hukins, A. Mahomed, and S. N. Kukureka, "Accelerated aging for testing polymeric biomaterials and medical devices," *Medical Engineering & Physics*, vol. 30, pp. 1270–1274, 12 2008.

[28] N. Kunori and I. Takashima, "A transparent epidural electrode array for use in conjunction with optical imaging," *Journal of Neuroscience Methods*, vol. 251, pp. 130–137, 8 2015.

[29] C. G. Granqvist and A. Hultåker, "Transparent and conducting ito films: new developments and applications," *Thin Solid Films*, vol. 411, pp. 1–5, 5 2002.

[30] T. D. Kozai and A. L. Vazquez, "Photoelectric artefact from optogenetics and imaging on microelectrodes and bioelectronics: new challenges and opportunities," *Journal of Materials Chemistry B*, vol. 3, pp. 4965–4978, 6 2015.

[31] B. Lu, S. Zheng, B. Q. Quach, and Y. C. Tai, "A study of the autofluorescence of parylene materials for μtas applications," *Lab on a Chip*, vol. 10, pp. 1826–1834, 6 2010.

[32] B. Chiovini, G. F. Turi, G. Katona, A. Kaszás, F. Erdélyi, G. Szabó, H. Monyer, A. Csákányi, E. S. Vizi, and B. Rózsa, "Enhanced dendritic action potential backpropagation in parvalbumin-positive basket cells during sharp wave activity," *Neurochemical Research*, vol. 35, pp. 2086–2095, 12 2010.

DOI:10.15774/PPKE.ITK.2023.003

[33] D. W. Park, A. A. Schendel, S. Mikael, S. K. Brodnick, T. J. Richner, J. P. Ness, M. R. Hayat, F. Atry, S. T. Frye, R. Pashaie, S. Thongpang, Z. Ma, and J. C. Williams, "Graphene-based carbon-layered electrode array technology for neural imaging and optogenetic applications," *Nature Communications 2014 5:1*, vol. 5, pp. 1–11, 10 2014.

[34] B. M. Blaschke, N. Tort-Colet, A. Guimerà-Brunet, J. Weinert, L. Rousseau, A. Heimann, S. Drieschner, O. Kempski, R. Villa, M. V. Sanchez-Vives, and J. A. Garrido, "Mapping brain activity with flexible graphene micro-transistors," *2D Materials*, vol. 4, p. 025040, 2 2017.

DOI:10.15774/PPKE.ITK.2023.003

Chapter 4

Potential applications and benefits

My work has improved the advancement in the technology of in vitro cell culturing microdevices. The results of my work have substantially contributed to the success of the related research project funded by the National Development and Innovation Office (NKFIH) through grant number OTKA NN 116550 (led by Dr Anita Pongrácz). The investigation on transparent microimplants paved the way for the development of new multimodal imaging approaches that recently facilitated network scale monitoring of neural activity in combination with two-photon imaging in awake animals. The results of this thesis constituted an essential part of the research project funded by NKFIH under grant number NKFIH K 120143 and 2017_1.2.1-NKP-2017-00002 (led by Dr Zoltán Fekete). Based on the above work and efforts, a long-term collaboration between Qualia Medical Inc. (Dallas, Texas, USA) has been launched, and using my established characterization tools, evaluation of shape memory polymer based microECoGs are being efficiently carried out.

DOI:10.15774/PPKE.ITK.2023.003

Chapter 5

Other publications of the author

OJ 1. Liliom, H., Lajer, P., Bérces, Z., Csernyus, B., **Szabó, Á.**, Pinke, D., Lőw, P., Fekete, Z., Pongrácz, A, & Schlett, K, "Comparing the effects of uncoated nanostructured surfaces on primary neurons and astrocytes," *Journal of Biomedical Materials Research Part A, 107(10), 2350-2359*, 2019. Available: `https://doi.org/10.1002/jbm.a.36743`

OJ 2. Csernyus, B., **Szabó, Á.**, Zátonyi, A., Hodován, R., Lázár, C., Fekete, Z., Erőss. L. & Pongrácz, A, "Recent antiepileptic and neuroprotective applications of brain cooling", *Seizure, 82, 80-90*, 2020. Available: `https://doi.org/10.1016/j.seizure.2020.09.018`

OJ 3. Csernyus, B., **Szabó, Á.**, Fiáth, R., Zátonyi, A., Lázár, C., Pongrácz, A., & Fekete, Z, "A multimodal, implantable sensor array and measurement system to investigate the suppression of focal epileptic seizure using hypothermia", *Journal of Neural Engineering, 18(4), 0460c3*, 2021. Available: `https://doi.org/10.1088/1741-2552/ac15e6`

OJ 4. Fedor, F. Z., Madarász, M., Zátonyi, A., **Szabó, Á.**, Lőrincz, T., Danda, V., Spurgin, L., Manz, C., Rózsa, B., & Fekete, Z, "Soft, Thiol-ene/Acrylate-Based Electrode Array for Long-Term Recording of Intracranial EEG Signals with Improved Biocompatibility in Mice", *Advanced Materials Technologies, 7, 2100942*, 2021. Available: `https://doi.org/10.1002/admt.202100942`

OJ 5. **Szabó, Á.**, Madarász, M., Lantos, Zs., Zátonyi, A., Danda, V., Spurgin, L., Manz, C., Rózsa, B., & Fekete, Z, "Transparent thiol-ene/acrylate based microECoG devices used for concurrent recording of fluorescent Calcium signals and electrophysiology in awake animals", *Advanced Materials Interfaces* in press, 2022.

DOI:10.15774/PPKE.ITK.2023.003

Acknowledgment

Working in a supportive and inspiring environment is a great privilege. I am grateful for creating such a workplace to my supervisor *Dr. Zoltán Fekete* and motivating me with his enthusiasm. During my work in the neuromems team, he not only helped me finding new solutions and publish them, but gave me great advices how to navigate my career. I would like to thank to *Dr. Anita Pongrácz*, my previous supervisor, to welcoming me to this wonderful team. I am also thankful to my team members, *Dr. Anita Zátonyi, Bence Csernyus, Dr. Ágoston Horváth, Zsófia Lantos, Ebrahim Ismaiel* for the friendly atmosphere and joint research work.

I find the work with collaborators a great advantage. I would like to thank all the help and work for *Dr. Hanna Liliom, Dr. Katalin Schlett* during the investigation of the interaction between astrocytes and micropatterned surfaces. Thanks to *Miklós Madarász* and *Tibor Lőrincz* for the in vitro, in vivo and two-photon experiments. Thanks for the supportive work of the cleanroom staff at the Microsystems Lab in the Centre for Energy Research.

I am thankful to the Doctoral School, especially to *Prof. Gábor Szederkényi*, *Prof. Péter Szolgay* and *Prof. Pongor Sándor* for the opportunity to participate in the doctoral program. I am specially thankful to *Dr. Tivadarné Vida* for her kind help during my doctoral studies.

I would like to thank to my family and friends for their limitless support. Special thanks to *János Szőts* for the help in editing my manuscript and all his patience, support and time during these four years.

Finally, I like to thank for the following grants to support my work. The European Union through the grant EFOP-3.6.3-VEKOP-16-2017-00002 co-financed by the European Social Fund is also acknowledged; the KAP19-32003-3.3-ITK grants; the National Brain Research Program (grant: 2017_1.2.1-NKP-2017-00002) and the National Research, Development and Innovation Office (grants: NKFIH K 120143). Also, for the New National Excellence Program of the Ministry for Innovation and Technology (grants: ÚNKP-20-3, ÚNKP-21-3)